MEASUREMENT OF THE CHIRALITY PARAMETER IN THE CHARGED-CURRENT COUPLING OF THE TAU LEPTON

by

Ronald Scott Moore

A dissertation submitted in partial fulfillment
of the requirements for the degree of
Doctor of Philosophy
(Physics)
in The University of Michigan
1998

Doctoral Committee:

Associate Professor J. Keith Riles, Chair
Associate Professor Mary L. Brake
Professor Gordon L. Kane
Associate Professor Bradford G. Orr
Professor Byron P. Roe

I deny nothing, but doubt every thing.

Lord Byron, 1788-1824

Be very, very careful what you put into that head, because you will never, ever get it out.

Cardinal Wolsey, 1475?-1530

For Patty and Freddie

ABSTRACT

MEASUREMENT OF THE CHIRALITY PARAMETER IN THE CHARGED-CURRENT COUPLING OF THE TAU LEPTON

by

Ronald Scott Moore

Chair: J. Keith Riles

According to the Standard Model of electroweak interactions, the weak charged-current has a universal $V-A$ Lorentz structure. In order to test the charged-current coupling of the τ lepton, the chirality parameter ξ_h was measured in the decays $\tau^- \to \pi^-\nu_\tau$ and $\tau^- \to \rho^-\nu_\tau$.

This measurement is based on an integrated luminosity of 148 pb^{-1} for $\mathrm{e}^+\mathrm{e}^-$ interactions at center-of-mass energies near the Z boson mass. These interactions were recorded with the L3 detector at the LEP $\mathrm{e}^+\mathrm{e}^-$ collider located at CERN. The data sample consists of 41608 selected $\mathrm{Z} \to \tau^+\tau^-$ events in which at least one of the τ decays is identified as $\tau \to \pi\nu$ or $\tau \to \rho\nu$. The chirality parameter and the average τ polarization in $\mathrm{Z} \to \tau^+\tau^-$ are measured simultaneously by using the decay spectra of individual τ decays and by exploiting the correlations between the τ^+ and τ^- in an event.

Assuming universality in τ decays, the results are:

$$\xi_h = -1.031 \pm 0.031 \pm 0.014$$

$$\mathcal{P}_\tau = -0.149 \pm 0.011 \pm 0.015\,,$$

where the first error is statistical and the second error is systematic. This value of ξ_h agrees with the Standard Model construction of a pure $V-A$ weak charged-current, and this value of $\mathcal{P}_\tau$ agrees with determinations from other experiments.

ACKNOWLEDGEMENTS

I would like to begin by acknowledging my advisor, Prof. Keith Riles, for his support, guidance and friendship during the past five years. I appreciated your insightful advice and genuine words of encouragement during times of frustration and uncertainty. I hope I can practice what I have learned about being a good scientist and a good mentor.

I would also like to thank the other UM physicists in our group: Prof. Larry Jones, Prof. Byron Roe, Dr. Tofigh Azemoon, Dr. Bob Ball and Dr. Dick Gustafson. You all helped create a stimulating and fun environment for physics research. Thanks, Tofigh, for helping Patty and me settle into life at CERN. Bob, thanks for keeping the computers running happily.

Of course, without the hard work of hundreds of physicists, engineers, technicians and support personnel, the construction and operation of the L3 experiment and the LEP machine would have been impossible. Thanks, too, to all the government agencies which help fund high-energy physics projects, as well as other basic research endeavors.

I would like to acknowledge the past and present members of the L3 τ analysis group for their collaborative efforts in making τ physics successful in L3. I especially appreciated helpful conversations with Dr. Andrei Kounine, Dr. Wolfgang Lohmann, Prof. Peter Fisher, Dr. Tom Paul, Dr. Pavel Kapinos, Dr. James Gerald, Dr. Pablo Garcia-Abiá, and Dr. Reinhold Völkert.

Thank you, Mom and Dad, for encouraging my interests in science as I was growing

up. Your constant love and support helped me become the person I am today. Marla, thanks for being a great little sister. Help all your students become interested in science.

Thanks to my friends on both sides of the Atlantic Ocean for all the laughter and good times. Getting a Ph.D. is not easy, but your friendship eased the stress.

Finally, the greatest thank you goes out to my wife, Patty. Thanks for your love, thanks for your support, thanks for your patience, and thanks for all the sacrifices you have made for me during graduate school. I know it has been very difficult at times, but we struggled together. We also had lots of wonderful times together, too, especially in Europe. Wherever we go and whatever we do in the future, I look forward to being together with you. Je t'aime.

TABLE OF CONTENTS

DEDICATION ii

ACKNOWLEDGEMENTS iii

LIST OF FIGURES vii

LIST OF TABLES ix

LIST OF APPENDICES x

CHAPTER

1. INTRODUCTION 1

2. THE STANDARD MODEL 3

2.1 Dirac Spin Notation 3
2.2 The Standard Model 6
2.2.1 The Neutral Current 11
2.2.2 The Charged Current 13
2.2.3 Masses in the Standard Model 14
2.2.4 Parameters of the Standard Model 16

3. PRODUCTION AND DECAY OF THE τ LEPTON 17

3.1 Overview of the τ and ν_τ 17
3.2 τ Production via $e^+e^- \to \tau^+\tau^-$ 17
3.3 Decays of the τ Lepton 23
3.3.1 Lorentz Structure of $\tau^- \to h^-\nu_\tau$ 25
3.3.2 $\tau^- \to \pi^-\nu_\tau$ Decays 27
3.3.3 $\tau^- \to \rho^-\nu_\tau$ Decays 28
3.4 $\tau^+\tau^-$ Correlation Distributions 33

4. EXPERIMENTAL METHOD OF THE MEASUREMENT 39

5. THE LEP COLLIDER 46

6. THE L3 DETECTOR 51

6.1 Magnet 51
6.2 Support Tube 54
6.3 Muon Spectrometer 54
6.4 Hadron Calorimeter 59
6.5 Scintillation Counters 62
6.6 Electromagnetic Calorimeter 63
6.7 Central Tracking Chambers 67
6.7.1 Time Expansion Chamber 68
6.7.2 Z-chambers 69
6.8 Silicon Microstrip Detector 69
6.9 Luminosity Monitor 71
6.10 Data Acquisition and Trigger 71
6.10.1 Level-1 Trigger 72
6.10.2 Level-2 Trigger 74
6.10.3 Level-3 Trigger 75
6.11 Detector Simulation 75

7. EVENT SELECTION 77

7.1 Data Sample 77
7.2 Event Selection 77
7.2.1 Event Preselection 78
7.2.2 Particle Identification 83
7.2.3 Event Classification and Non-τ Background Rejection 91
7.3 Estimation of Selection Efficiencies and Backgrounds 95

8. MEASUREMENT 99

8.1 Fit Results 99
8.2 Systematic Uncertainties 100

9. CONCLUSION 107

9.1 Results 107
9.2 Recent and Future Measurements 108

APPENDICES 109

BIBLIOGRAPHY 113

LIST OF FIGURES

Figure		
2.1	Fundamental vertices describing fermion interactions via: a) the weak charged current, b) the weak neutral current, and c) the electromagnetic current.	9
3.1	Feynman diagrams illustrating the Born-level processes contributing to $e^+e^- \to \tau^+\tau^-$.	18
3.2	The Born-level cross section of $e^+e^- \to \tau^+\tau^-$ as a function of the center-of-mass energy.	19
3.3	The τ polarization as a function of $\cos\theta$ in $e^+e^- \to Z \to \tau^+\tau^-$ events.	21
3.4	Initial (left) and final (right) state radiation processes contributing to QED corrections of $e^+e^- \to \tau^+\tau^-$.	23
3.5	Higher order electroweak contributions to $e^+e^- \to \tau^+\tau^-$.	24
3.6	The SM Born-level process for τ^- decay.	25
3.7	Spin configuration for right-handed τ^- in $V-A$ $\tau^- \to \pi^- \nu_\tau$.	28
3.8	The f and g kinematic functions for $\tau^- \to \pi^-\nu_\tau$ decays.	29
3.9	The x_π spectra from left-handed and right-handed $\tau^- \to \pi^-\nu_\tau$ assuming $V-A$ charged-current coupling.	30
3.10	The favored spin configurations in $\tau^- \to \rho^-\nu_\tau$.	31
3.11	The $\cos\theta^*$ distributions for left-handed and right-handed $\tau^- \to \rho^-\nu_\tau$.	31
3.12	The $\cos\psi^*$ distributions for left-handed and right-handed $\tau^- \to \rho^-\nu_\tau$.	32
3.13	The ω spectra from left-handed and right-handed $\tau^- \to \rho^-\nu_\tau$ assuming $V-A$ charged-current coupling.	33
3.14	The f and g kinematic functions for $\tau^- \to \rho^-\nu_\tau$ decays.	34
3.15	The $\rho\pi$ correlated decay distribution assuming $\mathcal{P}_\tau = -0.134$ and $\xi = -1$.	36
3.16	Projection bands of the $\rho\pi$ correlated decay distribution assuming $\mathcal{P}_\tau = -0.134$ and $\xi = -1$.	37
3.17	Projection bands of the $\rho\pi$ correlated decay distribution assuming $\mathcal{P}_\tau = -0.134$ and $\xi = -0.5$.	38
4.1	The f and g kinematic functions for $\tau^- \to \pi^-\nu_\tau$ decays.	42
4.2	The x_π distributions for left-handed and right-handed τ in $\tau^- \to \pi^-\nu_\tau$.	42
4.3	The ω distributions for left-handed and right-handed τ in $\tau^- \to \rho^-\nu_\tau$.	43
4.4	The f and g kinematic functions for $\tau^- \to \rho^-\nu_\tau$ decays.	43
5.1	Location of the LEP e^+e^- collider at CERN.	47
5.2	Accelerators in the LEP injector system.	49
5.3	Integrated luminosity recorded by L3 versus time during LEP 1.	50
6.1	Perspective view of the L3 detector.	52
6.2	View of the inner L3 subdetectors in the upper $r-z$ plane.	52
6.3	Perspective view of the L3 barrel muon chamber system.	55

6.4	Schematic of barrel muon spectrometer octant in the $x-y$ plane.	56
6.5	Measurement of track curvature in the barrel muon spectrometer.	57
6.6	Wire plane geometry in a P chamber drift cell.	58
6.7	Wire chamber layers in a long HCAL barrel module.	61
6.8	Scintillator time-of-flight difference resolution.	64
6.9	Side view of the BGO calorimeter.	65
6.10	Schematics of a BGO crystal.	66
6.11	A partial schematic of the central tracking system in the $r-\varphi$ plane.	67
6.12	Perspective drawing of the SMD.	70
7.1	A view of a $Z\rightarrow \tau^+\tau^-$ event in the $r-\varphi$ plane.	79
7.2	A view of a $Z\rightarrow \tau^+\tau^-$ event in the $r-z$ plane.	80
7.3	A view of a typical $Z\rightarrow q\bar{q}$ decay in the $r-z$ plane as reconstructed with the L3 detector.	82
7.4	The opening angle distribution between the π^- and the nearest photon in $\tau^-\rightarrow\rho^-\nu_\tau$ decays from a $e^+e^-\rightarrow Z\rightarrow\tau^+\tau^-$ Monte-Carlo sample.	84
7.5	Illustration of the algorithm used to reconstruct neutral clusters overlapping a charged hadron shower in the BGO.	86
7.6	The reconstructed mass of the π^o candidates in the hemispheres identified as $\tau^-\rightarrow\rho^-\nu_\tau$.	87
7.7	The average π^- energy resolutions versus π^- energy for momentum measurement alone, calorimetric energy measurement alone, and the combined measurement.	88
7.8	The π^- energy-momentum compatibility distribution for hemispheres identified as $\tau^-\rightarrow\pi^-\nu_\tau$ without applying the cut on the compatibility.	90
7.9	The $\pi^-\pi^o$ invariant mass distribution for hemispheres with an identified $\tau^-\rightarrow\rho^-\nu_\tau$.	91
7.10	Quantities used to reject non-τ background in the selected ρX sample.	93
7.11	Quantities used to reject non-τ background in the selected πX sample.	94
7.12	Definition of the acollinearity between two tracks.	95
7.13	Definition of track DCA.	96
7.14	The average $\tau^-\rightarrow\rho^-\nu_\tau$ selection efficiency within the fiducial volume $\lvert\cos\theta\rvert<0.7$ as a function of generated ω.	98
7.15	The average $\tau^-\rightarrow\pi^-\nu_\tau$ selection efficiency within the fiducial volume $\lvert\cos\theta\rvert<0.7$ as a function of generated x_π.	98
8.1	The observed and best-fit ω spectra for ρX events.	100
8.2	The observed and best-fit x_π spectra for πX events.	101
8.3	Projection slices of the observed and best-fit $(\omega_{min},\omega_{max})$ correlated decay distributions for $\rho\rho$ events.	102
8.4	Projection slices of the observed and best-fit $(x_\pi^{min},x_\pi^{max})$ correlated decay distributions for $\pi\pi$ events.	103
8.5	Projection slices of the observed and best-fit (x_π,ω) correlated decay distributions for $\rho\pi$ events.	104

LIST OF TABLES

Table		
2.1	Family structure of the quarks and leptons.	7
2.2	Fundamental fermion masses.	7
2.3	Masses of the SM gauge bosons.	8
2.4	Measured values of three parameters describing the electroweak interaction.	16
3.1	Measured branching fractions of major τ^- lepton decay modes.	18
6.1	Main parameters of the L3 solenoid.	53
6.2	Physical properties of BGO.	64
7.1	The numbers of selected events in each class by year.	97
7.2	The average selection efficiencies (over 4π solid angle) and background fractions from misidentified τ decays and non-τ backgrounds for the five event classes.	97
8.1	The individual and combined systematic errors for the chirality parameters and $\mathcal{P}_\tau$.	105
9.1	Other recent measurements of the chirality parameter.	108

LIST OF APPENDICES

Appendix		
A.	The ω Variable in $\tau^- \to \rho^- \nu_\tau$	110
B.	Glossary of Acronyms	111

CHAPTER 1

INTRODUCTION

In the Standard Model of electroweak interactions [1–3], the parity-violating $V-A$ Lorentz structure of the weak charged-current was selected on the basis of experimental observations. The weak charged-current mediates such processes as nuclear β-decay and decays of the muon (μ) and τ lepton. The presumed universality of the charged weak interaction can be tested by measuring the μ and τ charged-current couplings via μ and τ decays. The Lorentz structure of muon decay has been determined to be $V-A$ within experimental errors, and upper limits have been set on the presence of all other interaction types [4].

A complete understanding of the τ lepton's charged-current interactions is lacking. Semileptonic τ decays can be used to measure the chirality parameter ξ_h, equivalent to the average ν_τ helicity, which specifies the $V-A$ and $V+A$ content in the charged-current coupling of the τ. Chirality parameter measurements differing from the Standard Model prediction $\xi_h = -1$ would imply the presence of a $V+A$ current and the existence of a right-handed ν_τ.

This dissertation describes a measurement of the chirality parameter ξ_h in $\tau^- \to \pi^-\nu_\tau$ and $\tau^- \to \rho^-\nu_\tau$ decays. A collection of $Z \to \tau^+\tau^-$ events, in which at least one of the τ decays has been identified as $\tau^- \to \pi^-\nu_\tau$ or $\tau^- \to \rho^-\nu_\tau$, was selected from a sample of e^+e^- interactions recorded during 1991-1995 by the L3 detector at the e^+e^- collider LEP. The e^+e^- interactions occurred at center-of-mass energies around the Z boson mass ($M_Z \approx 92$ GeV). The chirality parameter and the average τ polarization in $Z \to \tau^+\tau^-$ were measured simultaneously by using the decay spectra of individual τ decays, and by exploiting the correlations between the τ^+ and τ^- when both τ's were identified as $\tau^- \to \pi^-\nu_\tau$ or $\tau^- \to \rho^-\nu_\tau$.

This dissertation contains nine chapters which include this introduction as Chapter 1. Chapter 2 gives an overview of the Standard Model, and Chapter 3 describes the production of $\tau^+\tau^-$ pairs via e^+e^- annihilations and the formalism of τ lepton decays. Chapter 4 outlines the method of the measurement. The LEP collider and the L3 detector are described in Chapters 5 and 6 respectively. Chapter 7 details the event selection procedure. The measurement and the systematic error study are presented in Chapter 8, and Chapter 9 contains the conclusions.

Throughout this dissertation, quantities are expressed in terms of "natural units" conventionally used in the elementary particle physics community to simplify formulæ. In these units, the speed of light c and the reduced Planck constant $\hbar$ are defined to be 1. As a result, mass, momentum and energy are equivalent and are typically expressed in MeV or GeV units. Also, when referring to exclusive τ lepton decays, usually only the τ^- decay is written. However, the charge-conjugate τ^+ decay is also implied, unless noted otherwise.

My personal contributions to the L3 experiment included both analysis and hardware activities. For this measurement, I modified the event selection and identification criteria developed by other members of the L3 τ analysis group for similar analyses of τ polarization which assume a pure $V-A$ structure of the τ charged-current coupling. I then performed the measurement and study of systematic uncertainties described in this dissertation. I also contributed to the 1994 hadron calorimeter calibration and the 1995 study of alignment between the electromagnetic calorimeter and tracking chambers. My hardware responsibilities included construction, installation, and maintenance of timing calibration electronics for the endcap muon drift chamber system, as well as monitoring shifts in the L3 control room.

CHAPTER 2

THE STANDARD MODEL

The Standard Model (SM) is a relativistic, gauge invariant, quantum field theory which describes the interactions of the known fundamental fermions via the exchange of spin-1 bosons. The theory incorporates three of the four known forces of nature: the familiar electromagnetism; the weak force, responsible for radioactive β-decay processes; and the strong force, which binds protons and neutrons in nuclei. Electromagnetism and the weak force have been unified into a single "electroweak" interaction. While the SM has been impressively consistent with experimental observations, it is incomplete. A fully relativistic quantum field theory for gravity has not yet been developed, and the SM does not address many basic questions, such as "Why do particles have the masses they do?" and "Why are there three generations of fermions?" Theorists hope to unify Quantum Chromodynamics (the quantum theory for the strong force) and even gravity with the electroweak force to have a complete theoretical description of particle interactions.

This chapter will describe features of the SM relevant to this analysis. In particular, the structure of the weak neutral and charged currents will be presented. The notation and logic follows that in References [5] and [6].

2.1 Dirac Spin Notation

Fermions and the concept of spin play central roles in the physical world and the SM. To accommodate spin-1/2 fermions in a relativistically correct manner, the SM must incorporate solutions of the Dirac equation. In this section, the notation for describing spin-1/2 fermions will be reviewed.

In 1928, Dirac derived an equation of motion for a relativistic free electron which properly included the effects of spin [7]. Although written for an electron, the equation applies to all spin-1/2 fermions. He began with the most general, relativistically covariant, probability-conserving equation (linear in the space and time derivatives) for the wavefunction ψ:

$$i\frac{\partial\psi}{\partial t} = (-i\,\vec{\alpha}\cdot\vec{\nabla} + \beta m)\,\psi\,. \tag{2.1}$$

The four coefficients $\vec{\alpha}$ and β must satisfy conditions imposed by the energy-momentum relation $E^2 = (pc)^2 + (mc^2)^2$. Dirac realized that these conditions were anticommutation relations which could be satisfied by particular sets of 4×4 matrices. While such matrices are not unique, it is convenient to use the so-called γ-matrices defined by $\gamma^0 = \beta$ and $\gamma^i = \beta\alpha_i$:

$$\gamma^0 = \begin{pmatrix} 0 & 1 \\ 1 & 0 \end{pmatrix} \qquad \gamma^i = \begin{pmatrix} 0 & -\sigma_i \\ \sigma_i & 0 \end{pmatrix} \tag{2.2}$$

where $i = 1, 2, 3$. In this representation, each element of the γ-matrices is actually a 2×2 matrix where 1 is the unit matrix and σ_i are the Pauli matrices

$$\sigma_1 = \begin{pmatrix} 0 & 1 \\ 1 & 0 \end{pmatrix} \quad \sigma_2 = \begin{pmatrix} 0 & -i \\ i & 0 \end{pmatrix} \quad \sigma_3 = \begin{pmatrix} 1 & 0 \\ 0 & -1 \end{pmatrix}. \tag{2.3}$$

The matrix

$$\gamma^5 \equiv i\gamma^0\gamma^1\gamma^2\gamma^3 = \begin{pmatrix} 1 & 0 \\ 0 & -1 \end{pmatrix} \tag{2.4}$$

is a useful combination which will appear again shortly. The γ-matrices allow Equation 2.1 to be written in a compact four-vector notation. Assuming a plane wave solution for free particles, the Dirac equation becomes

$$(i\gamma^\mu\partial_\mu - m)\,\psi \;=\; (\gamma^\mu p_\mu - m)\,\psi = 0. \tag{2.5}$$

Solutions of the Dirac equation are four-component spinors corresponding to the spin-up and spin-down states of the electron and the positron. One representation of the solutions can be written

$$\psi = \begin{pmatrix} \varphi \\ \chi \end{pmatrix} \tag{2.6}$$

where φ and χ are two-component spinors with a special significance to be shown shortly. In this form, the Dirac equation 2.5 reduces to the two equations

$$\vec{\sigma}\cdot\hat{p}\,\chi = -\frac{E}{|\vec{p}|}\,\chi + \frac{m}{|\vec{p}|}\,\varphi \qquad \vec{\sigma}\cdot\hat{p}\,\varphi = \frac{E}{|\vec{p}|}\,\varphi - \frac{m}{|\vec{p}|}\,\chi\,, \tag{2.7}$$

where $\hat{p} \equiv \vec{p}\,/\,|\vec{p}|$ is the unit vector along the momentum direction. The *helicity operator* $\vec{\sigma}\cdot\hat{p}$ measures the spin component parallel to the momentum. A right-handed fermion has its spin axis parallel to its momentum, whereas the spin axis of a left-handed fermion is antiparallel to its momentum. In the ultrarelativistic limit $E \gg m$, the above equations separate and reveal that φ and χ are eigenspinors of the helicity operator:

$$\vec{\sigma}\cdot\hat{p}\,\chi = -\chi \qquad \text{negative helicity} \tag{2.8}$$

$$\vec{\sigma}\cdot\hat{p}\,\varphi = +\varphi \qquad \text{positive helicity .} \tag{2.9}$$

The significance of φ and χ is now apparent. Positive helicity states (φ) correspond to right-handed fermions and left-handed antifermions, while negative helicity states (χ) refer to left-handed fermions and right-handed antifermions.

The so-called *projection operators* P_L and P_R select one of the two chiral components from a Dirac spinor. In terms of the γ-matrices,

$$P_L = \frac{1}{2}(1-\gamma^5) \qquad\qquad P_R = \frac{1}{2}(1+\gamma^5)\,. \tag{2.10}$$

For example, explicitly applying the P_L operator to a Dirac spinor gives

$$P_L\,\psi = \frac{1}{2}\left[\begin{pmatrix}1&0\\0&1\end{pmatrix} - \begin{pmatrix}1&0\\0&-1\end{pmatrix}\right]\begin{pmatrix}\varphi\\ \chi\end{pmatrix} = \begin{pmatrix}0&0\\0&1\end{pmatrix}\begin{pmatrix}\varphi\\ \chi\end{pmatrix} = \begin{pmatrix}0\\ \chi\end{pmatrix}\,. \tag{2.11}$$

The notations f_L and f_R will signify the left and right-handed projections, $P_L\,f$ and $P_R\,f$ respectively, of a fermion f.

The γ-matrices are also used to describe the Lorentz transformation properties of fermion interactions. For fermion spinors u and v, possibly being the same fermion, Lorentz invariance allows the following five currents with the indicated transformation properties:

scalar	$\bar{v}u$	$=$	$\bar{v}_L u_R + \bar{v}_R u_L$	(2.12)
pseudoscalar	$\bar{v}\gamma^5 u$	$=$	$\bar{v}_L u_R - \bar{v}_R u_L$	(2.13)
vector	$\bar{v}\gamma^\mu u$	$=$	$\bar{v}_R\gamma^\mu u_R + \bar{v}_L\gamma^\mu u_L$	(2.14)
axial-vector	$\bar{v}\gamma^5\gamma^\mu u$	$=$	$\bar{v}_R\gamma^\mu u_R - \bar{v}_L\gamma^\mu u_L$	(2.15)
tensor	$\bar{v}\sigma^{\mu\nu} u$	$=$	$\bar{v}_L\sigma^{\mu\nu} u_R + \bar{v}_R\sigma^{\mu\nu} u_L$,	(2.16)

where $\sigma^{\mu\nu} = \frac{i}{2}(\gamma^\mu\gamma^\nu - \gamma^\nu\gamma^\mu)$. Note that the terms of the vector and axial-vector currents (right-hand sides of 2.14 and 2.15) contain both right-handed or both left-handed fermion

spinors, while the terms of the other interactions have one spinor of each chirality. Accordingly, only vector and axial-vector interactions preserve the chirality of the interacting fermions, *i.e.*, couple fermions of the same chirality. One should also note the properties of these currents under parity. The parity operator P inverts coordinates ($\vec{x} \rightarrow -\vec{x}$) and reverses momenta ($\vec{p} \rightarrow -\vec{p}$), but spins remain unchanged; this "mirror image" operator turns left-handed fermions into right-handed fermions and *vice versa*. Consequently, applying P to the pseudoscalar and axial-vector currents changes their signs, implying these interactions behave differently for left and right-handed fermions. The other interactions do not distinguish the interacting fermions' handedness. As will be demonstrated in the following section, vector and axial-vector interactions play central roles in the Standard Model.

2.2 The Standard Model

The fundamental spin-1/2 fermions include the quarks and the leptons, as well as their antimatter partners; the quarks feel the strong force, while the leptons do not. As indicated in Table 2.1, the quarks and leptons can be arranged into three groups, called *families* or *generations*, of doublets. This arrangement is akin to Mendeleev's periodic table of the elements. The corresponding members of the three families exhibit many identical properties, such as electric charge and electroweak isospin, except for mass. The second and third generations merely seem to be heavier replicas of the first generation. Only the first generation fermions are stable; the other fermions quickly decay into lighter fermions, which may themselves decay, until only first generation fermions remain. Table 2.2 lists the masses of the quarks and leptons. The antifermions have the same mass and spin as their matter counterparts, but all of their charges are opposite. Since the interactions of the second and third generation fermions are quite similar to the first fermion generation, only the first generation fermions will be used in equations and discussions throughout the rest of this chapter, unless noted otherwise.

The fermions possess three empirically discovered, internal symmetries. In the language of mathematical group theory, these symmetries are based on sets of transformations which form $U(1)$, $SU(2)$ and $SU(3)$ groups. It is not known why particles should possess these particular symmetries, or if they possess others. The $U(1)$ transformations are called Abelian, since applying them in any order gives the same result. Conversely, the

	Generation 1	2	3	Q
quarks	$\begin{pmatrix} u \\ d \end{pmatrix}$	$\begin{pmatrix} c \\ s \end{pmatrix}$	$\begin{pmatrix} t \\ b \end{pmatrix}$	$+2/3$ $-1/3$
leptons	$\begin{pmatrix} \nu_e \\ e \end{pmatrix}$	$\begin{pmatrix} \nu_\mu \\ \mu \end{pmatrix}$	$\begin{pmatrix} \nu_\tau \\ \tau \end{pmatrix}$	0 -1

Table 2.1: Family structure of the quarks and leptons. Q is the electric charge.

Quark	Mass (GeV)	Lepton	Mass (MeV)
u	$(2\text{-}8)\times10^{-3}$	e	0.511
d	$(5\text{-}15)\times10^{-3}$	μ	105.6
s	0.1-0.3	τ	1777
c	1.0-1.6	ν_e	$< 8(10)^{-6}$
b	4.1-4.5	ν_μ	< 0.17
t	175	ν_τ	< 18.2

Table 2.2: Fundamental fermion masses. The listed quark masses are the "current" or "free" quark masses.

Boson	Mass (GeV)
γ	0
W^+, W^-	≈ 80.2
Z	≈ 91.2
g	0

Table 2.3: Masses of the SM gauge bosons.

non-Abelian $SU(2)$ and $SU(3)$ transformations do not commute.

A free particle Lagrangian for fermions contains only kinetic energy and mass terms:

$$\mathcal{L}_{free} = \bar{f}\,(i\gamma^{\mu}\partial_{\mu} - m)\,f\,, \tag{2.17}$$

where $\bar{f} = f^{\dagger}\gamma^{0}$. Quantum mechanics asserts that the physical observables of a system depend on $|\psi|^2$, where ψ is the wavefunction describing the system. Consequently, the Lagrangian should be invariant under changes of phase convention of ψ at each space-time point. These transformations are called *local phase transformations* or *gauge transformations*, and Lagrangians that are symmetric under such transformations are said to be *gauge invariant.* However, a free particle Lagrangian cannot be gauge invariant; gauge invariance requires the existence of vector fields and associated spin-1 particles called *gauge bosons.* These fields generate interactions between fermions that are mediated by the exchange of gauge bosons. Hence, under gauge invariance, the free theory actually contains an interaction between the fermions. The Lagrangian can be written in gauge invariant form by replacing ∂_{μ} with a covariant derivative which contains the interacting field. In the SM, the photon and the weak force bosons (W^+, W^- and Z) are the gauge bosons of the combined $U(1)$ and $SU(2)$ symmetries. The $SU(3)$ gauge bosons are the eight gluons of QCD which mediate the strong interaction. As shown in Table 2.3, the photon and gluons are massless, while the $W^{\pm}$ and Z have considerable mass.

The fundamental interactions between the electroweak gauge bosons and fermions are illustrated in Figure 2.1. The coupling strengths are expressed in terms of the electron charge e and the electroweak mixing angle θ_w which will be described later.

One important feature of the SM is that left and right-handed fermions transform differently under $SU(2)$ transformations. Although the theory can accommodate this violation of parity, the SM does not explain the origin of parity violation. The left-handed

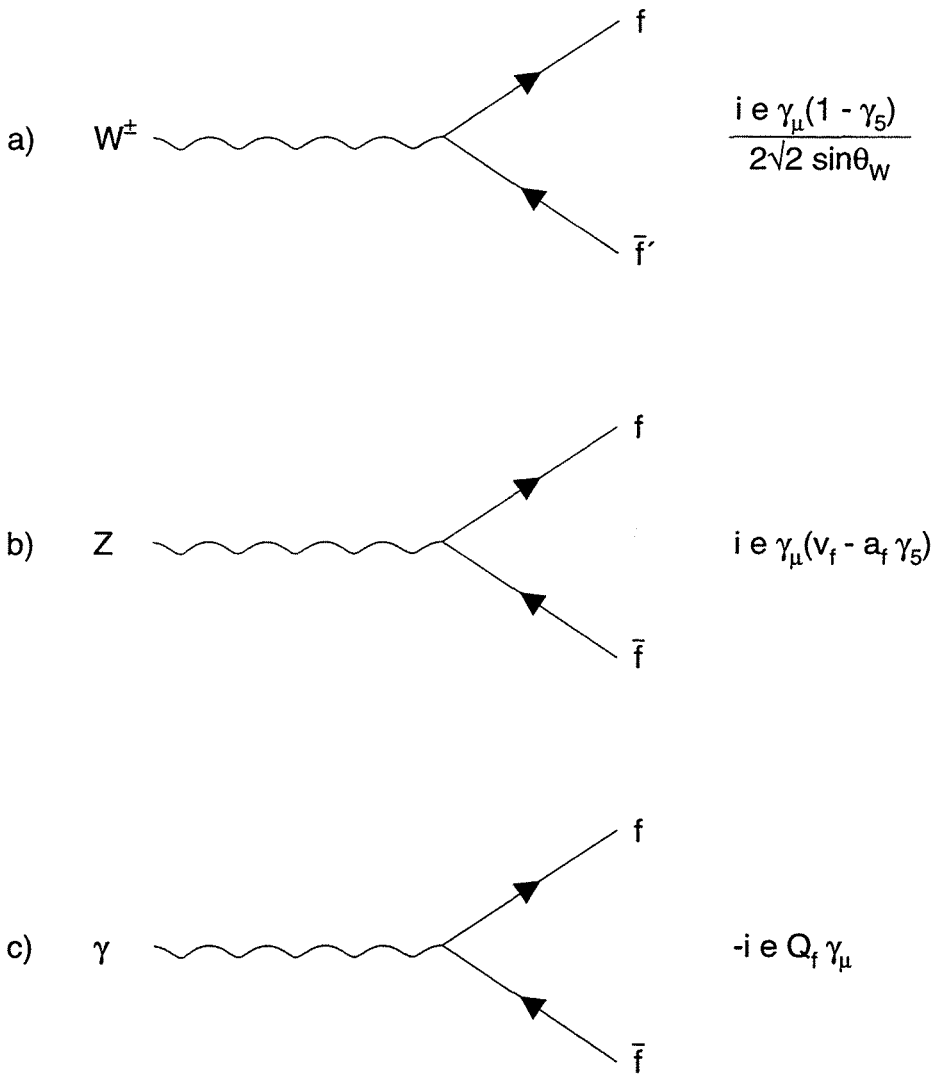

Figure 2.1: Fundamental vertices describing fermion interactions via: a) the weak charged current, b) the weak neutral current, and c) the electromagnetic current.

electron and ν_e form an $SU(2)$ doublet

$$L = \begin{pmatrix} \nu_e \\ e^- \end{pmatrix}_L \tag{2.18}$$

and the right-handed electron e_R is an $SU(2)$ singlet. The SM does not contain a right-handed neutrino, as dictated by current experimental results. The quarks behave similarly to the leptons. The right-handed u and d quark states are $SU(2)$ singlets $u_{R\alpha}$ and $d_{R\alpha}$, while the left-handed u and d quarks comprise an $SU(2)$ doublet

$$Q_{L\alpha} = \begin{pmatrix} u_\alpha \\ d_\alpha \end{pmatrix}_L . \tag{2.19}$$

Each quark needs an additional label, α, to indicate its state in the $SU(3)$ triplet space for the strong force. The leptons are $SU(3)$ singlets since they do not feel the strong force. The second and third generation fermion states have the same structure.

The interaction Lagrangian of the Standard Model (for the first generation fermions) can be written as

$$\mathcal{L}_{SM} = \sum_{\substack{f=L,e_R \\ Q_{L\alpha},u_{R\alpha},d_{R\alpha}}} \bar{f} i\gamma^\mu \mathcal{D}_\mu f$$

$$\mathcal{D}_\mu = \partial_\mu - \underbrace{ig_1\frac{Y}{2}B_\mu}_{U(1)} - \underbrace{ig_2\frac{\tau^i}{2}W^i_\mu}_{SU(2)} - \underbrace{ig_3\frac{\lambda^a}{2}G^a_\mu}_{SU(3)}$$

where the sum is over the lepton and quark left-handed doublets and right-handed singlets, and $\mathcal{D}_\mu$ is the covariant derivative necessary for gauge invariance under transformations from the labeled groups. $\mathcal{D}_\mu$ contains a term for each gauge symmetry. B_μ, W^i_μ and G^a_μ represent the interacting fields, while Y, τ^i and λ^a denote the generators of the corresponding groups. Y is just a number, called *weak hypercharge*, but it has different values for left and right-handed fermions; their values are ascertained in the next section. The τ^i are the familiar 2×2 Pauli matrices explicitly written (with the labels σ^i) in Equation 2.3. The λ^a, $a = 1..8$, are eight 3×3 matrices whose representations can be found in Appendix B.4 of Reference [5].

The factors g_1, g_2 and g_3 symbolize the interaction coupling strengths of the fields and must be measured experimentally. Writing the Lagrangian in this compact form requires the convention that $\mathcal{D}_\mu$ terms acting on fermion states of different matrix form give zero. For example, the 2×2 matrix $\tau^i W^i_\mu$ gives zero when operating on the $SU(2)$ singlet

states e_R, $u_{R\alpha}$ and $d_{R\alpha}$. Similarly, $\lambda^a G^a_\mu$, a 3×3 matrix in $SU(3)$, acting on the lepton $SU(3)$ singlets also gives a zero result. The terms for the second and third generation fermions are obtained by summing over the corresponding fermion states.

The remainder of this chapter concentrates on the $U(1)$ and $SU(2)$ terms of the SM Lagrangian, since those are the terms responsible for the physics relevant to this measurement. After defining the charge states, W^+_μ, W^-_μ and W^0_μ of the $SU(2)$ fields

$$W^\pm_\mu \equiv (-W^1_\mu \pm i\, W^2_\mu)/\sqrt{2} \qquad\qquad W^0_\mu \equiv W^3_\mu\,, \tag{2.20}$$

the $SU(2) \times U(1)$ piece of the Lagrangian for leptons can be expressed

$$\begin{aligned}\mathcal{L}^{\text{leptons}}_{SU(2)\times U(1)} &= \frac{g_1}{2}\left[\, Y_L\, (\bar{\nu}_L \gamma^\mu \nu_L + \bar{e}_L \gamma^\mu e_L) + Y_R\, \bar{e}_R \gamma^\mu e_R\right] B_\mu \\ &+\frac{g_2}{2}\left[\bar{\nu}_L \gamma^\mu \nu_L W^0_\mu - \bar{e}_L \gamma^\mu e_L W^0_\mu - \sqrt{2}\, \bar{\nu}_L \gamma^\mu e_L W^+_\mu - \sqrt{2}\, \bar{e}_L \gamma^\mu \nu_L W^-_\mu\right]. \end{aligned} \tag{2.21}$$

The terms containing $\bar{e}_L \gamma^\mu e_L$, $\bar{\nu}_L \gamma^\mu \nu_L$, $\bar{e}_R \gamma^\mu e_R$, are called the *neutral current* (NC), while the $\bar{e}_L \gamma^\mu \nu_L$ and $\bar{\nu}_L \gamma^\mu e_L$ terms make up the *charged current* (CC). Y_L and Y_R specify the weak hypercharge for the left and right fermion chiral states. Since the leptons do not interact with the strong force $SU(3)$ field, Equation 2.21 represents, by construction, the electromagnetic and weak interactions of the leptons. How the B_μ and W_μ fields relate to the physical fields must be determined.

The neutral and charged-current interactions of the quarks are similar to those of the leptons. However, the charged-current couplings of the left-handed quarks involve a mixing of states which will be explained later.

2.2.1 The Neutral Current

In principle, the photon should be a linear combination of the neutral fields B_μ and W^0_μ. Consider the neutral current for the neutrinos

$$(\frac{g_1}{2} Y_L B_\mu + \frac{g_2}{2} W^0_\mu)\, \bar{\nu}_L \gamma^\mu \nu_L\,. \tag{2.22}$$

Since the neutrino is electrically neutral, it has no electromagnetic interactions. Hence, the electromagnetic field must be orthogonal to the combination in Equation 2.22. The two orthogonal linear combinations of B_μ and W^0_μ

$$A_\mu \equiv \frac{g_2 B_\mu - g_1 Y_L W^0_\mu}{\sqrt{g_2^2 + g_1^2 Y_L^2}} \qquad\qquad Z_\mu \equiv \frac{g_1 Y_L W^0_\mu + g_2 B_\mu}{\sqrt{g_2^2 + g_1^2 Y_L^2}} \tag{2.23}$$

properly represent the electromagnetic field A_μ and the weak neutral current, Z_μ, mediated by the Z-boson.

Using the definitions in Equation 2.23, we can rewrite the neutral current Lagrangian terms for the electron as

$$\begin{aligned}\mathcal{L}_{NC} &= A_\mu \left\{ \left[\frac{g_1 g_2 Y_L}{\sqrt{g_2^2 + g_1^2 Y_L^2}}\right] \bar{e}_L \gamma^\mu e_L + \left[\frac{g_1 g_2 Y_R}{2\sqrt{g_2^2 + g_1^2 Y_L^2}}\right] \bar{e}_R \gamma^\mu e_R \right\} \\ &+ Z_\mu \left\{ \left[\frac{g_1^2 Y_L^2 - g_2^2}{2\sqrt{g_2^2 + g_1^2 Y_L^2}}\right] \bar{e}_L \gamma^\mu e_L + \left[\frac{g_1^2 Y_L Y_R}{2\sqrt{g_2^2 + g_1^2 Y_L^2}}\right] \bar{e}_R \gamma^\mu e_R \right\} . \qquad (2.24)\end{aligned}$$

From electromagnetism, we know that the square-bracketed coupling strengths of the A_μ terms must be the electric charge $-e$. Imposing this physical requirement gives

$$Y_R = 2Y_L \qquad e = -g_2 g_1 Y_L \Big/ \sqrt{g_2^2 + g_1^2 Y_L^2} \, . \qquad (2.25)$$

By choosing the weak hypercharge $Y_L = -1$ (changes in Y_L can be absorbed by redefining g_1), the electric charge can be expressed in terms of the coupling strengths g_1 and g_2

$$e = g_1 g_2 \Big/ \sqrt{g_1^2 + g_2^2} \, . \qquad (2.26)$$

Equations 2.23 and 2.26 suggest that the mixing of the B_μ and W_μ^0 fields can be described by a rotation angle defined by

$$\sin\theta_w = g_1 \Big/ \sqrt{g_1^2 + g_2^2} \qquad \text{or} \qquad \cos\theta_w = g_2 \Big/ \sqrt{g_1^2 + g_2^2} \, . \qquad (2.27)$$

The angle θ_w is called the *electroweak mixing angle*. By substituting the above equations into Equation 2.26, the $SU(2)$ and $U(1)$ coupling strengths can be expressed in terms of a single coupling strength, *i.e.*, the electric charge, and the electroweak mixing angle:

$$g_1 = e/\sin\theta_w \qquad g_2 = e/\cos\theta_w \, . \qquad (2.28)$$

These arguments demonstrate the unification of the electromagnetic and weak forces into a single "electroweak" interaction which is invariant under $SU(2) \times U(1)$ gauge transformations.

The previous arguments show that the physical fields Z_μ and A_μ, corresponding to the Z boson and the photon, are given by rotations of the $U(1)$ and $SU(2)$ fields B_μ and W_μ^0:

$$Z_\mu = W_\mu^0 \cos\theta_w + B_\mu \sin\theta_w \qquad A_\mu = -W_\mu^0 \sin\theta_w + B_\mu \cos\theta_w \, . \qquad (2.29)$$

In terms of vector and axial-vector interactions, the neutral current Lagrangian can be expressed

$$\mathcal{L}_{NC} \;=\; -e\,\bar{\mathrm{e}}\gamma^{\mu}\mathrm{e}\,A_{\mu} \;+\; e\,[\,\bar{\mathrm{e}}(g_v^e\gamma^{\mu} - g_a^e\gamma^{\mu}\gamma^5)\mathrm{e} \;+\; \bar{\nu}(g_v^{\nu}\gamma^{\mu} - g_a^{\nu}\gamma^{\mu}\gamma^5)\nu\,]\,Z_{\mu} \quad (2.30)$$

with

$$g_v^f \equiv \frac{T_3 - 2Q\,\sin^2\theta_w}{2\,\sin\theta_w\cos\theta_w} \qquad\qquad g_a^f \equiv \frac{T_3}{2\,\sin\theta_w\cos\theta_w}\,, \quad (2.31)$$

where g_v and g_a denote the vector and axial-vector coupling constants for the fermion f. T_3 is third component of electroweak isospin; $T_3 = \pm 1/2$ for the upper/lower members of the left-handed $SU(2)$ doublets, and $T_3 = 0$ for the right-handed $SU(2)$ singlets. The quark couplings to the neutral current are exactly like the lepton couplings.

2.2.2 The Charged Current

The charged-current terms in the SM Lagrangian represent transitions between the members of the left-handed $SU(2)$ doublet:

$$\mathcal{L}_{CC} = -\frac{g_2}{\sqrt{2}}\,[\,\bar{\nu}_L\gamma^{\mu}\mathrm{e}_L\,W_{\mu}^{+} \;+\; \bar{\mathrm{e}}_L\gamma^{\mu}\nu_L\,W_{\mu}^{-}\,]\,. \quad (2.32)$$

The $W^{\pm}$ bosons are the physical manifestations of the $W_{\mu}^{\pm}$ fields. It is essential to note that *only* the left-handed fermions have charged-current interactions. Recall that the right-handed electron e_R is an $SU(2)$ singlet and right-handed neutrinos have not been experimentally observed. This inherent parity violation can be expressed another way. Using the Dirac spinor projection operators discussed earlier, the charged-current Lagrangian looks like

$$\mathcal{L}_{CC} = -\frac{g_2}{2\sqrt{2}}\,[\,\bar{\nu}\,(\gamma^{\mu} - \gamma^{\mu}\gamma_5)\,\mathrm{e}\,W_{\mu}^{+} \;+\; \bar{\mathrm{e}}\,(\gamma^{\mu} - \gamma^{\mu}\gamma_5)\,\nu\,W_{\mu}^{-}\,]\,. \quad (2.33)$$

Like the weak neutral current, the charged-current interaction consists of vector and axial-vector currents. The Lorentz structure $(\gamma^{\mu} - \gamma^{\mu}\gamma_5)$ is called $V\!-\!A$, for "vector$-$axial vector", and is the hallmark of the SM weak charged-current. If the $SU(2)$ lepton doublet were right-handed instead of left-handed, the charged current would have a $(\gamma^{\mu} + \gamma^{\mu}\gamma_5)$ or $V\!+\!A$ structure.

As mentioned earlier in this section, the couplings of the left-handed, down-type $(Q = -1/3)$ quarks to the charged current involves a mixing of the quark states in all three generations. This mixing stems from the fact that the mass eigenstates are not the same as

the electroweak eigenstates. By convention, the mixing is formulated as a rotation of the down-type quark states. The charged current for quarks is then expressed

$$J^{\mu}_{CC} = \begin{pmatrix} \bar{u} & \bar{c} & \bar{t} \end{pmatrix} \gamma^{\mu} P_L \begin{pmatrix} d' \\ s' \\ b' \end{pmatrix} \qquad \begin{pmatrix} d' \\ s' \\ b' \end{pmatrix} = \begin{pmatrix} V_{ud} & V_{us} & V_{ub} \\ V_{cd} & V_{cs} & V_{cb} \\ V_{td} & V_{ts} & V_{tb} \end{pmatrix} \begin{pmatrix} d \\ s \\ b \end{pmatrix} , \quad (2.34)$$

where the 3×3 rotation matrix V_{ij}, called the CKM matrix, describes the down-type quark electroweak eigenstates in terms of the mass eigenstates. In 1963, Cabibbo wrote a rotation matrix for the quarks in the first two generation [8]. Kobayashi and Maskawa later generalized the rotation matrix to three generations [9]. The CKM matrix is nearly the unit matrix; its small off-diagonal elements indicate mixing. This mixing allows the s and b quarks to decay via the charged current.

2.2.3 Masses in the Standard Model

The interaction Lagrangians outlined previously neglect the question of why most particles have mass. The SM can accommodate mass through a spontaneous breaking of the $SU(2) \times U(1)$ local gauge symmetry called the Higgs mechanism. Englert and Brout [10] and Higgs [11] described spontaneous breaking of an Abelian local gauge symmetry in the early 1960's, and their work was extended to the non-Abelian SM framework by Weinberg [1], Salam [2], and Glashow [3].

According to the Higgs mechanism, a scalar field φ, called the Higgs field, permeates the universe. Interactions with the Higgs field is the source of particles' masses. The Higgs field is an $SU(2)$ doublet with non-zero $U(1)$ hypercharge, but it is an $SU(3)$ color singlet. The $SU(2)$ doublet representation of φ is $\varphi = \begin{pmatrix} \varphi^+ \\ \varphi^0 \end{pmatrix}$, where φ^+ and φ^0 represent charged and neutral components. If the vacuum (ground) state φ_0 has non-zero $SU(2)$ and $U(1)$ quantum numbers, the $SU(2) \times U(1)$ symmetry is spontaneously broken. The spontaneous symmetry-breaking also causes the vacuum state to have non-zero Higgs field potential energy (vacuum expectation value). Conservation of electric charge requires that only φ^0 can have a non-zero vacuum expectation value.

Interactions between the Higgs field and the up to now massless $SU(2)$ and $U(1)$ fields W^i_{μ} and B_{μ} are represented by the Lagrangian:

$$\varphi^{\dagger} \left(i g_1 \frac{Y}{2} B_{\mu} + i g_2 \frac{\tau^i}{2} W^i_{\mu} \right)^{\dagger} \left(i g_1 \frac{Y}{2} B_{\mu} + i g_2 \frac{\tau^i}{2} W^i_{\mu} \right) \varphi \, . \quad (2.35)$$

Writing the Higgs field as $\varphi = \frac{1}{\sqrt{2}}\begin{pmatrix} 0 \\ v + H(x) \end{pmatrix}$ and expressing W_μ^i and B_μ in terms of the physical fields $W_\mu^\pm$, Z_μ and A_μ, the above Lagrangian can be shown to contain terms representing massive vector fields:

$$\frac{1}{2}\left(\frac{1}{2}vg_2\right)^2 W_\mu^+ W^{-\mu} + \frac{1}{2}\left(\frac{1}{2}v\sqrt{g_1^2+g_2^2}\right)^2 Z_\mu Z^\mu \,. \tag{2.36}$$

(Note that the term proportional to $A_\mu A^\mu$ is absent.) From the coefficients of each term, we can identify the masses of the gauge bosons: $M_\mathrm{W} = vg_2/2$, $M_\mathrm{Z} = v\sqrt{g_1^2+g_2^2}/2$, and $M_\gamma = 0$. Using the right-hand member of Equations 2.27, we see that the W and Z boson masses are intimately related

$$M_\mathrm{W}/M_\mathrm{Z} = \cos\theta_w \,. \tag{2.37}$$

That the W and Z bosons in fact exist and have masses consistent with the independently measured value of θ_w demonstrates one of the many successful predictions of the Standard Model.

In addition to the mass terms, the interaction between the gauge bosons and the Higgs field gives rise to a new scalar boson called the Higgs boson. The Higgs boson mass is unknown because it depends on an arbitrary self-coupling parameter whose value is not predicted by the theory. The Higgs boson couples directly to the gauge bosons with a strength proportional to the gauge boson mass.

The fermions also acquire mass by interacting with the Higgs field. After writing the appropriate Lagrangian terms for these interactions, one finds that the mass of a fermion f is given by:

$$m_f = g_f\, v/\sqrt{2} \,, \tag{2.38}$$

where g_f represents an arbitrary coupling parameter. These coupling parameters differ for each fermion and are not determined from a gauge principle, unlike the g_1 and g_2 electroweak coupling strengths. In this sense, the SM does not predict the fermion masses; they must be measured experimentally. In fact, g_f represents the strength of the Higgs boson coupling to the fermion. Rearranging the above equation reveals that, like the gauge bosons, the Higgs boson couples to fermions with a strength proportional to the fermion mass.

2.2.4 Parameters of the Standard Model

Although the SM continues to survive experimental tests successfully, there are many parameters that are not predicted by the theory, and they must be measured by experiment. These unspecified parameters include the fermion masses, the charged-current mixing angles of the quarks, the Higgs boson mass, three free parameters from the electroweak sector, and two more parameters associated with $SU(3)$ color force. The fact that the SM does not specify values for these parameters is one clear indication that the SM is not complete; a complete theory would predict their values.

The three free electroweak-related parameters can be represented by several combinations of common parameters. For example, the W boson mass, the fine structure constant α, and $\sin^2\theta_w$ fully determine the electroweak couplings and gauge boson masses. The most useful set of parameters for e^+e^- annihilation at $\sqrt{s} \approx M_Z$ are α, G_F and the Z boson mass. The parameter G_F is called the Fermi constant and is defined as $G_F/\sqrt{2} = g_2^2/8M_W^2$; its value can be determined by measuring the muon lifetime. Each of these parameters has been independently well-measured. The experimental measurements of these parameters are given in Table 2.4.

Parameter	Value
α	$1/(137.0359895 \pm 0.0000061)$ [12]
G_F	$(1.16639 \pm 0.00002) \times 10^{-5}$ GeV^{-2} [12]
M_Z	91.1867 ± 0.0020 GeV [13]

Table 2.4: Measured values of three parameters describing the electroweak interaction.

CHAPTER 3

PRODUCTION AND DECAY OF THE τ LEPTON

3.1 Overview of the τ and ν_τ

The τ lepton was discovered in 1975 by M. Perl *et al.* at the e^+e^- collider SPEAR [14], and it was the first known fermion from the third generation. Due to its large mass ($m_\tau = 1777.00^{+0.30}_{-0.27}$ MeV [12]), the τ is the only lepton that has decays involving hadrons in the final state. The final state always includes a ν_τ. The τ's short lifetime, $\tau_\tau = 290.21 \pm 1.15$ fs [15], makes it difficult to observe directly, so the τ decay products are used to analyze the τ itself. Table 3.1 lists the branching fractions for the major τ decay modes.

The τ-neutrino ν_τ remains the only fermion from the three SM generations not yet observed experimentally. Its existence is inferred from the fact that the τ decays as predicted if the ν_τ existed with the expected SM properties. The best direct limit on the ν_τ mass from an accelerator-based experiment is $m_{\nu_\tau} < 18.2$ MeV [16].

3.2 τ Production via $e^+e^- \to \tau^+\tau^-$

Pairs of τ leptons can be produced in e^+e^- annihilation through a virtual photon or Z, as depicted in Figure 3.1. The Born-level total cross section for $e^+e^- \to \tau^+\tau^-$ can be written:

$$\sigma_0(s) = \sigma^0_\gamma + \sigma^0_{\gamma Z} + \sigma^0_Z = \frac{4\pi\alpha^2}{3s} F_0(s) \,, \tag{3.1}$$

where

$$F_0(s) \equiv 1 + 2\, g^e_v\, g^\tau_v \,\mathrm{Re}\,\chi(s) + \left(g^{\tau 2}_v + g^{\tau 2}_a\right)\left(g^{e2}_v + g^{e2}_a\right)|\chi(s)|^2 \,, \tag{3.2}$$

decay mode	branching fraction (%) [12]
1 prong decays	84.96 ± 0.14
$e^- \bar{\nu}_e \nu_\tau$	17.83 ± 0.08
$\mu^- \bar{\nu}_\mu \nu_\tau$	17.35 ± 0.10
$\pi^- \nu_\tau$	11.31 ± 0.15
$K^- \nu_\tau$	0.71 ± 0.05
$\pi^- \pi^o \nu_\tau$	25.24 ± 0.16
$h^- 2\pi^o \nu_\tau$	9.50 ± 0.14
$K^{*-}(892) \nu_\tau$	1.28 ± 0.08
3 prong decays	14.91 ± 0.14

Table 3.1: Measured branching fractions of major τ^- lepton decay modes.

and $\chi(s)$ is the Z boson propagator

$$\chi(s) \equiv \frac{s}{s - M_Z^2 + is\Gamma_Z/M_Z} \,. \tag{3.3}$$

The variable s is the squared center-of-mass energy in the e^+e^- collision. The first and third terms in the total cross section (Equation 3.1) represent the contribution from annihilation through a photon and Z respectively, while the middle term is the γ-Z interference term.

The $e^+e^- \to \tau^+\tau^-$ Born-level cross-section, shown in Figure 3.2, contains a large resonance around $\sqrt{s} \approx M_Z$. (How the cross-section varies versus $\sqrt{s}$ around the Z resonance is often called the "Z lineshape".) In this region of center-of-mass energy, the Z-annihilation term dominates the cross-section. The e^+ and e^- annihilate into a real (as opposed to

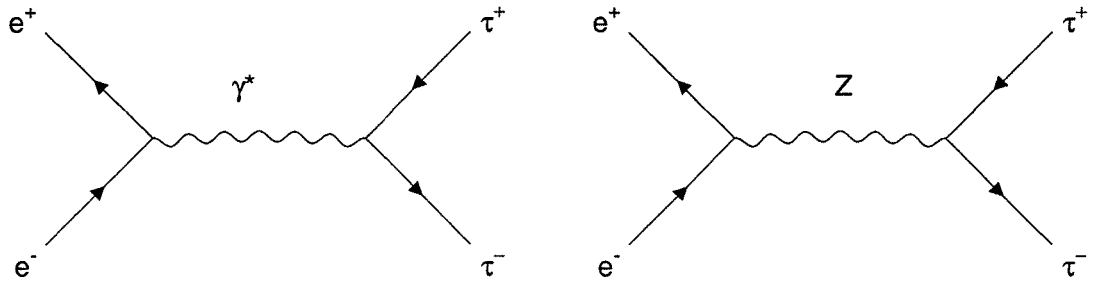

Figure 3.1: Feynman diagrams illustrating the Born-level processes contributing to $e^+e^- \to \tau^+\tau^-$.

virtual) Z boson which can then decay into a $\tau^+\tau^-$ pair. Although the $Z \to \tau^+\tau^-$ branching fraction is only $(3.360 \pm 0.015)\%$ [12], the resonant Z production allows sizeable $\tau^+\tau^-$ samples to be collected.

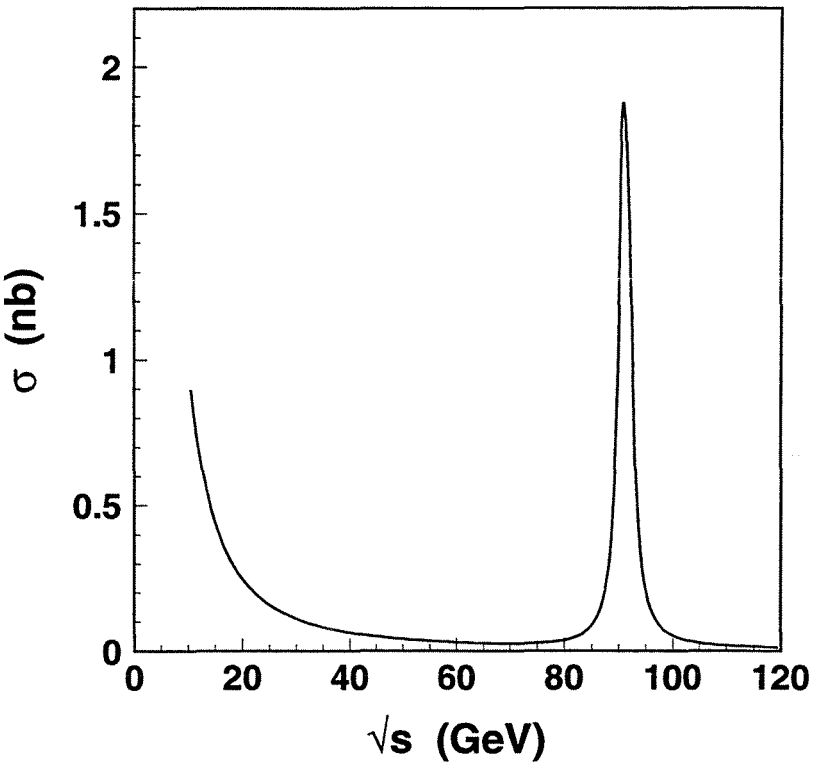

Figure 3.2: The Born-level cross section of $e^+e^- \to \tau^+\tau^-$ as a function of the center-of-mass energy.

In the e^+e^- center-of-mass frame, the τ^+ and τ^- are produced with equal energies in a back-to-back topology in accordance with energy and momentum conservation. When the incoming e^+ and e^- have the same energies, as is the case at LEP, the laboratory frame is identical to the center-of-mass frame, so the τ energies equal the e^+ and e^- energies.

Recall that vector and axial-vector interactions conserve the helicity of interacting fermions in the relativistic limit $E \gg m$. Since the neutral current consists only of vector and axial-vector currents, the helicities of the τ^+ and τ^- produced in e^+e^- annihilations are 100% anticorrelated up to corrections of order m_τ^2/E_τ^2. Hence, the final state helicity configuration is a left-handed τ^+ and a right-handed τ^- or *vice versa*. This helicity

anticorrelation plays a central role in this analysis.

The non-zero axial-vector couplings of the electron and the τ to the Z cause easily observable asymmetries in $e^+e^- \to \tau^+\tau^-$ for $\sqrt{s} \sim M_Z$. In particular, the net longitudinal spin polarization of the τ^+ and τ^- varies as a function of production angle. Moreover, the average polarization is non-zero. This behavior can be extracted from the Born-level differential cross section of $e^+e^- \to \tau^+\tau^-$ which includes the τ helicity dependence

$$\frac{d\sigma}{d\cos\theta} = \frac{\pi\alpha^2}{2s}\Big[\Big(F_0(s) - h_{\tau^-}F_2(s)\Big)\,(1+\cos^2\theta\,) + 2\,\Big(F_1(s) - h_{\tau^-}F_3(s)\Big)\,\cos\theta\Big] \qquad (3.4)$$

where

$$F_1(s) \equiv 2\,\mathrm{Re}\Big(\chi(s)\Big)\,g_a^e g_a^\tau + |\chi(s)|^2\,\Big(2g_v^e g_a^e\Big)\Big(2g_v^\tau g_a^\tau\Big) \qquad (3.5)$$

$$F_2(s) \equiv 2\,\mathrm{Re}\Big(\chi(s)\Big)\,g_v^e g_a^\tau + |\chi(s)|^2\,\Big(g_v^{e\,2} + g_a^{e\,2}\Big)\Big(2g_v^\tau g_a^\tau\Big) \qquad (3.6)$$

$$F_3(s) \equiv 2\,\mathrm{Re}\Big(\chi(s)\Big)\,g_a^e g_v^\tau + |\chi(s)|^2\,\Big(2g_v^e g_a^e\Big)\Big(g_v^{\tau 2} + g_a^{\tau 2}\Big)\,. \qquad (3.7)$$

The polar angle θ is the angle between the τ^- momentum and the e^- direction, while h_{τ^-} denotes the τ^- helicity.

The τ^- polarization $\mathcal{P}_{\tau^-}$ is defined as the asymmetry in the production cross-section of left-handed and right-handed τ^-. As a result of the helicity anticorrelation, the τ^- polarization is opposite that of the τ^+ polarization. By convention, the generic τ polarization $\mathcal{P}_\tau$ refers to the τ^- polarization, *i.e.*, $\mathcal{P}_\tau \equiv \mathcal{P}_{\tau^-} = -\mathcal{P}_{\tau^+}$. The polarization as a function of θ is written:

$$\mathcal{P}_\tau(\cos\theta) \equiv \frac{\left.\frac{d\sigma}{d\cos\theta}\right|_{h_\tau=+1} - \left.\frac{d\sigma}{d\cos\theta}\right|_{h_\tau=-1}}{\left.\frac{d\sigma}{d\cos\theta}\right|_{h_\tau=+1} + \left.\frac{d\sigma}{d\cos\theta}\right|_{h_\tau=-1}} \qquad (3.8)$$

$$= -\frac{F_2(s)(1+\cos^2\theta) + 2F_3(s)\cos\theta}{F_0(s)(1+\cos^2\theta) + 2F_1(s)\cos\theta}\,. \qquad (3.9)$$

Figure 3.3 illustrates how the τ polarization varies over θ. The maximum and minimum polarization occur when the τ^- is produced at far forward and backward θ angles. The average τ polarization measured within a symmetric interval of $\cos\theta$ is simply given by

$$\mathcal{P}_\tau = -\frac{F_2(s)}{F_0(s)} \approx -\frac{2\,g_v^\tau g_a^\tau}{g_v^{\tau 2} + g_a^{\tau 2}} \qquad \text{for } \sqrt{s} \approx M_Z\,. \qquad (3.10)$$

For an effective electroweak mixing angle $\sin^2\theta_w = 0.2324$, the average τ polarization at $\sqrt{s} = M_Z$ has the value $\mathcal{P}_\tau \approx -0.140$. Hence, there is a preference for producing left-handed τ^- (right-handed τ^+) in $Z \to \tau^+\tau^-$ decays.

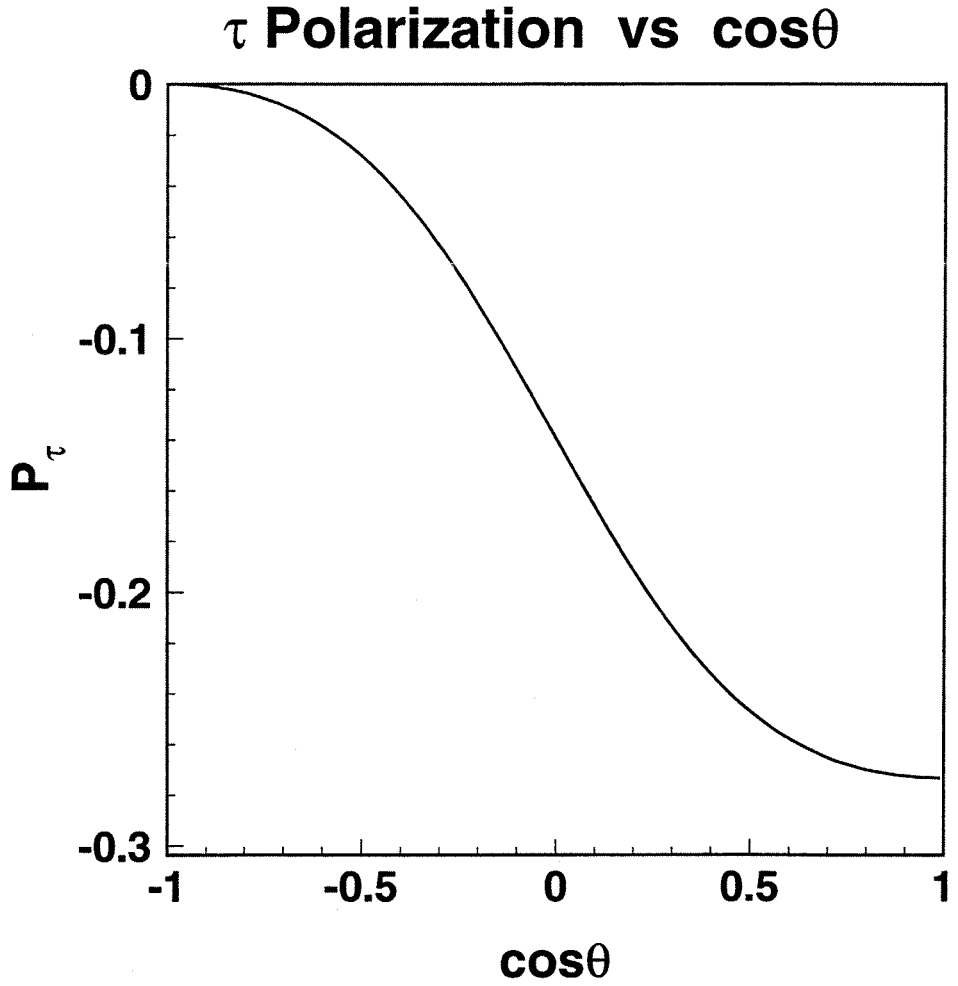

Figure 3.3: The τ polarization as a function of $\cos\theta$ in $e^+e^- \to Z \to \tau^+\tau^-$ events. The angle θ is the angle between the τ^- momentum and the e^- beam direction.

Radiative Corrections

Comparing SM predictions to precise experimental measurements requires including the effects of radiative corrections to the Born-level processes. In $e^+e^- \to f\bar{f}$, the one-loop corrections can be separated into two categories: pure QED corrections and electroweak corrections [17]. The pure QED corrections consist of initial and final state photon radiation, shown in Figure 3.4, and processes containing a virtual photon loop. The electroweak corrections, illustrated in Figure 3.5, involve loops containing virtual fermions (propagator corrections) or virtual W or Z bosons (vertex corrections and box diagrams).

Initial state radiation (ISR) is the process in which an incoming electron or positron emits a photon prior to annihilation. ISR photons are typically emitted within a narrow cone at low angles with respect to the beam direction. Detecting these photons depends on the acceptance of the experimental apparatus. The effect of ISR is to decrease the center-of-mass collision energy which affects many energy-dependent observables, such as the cross section and the τ polarization. These effects can be estimated by convoluting the theoretical cross section (including electroweak corrections) with a radiator function calculated from QED to incorporate the spectrum of ISR photons [18]. ISR reduces the peak cross section of the Z resonance by $\approx 25\%$, shifts the peak position downward by ≈ 110 MeV, and broadens the resonance width asymmetrically (lower half-max position decreases by ≈ 60 MeV, upper half-max shifts upward by ≈ 430 MeV) [18]. The effects on the Z lineshape arising from final state radiation and the interference between initial and final state radiation processes are, in general, small compared to the ISR effects.

The leading effects of the electroweak corrections in $e^+e^- \to Z \to f\bar{f}$ can be incorporated into the improved Born approximation [19] which consists of three modifications of the Born-level theory. First, the QED fine structure constant α becomes s-dependent to account for vacuum polarization effects; at $s \approx M_Z^2$, α has the approximate value $\alpha \approx 1/128$ compared to $\alpha = 1/137$ at low energies. Second, the constant Breit-Wigner width parameter Γ in the Z boson propagator also becomes s-dependent:

$$\Gamma_Z \;\to\; \Gamma_Z(s) = \frac{s}{M_Z^2}\Gamma_Z \,. \tag{3.11}$$

Finally, the electroweak mixing angle is replaced with an effective mixing angle

$$\sin^2\theta_w \;\to\; \sin^2\theta_{\text{eff}} = \sin^2\theta_w + \delta\rho\,\cos^2\theta_w \,, \tag{3.12}$$

where $\delta\rho$ embodies vector boson self-energy and vertex corrections and whose leading term

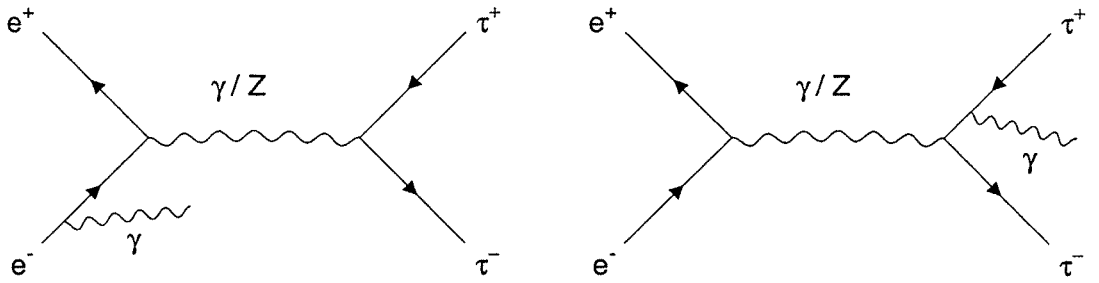

Figure 3.4: Initial (left) and final (right) state radiation processes contributing to QED corrections of $e^+e^- \to \tau^+\tau^-$.

is

$$\delta\rho \approx \frac{\sqrt{2}G_\mu}{16\pi^2} 3m_{\text{top}}^2 . \tag{3.13}$$

The quantity G_μ is the QED radiatively corrected Fermi coupling constant measured in muon decays.

3.3 Decays of the τ Lepton

In the SM, the τ^- decays via emission of a virtual W^- (at the Born-level), as illustrated in Figure 3.6. In addition to a ν_τ, the τ^- decay products could include an electron or muon along with their respective antineutrinos, or a charged meson which could itself decay.

The Lorentz structure of the τ^--ν_τ vertex is the focus of this measurement. The SM predicts a $V-A$ structure, and this prediction can and should be tested. The semileptonic τ^- decays $\tau^- \to h^-\nu_\tau$, where h is a meson, can be used to check $V-A$ and probe for a possible $V+A$ current contribution, as allowed in so-called "left-right symmetric" theories which could extend the SM [20].

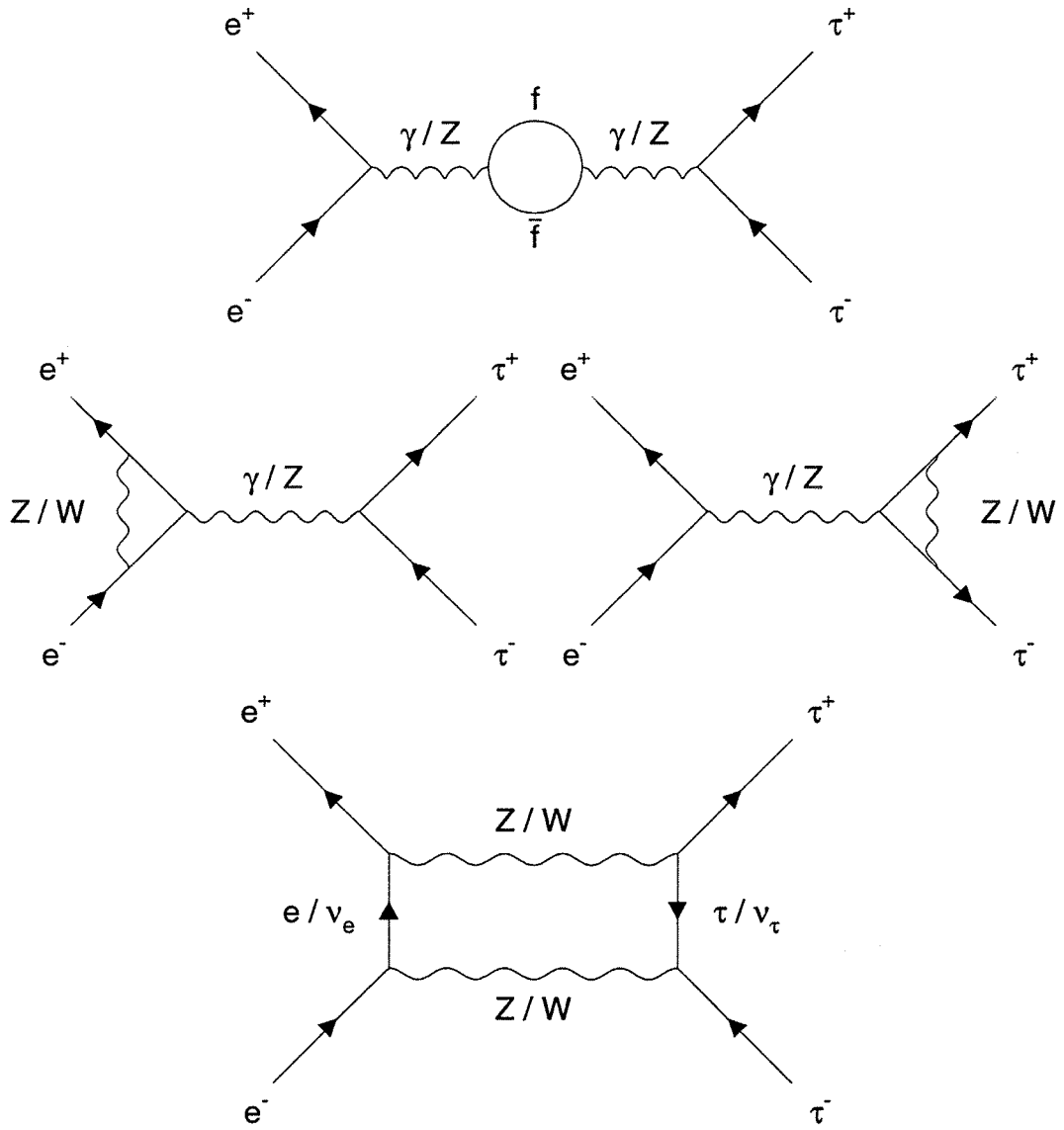

Figure 3.5: Higher order electroweak contributions to $e^+e^- \to \tau^+\tau^-$. The various processes are called propagator corrections (top), vertex corrections (middle), and box diagrams (bottom).

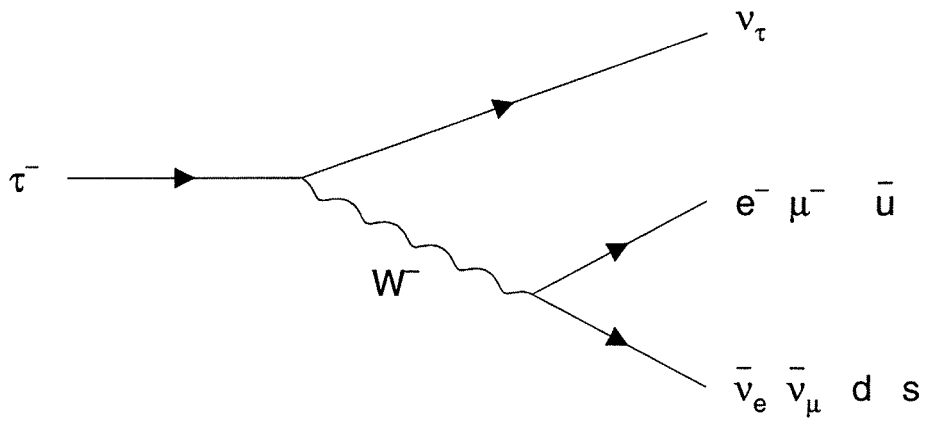

Figure 3.6: The SM Born-level process for τ^- decay. The virtual W^- can materialize as a e^--$\bar{\nu}_e$ or μ^--$\bar{\nu}_\mu$ pair, or a charged meson with quark content $\bar{u}d$ or $\bar{u}s$.

3.3.1 Lorentz Structure of $\tau^- \to h^- \nu_\tau$

The most general matrix element describing $\tau^- \to h^- \nu_\tau$ contains currents of all possible Lorentz structure:

$$\mathcal{M} = \frac{G_F}{\sqrt{2}} \sum_{\substack{\alpha = \\ S,P,V,A,T}} < \bar{h} \, |\Gamma^\alpha| \, 0 >< \bar{\nu}_\tau \, |\Gamma_\alpha| \, \tau > , \tag{3.14}$$

where Γ^α represent scalar, pseudoscalar, vector, axial-vector and tensor interactions. The two factors represent the hadronic and leptonic currents respectively.

It is impractical to investigate all of the Lorentz currents simultaneously, so we make the simplifying assumption that the charged-current consists only of vector and axial-vector interactions. This assumption is motivated by the hadronic current structure, *i.e.*, how the meson couples to the charged current. The $\tau^- \to \pi^- \nu_\tau$, $\tau^- \to K^- \nu_\tau$, and $\tau^- \to \rho^- \nu_\tau$ modes are used in this analysis, because the hadronic current is most reliably known or predicted for these mesons which have $J^P = 0^-$ (π/K) and 1^- (ρ). For $\tau^- \to \pi^- \nu_\tau$ and $\tau^- \to K^- \nu_\tau$, the hadronic current structure can be found from π and K decays. These decays proceed via an axial-vector interaction:

$$\mathcal{M}(\pi^- \to \mu^- \bar{\nu}_\mu) \quad \propto \; < \pi(p) | \gamma^\mu \gamma^5 | \, 0 > \; = \; i\sqrt{2} \, f_\pi \, p^\mu \cos\theta_C \tag{3.15}$$

$$\mathcal{M}(\mathrm{K}^- \to \mu^- \bar{\nu}_\mu) \quad \propto \quad < \mathrm{K}(p)|\gamma^\mu\gamma^5|\,0 > \;=\; i\sqrt{2}\, f_\mathrm{K}\, p^\mu \sin\theta_C \;, \tag{3.16}$$

where f_π and f_K are the pion and kaon decay constants, and θ_C is the Cabibbo mixing angle between the d and s quarks. Specifically, the most general coupling is a combination of axial-vector and pseudoscalar currents. However, the pseudoscalar coupling is excluded to a very high degree of accuracy from the ratio of the measured branching fractions of $\pi^-(\mathrm{K}^-) \to \mathrm{e}\bar{\nu}_\mathrm{e}$ and $\pi^-(\mathrm{K}^-) \to \mu\bar{\nu}_\mu$ decays. The ρ^- is assumed to have a vector coupling to the charged-current, as is the case for the ρ^0 in $\mathrm{e}^+\mathrm{e}^- \to \gamma^* \to \rho^0$. The ρ^- charged-current structure is related to the $\rho^0 - \gamma^*$ coupling by an electroweak isospin rotation. The hadronic current structure of mesons with $J^P = 1^+$, *e.g.* $\tau^- \to a_1^- \nu_\tau$, and strange mesons with $J^P = 1^-$, *e.g.* $\tau^- \to K^{*-}\nu_\tau$, cannot be predicted as reliably, so τ decays involving these mesons are not used in this analysis.

Under the assumption that the charged-current contains only vector and axial-vector interactions, the $\tau^- \to h^-\nu_\tau$ matrix element in Equation 3.14 can be simplified to

$$\mathcal{M} = \frac{G_F}{\sqrt{2}} < \bar{h} \,|\, v_h\Gamma^V + a_h\Gamma^A \,|\, 0 >< \bar{\nu}_\tau \,|\, v_\tau\Gamma^V + a_\tau\Gamma^A \,|\, \tau > \;, \tag{3.17}$$

where v_τ and a_τ denote the τ's vector and axial-vector charged-current couplings, and v_h and a_h are the analogous couplings for the hadron h. The chirality parameter ξ_h is defined as

$$\xi_h \;\equiv < h_{\nu_\tau} > = \frac{2\ \mathrm{Re}(v_\tau a_\tau^*)}{|v_\tau|^2 + |a_\tau|^2} \;, \tag{3.18}$$

and can be interpreted as the ν_τ helicity. In the SM, the $V{-}A$ charged-current structure results in left-handed ν_τ and $\xi_h = -1$. Right-handed ν_τ would arise from a $V{+}A$ current indicated by $\xi_h = +1$. Deviations of $|\xi_h|$ from 1 would indicate an admixture of $V{-}A$ and $V{+}A$ in the charged-current coupling of the τ. Equivalently, one could say that the ν_τ has a right-handed helicity state.

As will be demonstrated in the following subsections, the Lorentz structure of the τ charged-current coupling affects the angular distribution of the daughter hadron in the τ rest frame. The Lorentz boost due to the τ's momentum maps the rest frame angular distribution to the energy distribution in the lab frame. Tsai first investigated the observable distributions in heavy lepton decays in 1971 [21]. In general, the distribution of some observable quantity x_h in semileptonic $\tau^\pm$ decays decays can be written

$$\frac{1}{\Gamma}\frac{d\Gamma}{dx_h} \;=\; f_h(x_h) \pm h_{\tau^\pm}\, \xi_h\, g_h(x_h) \;, \tag{3.19}$$

where $h_{\tau\pm} = \pm 1$ denotes the helicity of the $\tau^{\pm}$, while f_h and g_h are kinematic functions which depend on the hadron h. Under the notion of universality in τ decays, the chirality parameters in $\tau^- \to \pi^-\nu_\tau$ and $\tau^- \to \rho^-\nu_\tau$ decays should be identical, although the possibility of unequal chirality parameters (ξ_π and ξ_ρ) will be considered.

The f and g kinematic functions are calculated using a sample of simulated events generated with a $V-A$ charged-current coupling of the τ. The functional form of the decay spectra for left and right-handed τ decays are given by Equation 3.19 with $h_{\tau\pm} = -1$ and $h_{\tau\pm} = +1$, respectively. Note that the decay spectra are identical for right-handed τ^+ and left-handed τ^-, and *vice versa*. Based on Equation 3.19, f and g can be expressed as:

$$f_h(x_h) = \frac{1}{2}\left(\frac{1}{\Gamma}\frac{d\Gamma(\tau_R^-)}{dx_h} + \frac{1}{\Gamma}\frac{d\Gamma(\tau_L^+)}{dx_h}\right) + \frac{1}{2}\left(\frac{1}{\Gamma}\frac{d\Gamma(\tau_L^-)}{dx_h} + \frac{1}{\Gamma}\frac{d\Gamma(\tau_R^+)}{dx_h}\right) \quad (3.20)$$

$$g_h(x_h) = \frac{1}{2}\left(\frac{1}{\Gamma}\frac{d\Gamma(\tau_R^-)}{dx_h} + \frac{1}{\Gamma}\frac{d\Gamma(\tau_L^+)}{dx_h}\right) - \frac{1}{2}\left(\frac{1}{\Gamma}\frac{d\Gamma(\tau_L^-)}{dx_h} + \frac{1}{\Gamma}\frac{d\Gamma(\tau_R^+)}{dx_h}\right) \quad (3.21)$$

3.3.2 $\tau^- \to \pi^- \nu_\tau$ Decays

The decay $\tau^- \to \pi^- \nu_\tau$ is the simplest hadronic τ decay to describe. Conservation of momentum demands the π^- and ν_τ momenta in the τ^- rest frame are equal in magnitude, *i.e.*, $|\vec{p}_{\pi^-}| = |\vec{p}_{\nu_\tau}| = \frac{1}{2} m_\tau (1 - m_\pi^2/m_\tau^2)$. Figure 3.7 illustrates the spin configuration for a right-handed τ^- in a $V-A$ $\tau^- \to \pi^- \nu_\tau$ decay. Since the π is a pseudoscalar (spin 0) particle, the ν_τ must carry all the spin, so the π^- is preferentially emitted parallel to the τ^- spin axis. The opposite is true for a left-handed τ^- in a $V-A$ decay, or a right-handed τ^- in a $V+A$ decay. For $\tau^+ \to \pi^+ \bar{\nu}_\tau$ decays, the π^+ direction is opposite to that of the π^- in the same configuration.

The π^- angular distribution in the τ^- rest frame can be written

$$\frac{1}{\Gamma}\frac{d\Gamma(\tau^- \to \pi^- \nu_\tau)}{d\cos\theta^*} = 1 \pm h_{\tau\pm}\, \xi_h \cos\theta^* \,. \quad (3.22)$$

Under a Lorentz transformation from the τ rest frame to the lab frame, the cosine of the decay angle θ^* can be expressed in terms of the pion energy:

$$\cos\theta^* = \frac{2x_\pi - 1 - m_\pi^2/m_\tau^2}{\beta_\tau\,(1 - m_\pi^2/m_\tau^2)} \approx 2x_\pi - 1 \,, \quad (3.23)$$

where $x_\pi \equiv E_\pi/E_\tau$ and $\beta_\tau = \sqrt{1 - m_\tau^2/E_\tau^2}$ is the τ lepton velocity in the lab frame. To obtain the approximate result, note $m_\pi/m_\tau \ll 1$ and $\beta_\tau \approx 1$ since in $e^+e^- \to Z \to \tau^+\tau^-$,

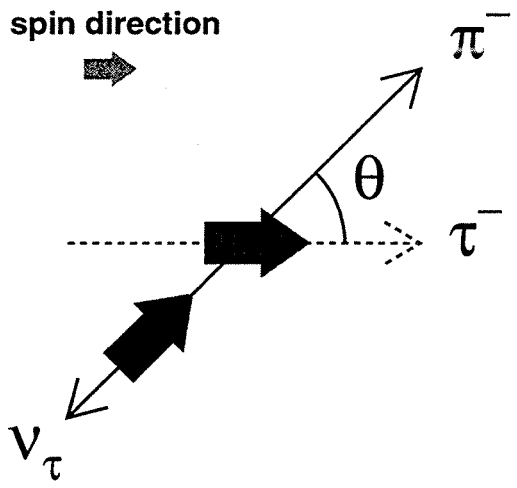

Figure 3.7: Spin configuration for right-handed τ^- in $V-A$ $\tau^- \to \pi^- \nu_\tau$. The solid arrows indicate spin directions, while the dotted arrow denotes the flight direction of the τ^-. For left-handed ν_τ, *i.e.*, $V-A$ charged-current, the π^- is preferentially emitted along the τ^- flight direction.

the τ energy ($\approx$ 45 GeV) is much greater than its mass ($\approx$ 1.78 GeV). Armed with the above relation for $\cos\theta^*$, we can now write an approximate expression for the pion energy distribution in the lab frame:

$$\frac{1}{\Gamma}\frac{d\Gamma(\tau^- \to \pi^- \nu_\tau)}{dx_\pi} = 1 - h_{\tau\pm}\xi_h(2x_\pi - 1)\,. \tag{3.24}$$

This equation matches the form of Equation 3.19, and we can identify the kinematic functions for $\tau^- \to \pi^- \nu_\tau$ as $f_\pi(x_\pi) = 1$ and $g_\pi(x_\pi) = 2x_\pi - 1$. These analytic results are valid only in the Born approximation, but higher order corrections do not alter the kinematic functions very much. Figure 3.8 shows the analytic approximations for f_π and g_π in addition to their forms as calculated from a Monte-Carlo event generator which incorporates higher order radiative processes. Figure 3.9 illustrates the x_π spectra for left and right-handed $\tau^- \to \pi^- \nu_\tau$ decays assuming a $V-A$ charged-current coupling of the τ.

3.3.3 $\tau^- \to \rho^- \nu_\tau$ Decays

The decay $\tau^- \to \rho^- \nu_\tau$ is more complicated than $\tau^- \to \pi^- \nu_\tau$ because the ρ meson is a vector (spin 1) particle which itself decays predominantly into a charged and neutral pion.

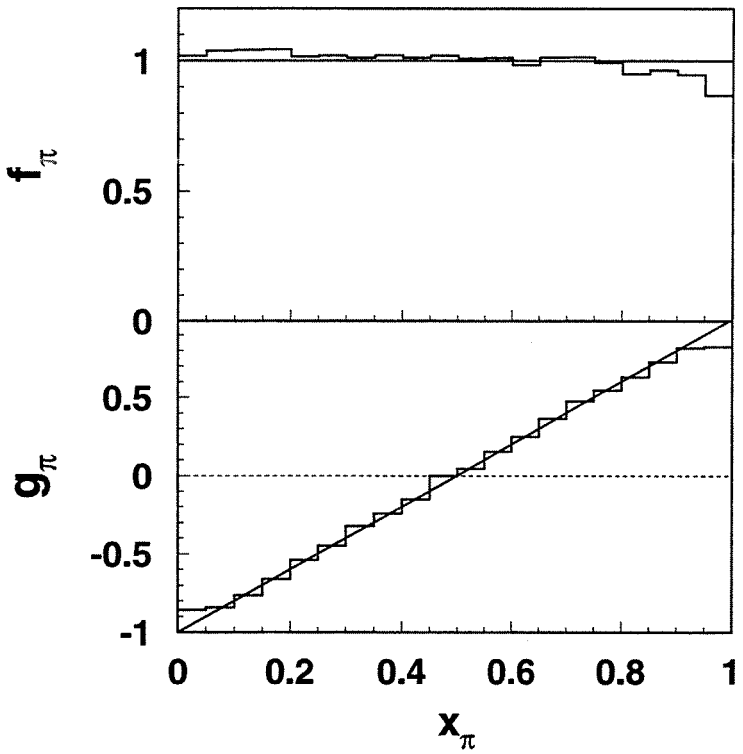

Figure 3.8: The f and g kinematic functions for $\tau^- \to \pi^- \nu_\tau$ decays. The solid lines denote the analytic approximations, while the histograms represent the functions calculated from a Monte-Carlo event generator which includes the effects of initial and final state radiation.

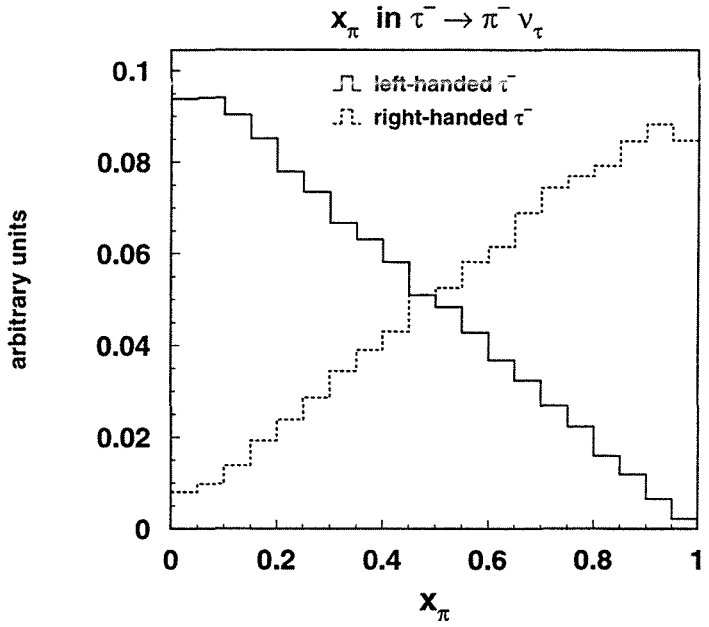

Figure 3.9: The x_π spectra from left-handed and right-handed $\tau^- \to \pi^-\nu_\tau$ assuming $V-A$ charged-current coupling.

The ρ is a broad resonance with mass $m_\rho = 768.5$ MeV and width $\Gamma = 150.7$ MeV [12]. As depicted in Figure 3.10, the two allowed ρ^- longitudinal spin projection states have opposite effects on the decay angle θ^* and, hence, the ρ^- energy in the lab frame. When $s_z = 0$ for the ρ, the configuration is identical to $\tau^- \to \pi^-\nu_\tau$, and the preferred ρ^- flight direction is parallel to the τ^- lab momentum. For a polarized $s_z = -1$ state, the ρ^- momentum is antiparallel to the τ^- momentum. The $\cos\theta^*$ distributions for left and right-handed $\tau^- \to \rho^-\nu_\tau$ are given by

$$\frac{1}{\Gamma}\frac{d\Gamma(\tau^- \to \rho^-\nu_\tau)}{d\cos\theta^*} \approx 1 - \alpha \mathcal{P}_\tau \xi_\rho \cos\theta^* ,$$

where

$$\cos\theta^* \approx \frac{4\,m_\tau^2}{m_\tau^2 - m_\rho^2}\frac{E_{\pi^-} + E_{\pi^0}}{\sqrt{s}} - \frac{m_\tau^2 + m_\rho^2}{m_\tau^2 - m_\rho^2} \tag{3.25}$$

and $\alpha = \frac{m_\tau^2 - 2m_\rho^2}{m_\tau^2 + 2m_\rho^2} \approx 0.46$. The factor α embodies the loss of sensitivity of $\cos\theta^*$ to the τ polarization caused by the two competing ρ^- helicity states. The sensitivity loss can be seen in the $\cos\theta^*$ distributions in Figure 3.11. If there were only one allowed ρ^- helicity state, the spectra would be steeper; compare to Figure 3.9 in which the x_π variable has maximal sensitivity to the τ^- polarization in $\tau^- \to \pi^-\nu_\tau$.

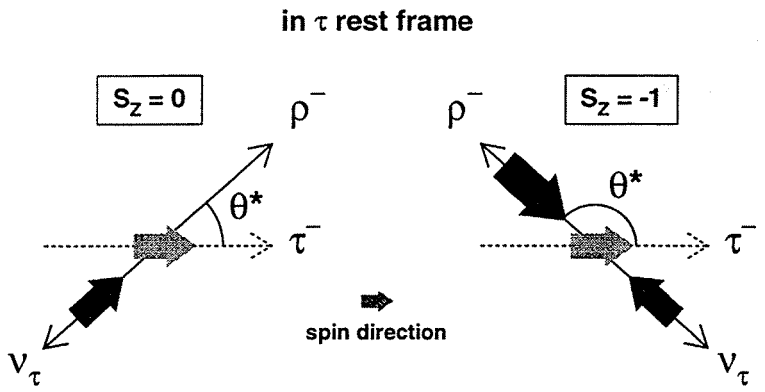

Figure 3.10: The favored spin configurations in $\tau^- \to \rho^- \nu_\tau$. The solid arrows indicate the direction of the longitudinal spin projection, and the dashed lines denote the τ^- momentum direction. When the ρ^- is in the $s_z = 0$ ($s_z = -1$) spin state, the preferred ρ^- direction is parallel (antiparallel) to the τ^- direction.

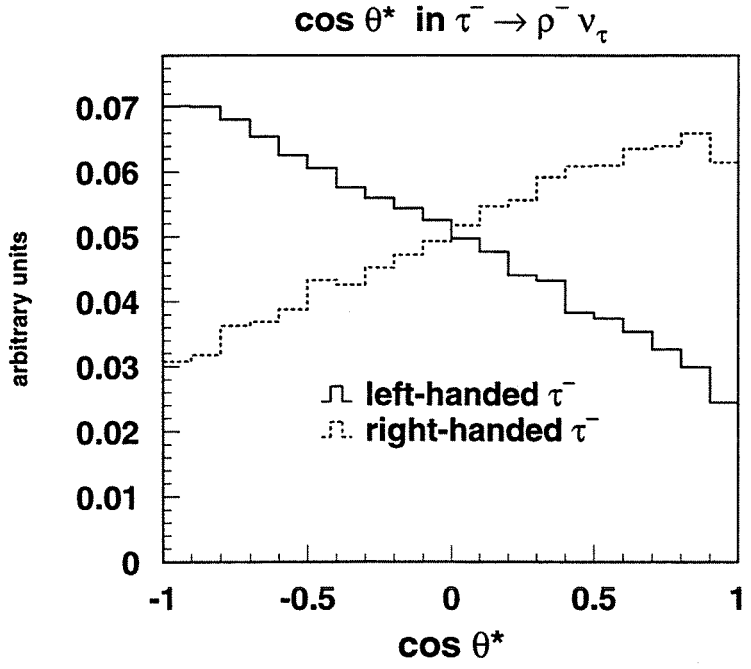

Figure 3.11: The $\cos\theta^*$ distributions for left-handed and right-handed $\tau^- \to \rho^- \nu_\tau$.

The τ polarization sensitivity lost from the $\cos\theta^*$ distribution can be nearly regained by also analyzing the $\rho^- \to \pi^-\pi^o$ decay. Just as θ^* depends on the τ^- helicity, the angle ψ^*, which is the angle between the π^- momentum in the ρ^- rest frame and ρ^- flight direction in the lab frame, depends on the longitudinal spin projection state of the ρ^-. The cosine of ψ^* is proportional to the difference of the π^- and π^o lab frame energies:

$$\cos\psi^* \approx \frac{m_\rho}{\sqrt{m_\rho^2 - (m_{\pi^-} + m_{\pi^o})^2}} \frac{E_{\pi^-} - E_{\pi^o}}{|\vec{p}_{\pi^-} + \vec{p}_{\pi^o}|}, \tag{3.26}$$

where $\vec{p}_{\pi^-}$ and $\vec{p}_{\pi^o}$ denote the lab frame momenta of the π^- and π^o respectively. Figure 3.12 illustrates the sensitivity of $\cos\psi^*$ to the τ^- helicity.

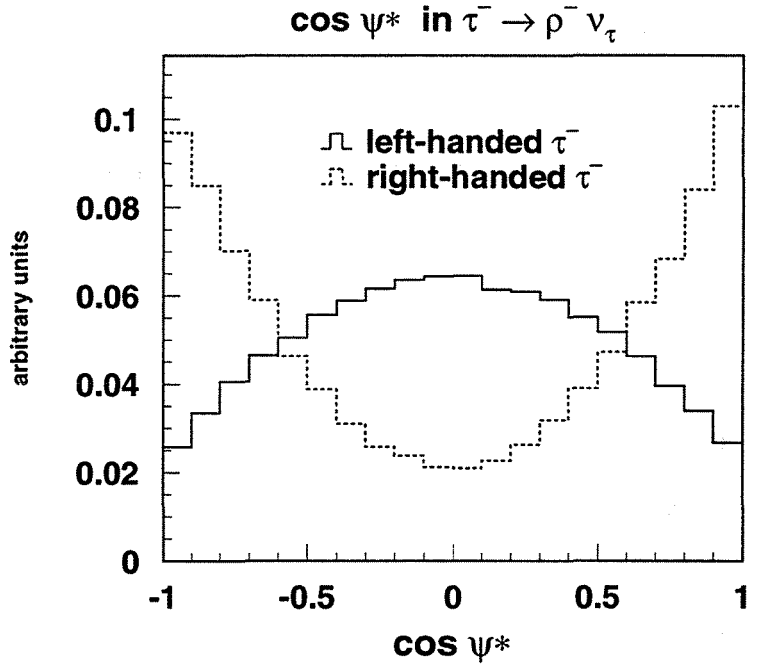

Figure 3.12: The $\cos\psi^*$ distributions for left-handed and right-handed $\tau^- \to \rho^-\nu_\tau$.

The two-dimensional $(\cos\theta^*, \cos\psi^*)$ distribution from $\tau^- \to \rho^-\nu_\tau$ has a better sensitivity to τ polarization than $\cos\theta^*$ has alone. However, using the $(\cos\theta^*, \cos\psi^*)$ distribution in this analysis would be cumbersome since the correlations between both τ leptons in $Z \to \tau^+\tau^-$ are exploited. Analysis of events in which both τ decay to $\rho\nu_\tau$ would require a 4-dimensional distribution $(\cos\theta_1^*, \cos\psi_1^*, \cos\theta_2^*, \cos\psi_2^*)$. Fitting such a distribution is complicated by the dimensionality and the reduced number of entries per bin when dealing with

low statistics.

Fortunately, the $\tau^- \to \rho^- \nu_\tau$ dynamics can be expressed in terms of a single variable with no intrinsic loss of sensitivity to the τ polarization. The quantity ω is derived from the two-dimensional $\tau^- \to \rho^- \nu_\tau$ decay distribution expressed in terms of $\cos\theta^*$ and $\cos\psi^*$ [22]. Appendix A contains the complicated analytic expression for ω, and Figure 3.13 illustrates the ω distributions for $\tau^- \to \rho^- \nu_\tau$ from left and right-handed τ^-. Using the observable ω, one can write a one-dimensional decay distribution for $\tau^- \to \rho^- \nu_\tau$ in the form of Equation 3.19:

$$\frac{1}{\Gamma}\frac{d\Gamma}{d\omega} = f_\rho(\omega) \pm h_{\tau\pm}\,\xi_h\, g_\rho(\omega)\,, \tag{3.27}$$

where f_ρ and g_ρ are the kinematic functions for $\tau^- \to \rho^- \nu_\tau$ shown in Figure 3.14.

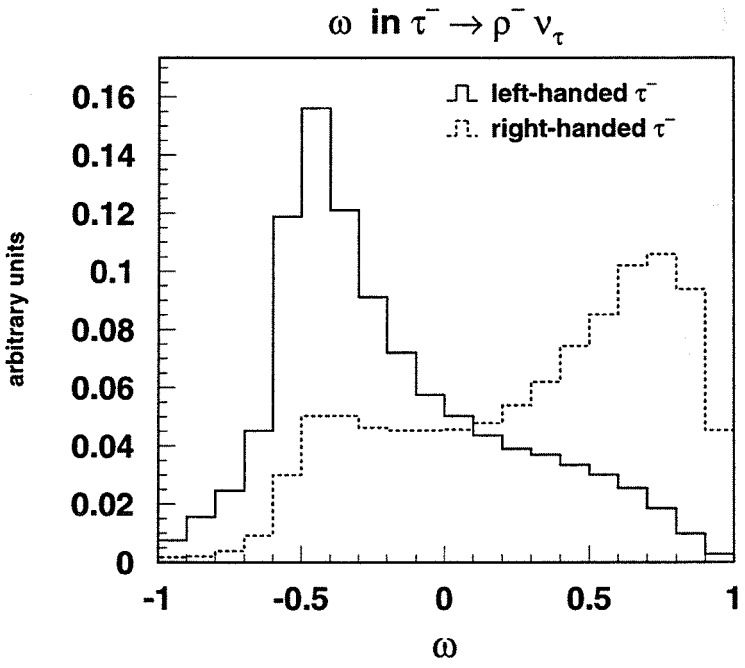

Figure 3.13: The ω spectra from left-handed and right-handed $\tau^- \to \rho^- \nu_\tau$ assuming $V-A$ charged-current coupling.

3.4 $\tau^+\tau^-$ Correlation Distributions

Tsai first described the decay correlations of heavy leptons in $e^+e^- \to \ell^+\ell^-$ assuming a universal $V-A$ charged-current structure [21]. Nelson promoted the use of $\tau^+\tau^-$

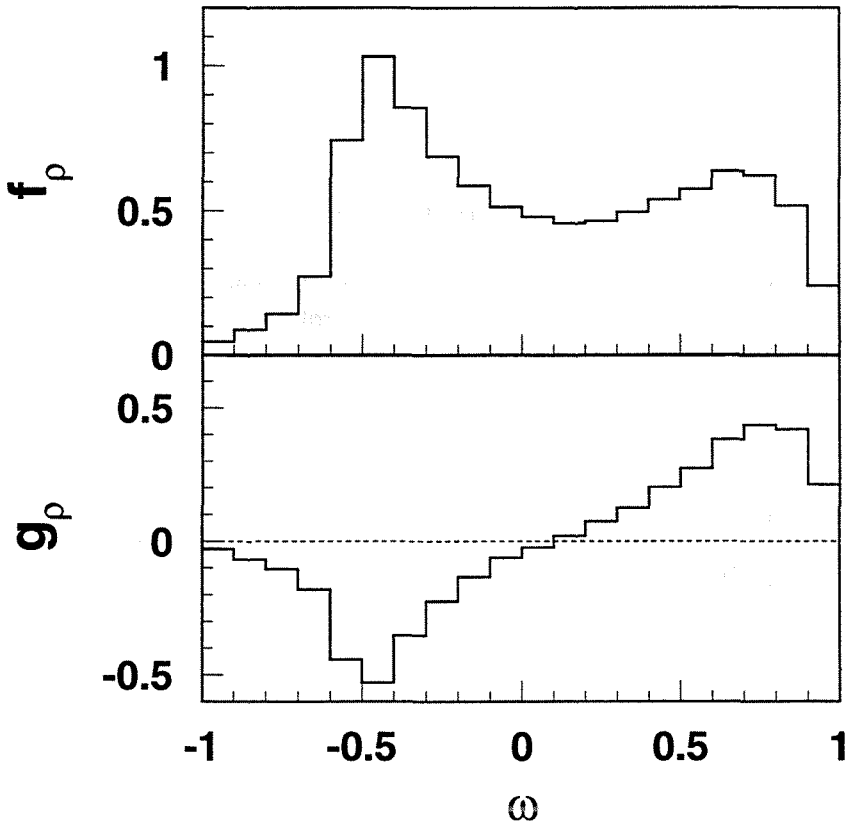

Figure 3.14: The f and g kinematic functions for $\tau^- \to \rho^- \nu_\tau$ decays.

correlations to investigate the charged-current Lorentz structure [23]. The decay distributions for individual τ decays (Equation 3.19) depend only on the product $\mathcal{P}_\tau \xi_h$, so they alone cannot be used to measure τ polarization and the chirality parameter independently. However, by exploiting the correlations between the τ^- and τ^+ it is possible to measure $\mathcal{P}_\tau$ and ξ independently. The correlation decay distribution for $e^+e^- \to Z \to \tau^+\tau^- \to A^\pm B^\mp \nu_\tau \bar{\nu}_\tau$, where A and B represent final state hadrons π/K or ρ, can be written [24]:

$$\begin{aligned} \frac{1}{\Gamma}\frac{d^2\Gamma}{dx_A\,dx_B} &= f_A(x_A)\,f_B(x_B) + \xi_A\xi_B\,g_A(x_A)\,g_B(x_B) \\ &- \mathcal{P}_\tau\left[\xi_B\,f_A(x_A)\,g_B(x_B) + \xi_A\,f_B(x_B)\,g_A(x_A)\right]. \end{aligned} \tag{3.28}$$

The variables x_A and x_B are the appropriate polarization-sensitive variables for the τ decay mode involving hadrons A or B. Under the assumption of universality, $\xi_A = \xi_B \equiv \xi_h$. Note that the second term of Equation 3.28 depends on ξ, but not $\mathcal{P}_\tau$; it is this term that makes it possible to simultaneously measure the chirality parameter and the τ polarization.

However, one cannot unambiguously determine the signs of $\mathcal{P}_\tau$ and ξ_h using the correlation distribution. This can be seen by making the substitutions $\mathcal{P}_\tau \to -\mathcal{P}_\tau$, $\xi_A \to -\xi_A$ and $\xi_B \to -\xi_B$ into Equation 3.28; the resulting equation is identical. As previously mentioned, this sign ambiguity prevents a distinction between pure $V{-}A$ and $V{+}A$ charged-current coupling of the τ, but a chirality parameter magnitude differing from unity indicates a mixture of $V{-}A$ and $V{+}A$. The signs of $\mathcal{P}_\tau$ and ξ are chosen to be negative based on the results of other experiments which can measure the sign of either parameter unambiguously. Thanks to the highly polarizable e^- beams at the Stanford Linear Collider (SLC), the SLD experiment can determine both the magnitude and sign of the τ neutral-current coupling asymmetry $\mathcal{A}_\tau$ (hence, $\mathcal{P}_\tau$), as well as the chirality parameter [25, 26]. However, their measurement of the chirality parameter magnitude is less precise than this measurement due to their smaller data sample. The $\tau^- \to a_1^-\nu_\tau$ decay has also been used to extract the sign of the chirality parameter [27, 28].

In this analysis, there are three correlated decay distributions to consider which correspond to the $\rho\rho$, $\pi\pi$ and $\rho\pi$ event classifications. As an example, Figure 3.15 shows the $\rho\pi$ correlated decay distribution for the f and g kinematic functions assuming $\mathcal{P}_\tau = -0.134$ and $\xi_\pi = -1$. Looking at projections of the correlated decay distributions is also useful; Figure 3.16 displays several x_π and ω projections of the $\rho\pi$ distribution in Figure 3.15. The τ^+ and τ^- helicity correlations are evident in this plot. The plots on top of each column correspond to x_π/ω ranges characteristically populated by τ_L^-/τ_R^+ decays; the ω/x_π spectra

also indicate an enhancement of τ_R^+/τ_L^- decays. Proceeding downward in the columns, the x_π/ω ranges correspond to higher ratios of τ_R^-/τ_L^+; the ω/x_π spectra also reflect an increasing ratio of τ_R^-/τ_L^+. As the chirality parameter magnitude diminishes, the τ^+ and τ^- helicity correlation decreases also, as illustrated for $\xi = -0.5$ in Figure 3.17. The top and bottom plots do not reflect highly polarized τ populations, and the changes between the plots proceeding downward in each column is less dramatic than for $\xi = -1$. In the extreme case of $\xi = 0$, *i.e.*, no correlation, the ω/x_π spectra would be identical in each x_π/ω region.

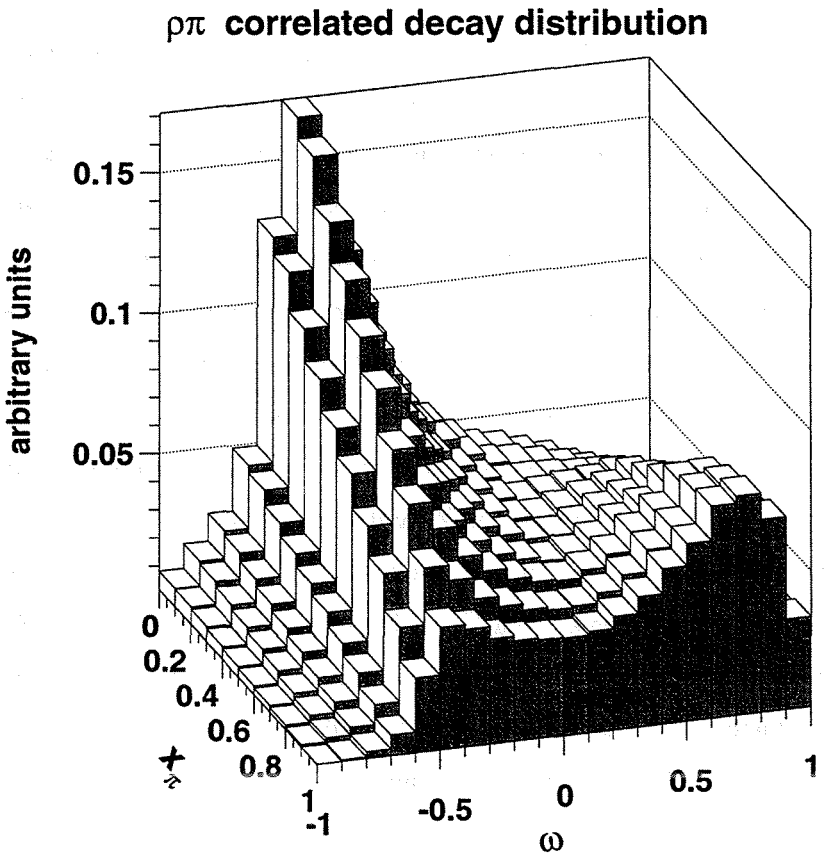

Figure 3.15: The $\rho\pi$ correlated decay distribution assuming $\mathcal{P}_\tau = -0.134$ and $\xi = -1$.

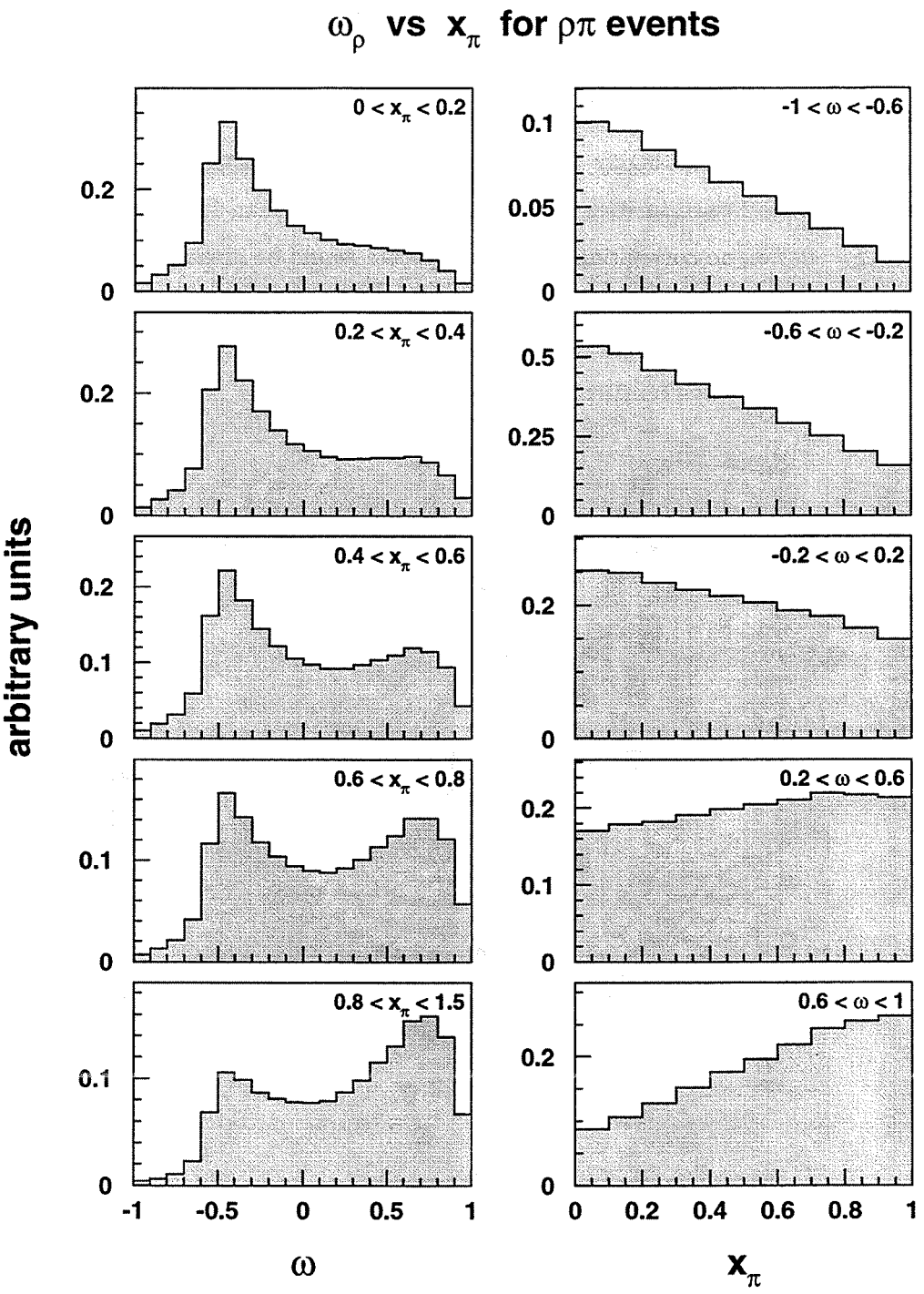

Figure 3.16: Projection bands of the $\rho\pi$ correlated decay distribution assuming $\mathcal{P}_\tau = -0.134$ and $\xi = -1$.

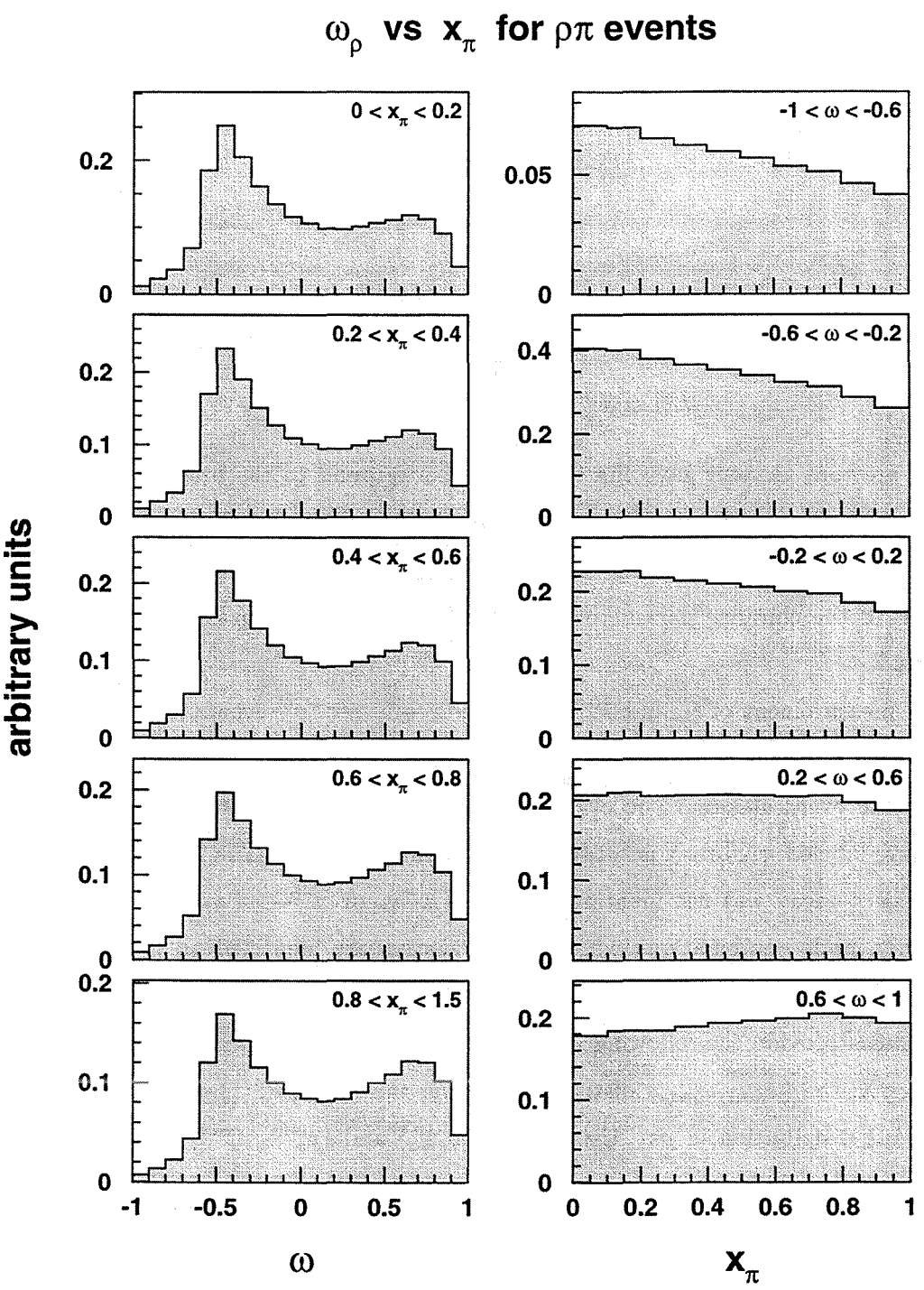

Figure 3.17: Projection bands of the $\rho\pi$ correlated decay distribution assuming $\mathcal{P}_\tau = -0.134$ and $\xi = -0.5$.

CHAPTER 4

EXPERIMENTAL METHOD OF THE MEASUREMENT

The previous chapter gave the theoretical background to the production of $\tau^+\tau^-$ pairs, the decays $\tau^- \to \pi^-\nu_\tau$ and $\tau^- \to \rho^-\nu_\tau$, and the correlations between the τ^+ and τ^- in a $e^+e^- \to Z \to \tau^+\tau^-$ event. This chapter demonstrates how to make an experimental measurement of the chirality parameter ξ_h and the average τ polarization $\mathcal{P}_\tau$ from those distributions.

This measurement of ξ_h and $\mathcal{P}_\tau$ requires $e^+e^- \to Z \to \tau^+\tau^-$ events in which at least one of the two τ's decays is identified as $\tau^- \to \pi^-\nu_\tau$ or $\tau^- \to \rho^-\nu_\tau$. Consequently, there are five possible event classes. The events which have only one identified $\tau^- \to \pi^-\nu_\tau$ or $\tau^- \to \rho^-\nu_\tau$ are labeled πX or ρX according to the identified decay. The X simply indicates that the other τ decay was not identified as $\tau^- \to \pi^-\nu_\tau$ or $\tau^- \to \rho^-\nu_\tau$. There are three possible decay mode combinations when both τ decays are identified as $\tau^- \to \pi^-\nu_\tau$ or $\tau^- \to \rho^-\nu_\tau$, and they are straightforwardly labeled $\rho\rho$, $\pi\pi$ or $\rho\pi$. For completeness, the five event classes provide the following decay distributions: the ω spectrum in ρX, the x_π spectrum in πX, the $(\omega_{min}, \omega_{max})$ distribution in $\rho\rho$, the $(x_\pi^{min}, x_\pi^{max})$ distribution in $\pi\pi$, and the (ω, x_π) distribution in $\rho\pi$. Using $(\omega_{min}, \omega_{max})$ and $(x_\pi^{min}, x_\pi^{max})$ distributions for $\rho\rho$ and $\pi\pi$ events precludes the need to consider the sign of the parent τ and assumes that CP, the combined operation of charge conjugation and parity, is not violated in τ decays, in agreement with current observations.

The observed decay spectra differ from the ideal theoretical ones described in Chapter 3 due to several experimental effects which were not incorporated there. These effects include event selection inefficiencies, non-zero backgrounds and finite resolution of the experimental apparatus. These effects will be qualitatively described here and quantitatively analyzed in a later chapter.

As stated previously, this analysis is based on a sample of $e^+e^- \rightarrow Z \rightarrow \tau^+\tau^-$ events in which at least one of the τ's decays into $\pi\nu$ or $\rho\nu$. Such events are only a fraction of the possible final states in e^+e^- annihilations. Ideally, one would hope to record and identify 100% of the desired events while rejecting all the unwanted events, but that is not practical experimentally. Without a detector that spans the complete 4π steradians in solid angle, final state particles traveling outside of the detector volume are simply lost. Typical collider experiments can cover up to 99% of 4π solid angle. Another source of inefficiency are gaps within the detector volume which could arise from malfunctions in an active detector element, or they could be physical gaps or insensitive regions between components. Selection inefficiencies are also introduced by analysis cuts which are usually intended to reduce the amount of unwanted background events in the event sample.

The background events in this analysis are classified into two categories: τ and non-τ background. The τ background consists of $Z \rightarrow \tau^+\tau^-$ events in which at least one of the τ decays has been misidentified. The non-τ background are events which are *not* $Z \rightarrow \tau^+\tau^-$ decays. This background mainly includes $Z \rightarrow e^+e^-$ (Bhabha events), $Z \rightarrow \mu^+\mu^-$ (dimuon events), $e^+e^- \rightarrow e^+e^- f\bar{f}$ ($\gamma\gamma$, or two-photon events), and cosmic rays passing through the experiment.

Another experimental effect to consider is the finite resolution of the detector. The theoretical decay distributions in Chapter 3 assumed infinitely precise energy and coordinate measurements from the apparatus. The finite experimental resolutions not only affect the ideal decay spectra, but also contribute to the selection inefficiencies and background in the data sample.

All of the above experimental issues alter the relevant decay spectra used in this analysis. In order to make a reliable measurement of ξ_h and $\mathcal{P}_\tau$, these effects need to be incorporated or folded into theoretical distributions. To do that, we rely on simulations of the relevant physics processes and the detector response.

The Monte-Carlo program KORALZ [29,30] generates the process $e^+e^- \rightarrow \gamma^*/Z \rightarrow \tau^+\tau^-$ via Standard Model processes and includes the effects of multiple initial and final state radiation, one-loop weak radiative corrections, and longitudinal τ polarization. The TAUOLA [31,32] program is used to model the signal and background τ decay modes, and it assumes a $V-A$ charged-current coupling of the τ. The four-vectors of the final state particles obtained from the event generator software are then used as input to the detector simulation (described in Chapter 6) which models the detector response.

The fully simulated $\tau^+\tau^-$ events are analyzed to select those events in which at least one τ decay is identified as $\tau^- \to \pi^-\nu_\tau$ or $\tau^- \to \rho^-\nu_\tau$, based on the selection criteria discussed in Chapter 7. These events are then classified into one of the five event classes used in the analysis. Since the actual τ decay modes are known in each Monte-Carlo event, the selection efficiency and backgrounds from misidentified τ decays can be estimated.

The decay spectra from the simulated $\tau^+\tau^-$ events are used to construct the f and g kinematic functions which include selection inefficiencies, misidentified τ decays and experimental resolutions. (The non-τ background is studied separately. This topic will be addressed in Chapter 7.) The handedness of each τ is known in the simulated events, so the f and g functions are obtained from Equations 3.21 using the decay spectra of left-handed and right-handed τ decays. Each event class has its own f and g functions. For the $\rho\rho$ and $\pi\pi$ classes, both ρ's and π's are used to calculate a single set of f and g functions, while a pair of f and g functions are needed for the $\rho\pi$ class, one for the ρ and one for the π.

Figures 4.2 through 4.4 illustrate the effects of selection inefficiencies, backgrounds, and experimental resolution on the x_π and ω distributions, and the respective f and g functions, for the πX and ρX event classes. Compare these plots to the ideal theoretical ones in Figures 3.8, 3.9, 3.13 and 3.14. The greatest effect is seen in the $\tau^- \to \pi^-\nu_\tau$ spectrum, which is affected by degraded selection efficiency at low π energy and by energy resolution for large π energy. The finite energy resolution softens the kinematic energy cutoff at $x_\pi = 1$ and accounts for measured E_π above the maximum possible true π energy. The ω spectra and $\tau^- \to \rho^-\nu_\tau$ kinematic functions are not as seriously altered by the experimental effects.

To make the measurement of ξ_h and $\mathcal{P}_\tau$, the observed decay spectra from the five event classes are simultaneously fit to the respective distributions constructed with the f and g obtained from the Monte-Carlo event sample. The fit is performed with a binned maximum likelihood method using a Poisson-based likelihood function

$$\mathcal{L}(\mu; n) \;=\; \prod_i \prod_j \frac{(\mu_{ij})^{n_{ij}}\, e^{-\mu_{ij}}}{n_{ij}!}\,, \tag{4.1}$$

where the index i represents the decay distribution (ρX, πX, $\rho\rho$, $\pi\pi$, $\rho\pi$), and j denotes a particular bin within distribution i. The quantities μ_{ij} and n_{ij} are, respectively, the number of events *expected* and *observed* in bin j of distribution i. The actual fit procedure utilizes the software package MINUIT [33] to numerically find the parameter values which minimize $-\ln\lambda$, where λ is the likelihood ratio $\mathcal{L}(\mu; n)/\mathcal{L}(n; n)$. The quantity λ is a general

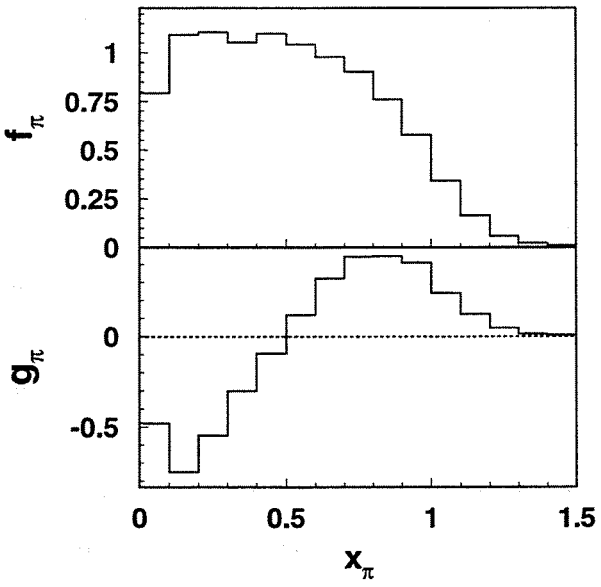

Figure 4.1: The f and g kinematic functions for $\tau^- \to \pi^- \nu_\tau$ decays. Selection inefficiencies, background from misidentified τ decays, and energy resolution effects are included.

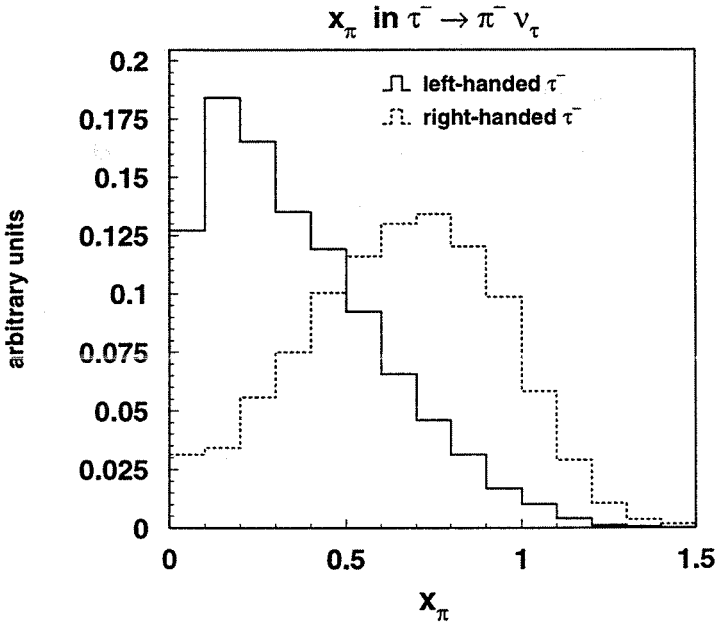

Figure 4.2: The x_π distributions for left-handed and right-handed τ in $\tau^- \to \pi^- \nu_\tau$. Selection inefficiencies, background from misidentified τ decays, and energy resolution effects are included.

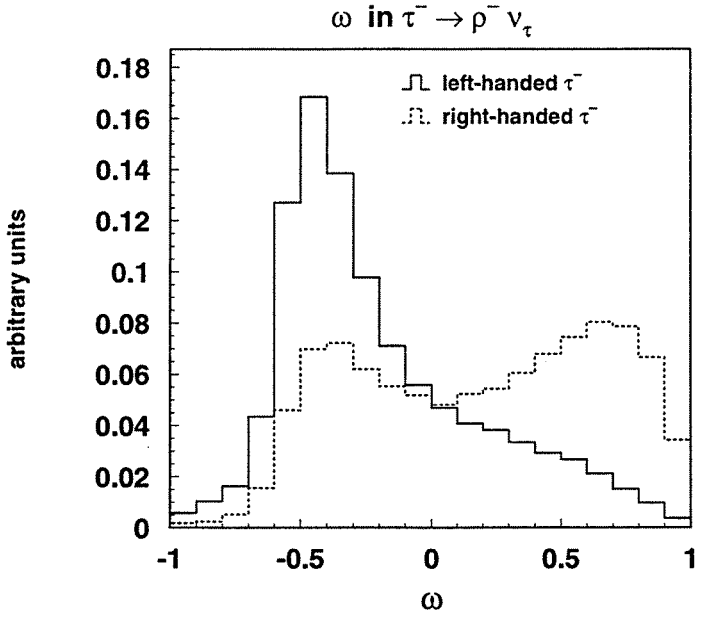

Figure 4.3: The ω distributions for left-handed and right-handed τ in $\tau^- \to \rho^- \nu_\tau$. Selection inefficiencies, background from misidentified τ decays, and energy resolution effects are included.

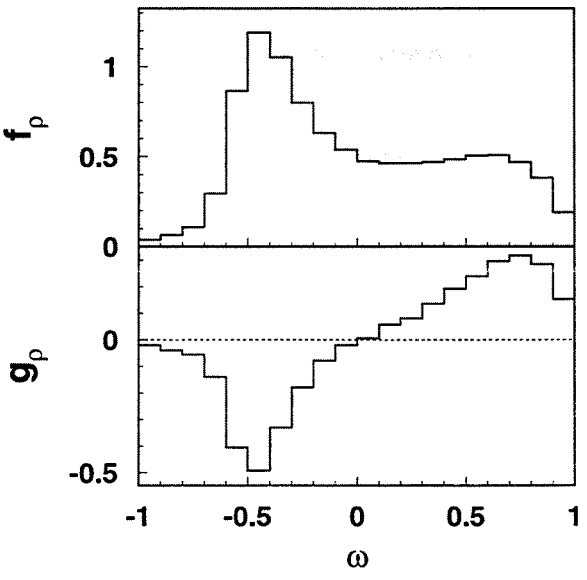

Figure 4.4: The f and g kinematic functions for $\tau^- \to \rho^- \nu_\tau$ decays. Selection inefficiencies, background from misidentified τ decays, and energy resolution effects are included.

χ^2 statistic when can be employed for goodness-of-fit evaluation [34].

The expected number of events in each bin is calculated from the decay distributions given in Equations 3.19 and 3.28 using the modified f and g functions which include the backgrounds, selection efficiencies and experimental resolutions. The functional form of the 1-dimensional ρX and πX decay spectra is

$$\frac{dN}{dz} = N_0 \left[f_h(z) + \mathcal{P}_\tau \xi_h \, g_h(z) \right] , \tag{4.2}$$

and the 2-dimensional correlated decay spectra for the $\rho\rho$, $\pi\pi$ and $\rho\pi$ classes has the form:

$$\frac{d^2N}{dz_1 \, dz_2} = N_0 \Big[f_{h_1}(z_1) f_{h_2}(z_2) + \xi_h^2 \, g_{h_1}(z_1) g_{h_2}(z_2) \tag{4.3}$$

$$- \mathcal{P}_\tau \, \xi_h \left(f_{h_1}(z_1) g_{h_2}(z_2) + f_{h_2}(z_2) g_{h_1}(z_1) \right) \Big] , \tag{4.4}$$

The variable z represents x_π or ω depending on the τ decay mode. N_0 denotes the normalization of a distribution; it can be fixed to the number of events in the observed data distribution or left as a floating parameter in the fit.

This measurement method was tested by fitting decay distributions based on a sample of Monte-Carlo $e^+e^- \rightarrow Z \rightarrow \tau^+\tau^-$ events. The Monte-Carlo sample contains approximately eight times more events than the data sample. The raw decay distributions were scaled down by a factor of 8 to mimic the data distributions. New decay distributions were obtained from the (unscaled) raw distributions by employing a random number generator. New contents for each bin were generated according to a Poisson distribution with a mean equal to the bin's original raw contents. Obtaining the new distributions in this fashion is called *smearing* the raw distributions. The *scaled raw* decay distributions were then fit using f and g functions constructed from the *smeared* distributions. This smearing and fitting procedure was repeated 1000 times to study the distribution of the best-fit values of ξ_h and $\mathcal{P}_\tau$. The resulting average values are

$$\xi_h = -0.992 \qquad \text{and} \qquad \mathcal{P}_\tau = -0.135, \tag{4.5}$$

assuming universality in τ decays, and

$$\xi_\rho = -0.994 \, , \qquad \xi_\pi = -0.991 \qquad \text{and} \qquad \mathcal{P}_\tau = -0.135, \tag{4.6}$$

not assuming universality. These values should be compared to the input values of -1 for the chirality parameters and $\mathcal{P}_\tau = -0.134$. Good agreement is seen for $\mathcal{P}_\tau$, but the method

yields slightly biased results for the chirality parameters. The bias stems from the non-zero input $\mathcal{P}_\tau$ value which causes more left-handed than right-handed τ's to be generated. Consequently, the statistical fluctuations in right-handed τ decay distributions are relatively larger than those in the left-handed sample. The bias vanishes for Monte-Carlo samples that have no net τ polarization or that approach infinite size. This bias will be taken into account in the final result.

CHAPTER 5

THE LEP COLLIDER

In the late 1970's, the European high energy physics community decided to construct a high energy electron-positron collider in order to study the physics of electroweak unification. This machine was dubbed LEP - for Large Electron-Positron collider. At that time, the electroweak gauge bosons W^+, W^- and Z had not yet been discovered, but measurements of the electroweak mixing angle $\sin^2\theta_w \approx 0.2$ predicted $M_W \approx 80$ GeV and $M_Z \approx 90$ GeV. LEP design studies were initiated in 1976, and the first practical design was completed in 1978 [35]. The final design of LEP [36,37] evolved from a 1979 report which embodied a two stage plan for a 30 km circumference machine with a maximum beam energy of ≈ 100 GeV. The initial stage proposed a beam of energy of ≈ 50 GeV in order to produce copious numbers of Z bosons at $\sqrt{s} \approx M_Z$. The second stage called for additional accelerating cavities, hopefully superconducting, to boost the beam energy to ≈ 100 GeV in order to observe the production of W^+W^- pairs. The first phase of LEP operation with collision energies near the Z boson mass is called LEP 1, while the second phase with center-of-mass energies above W^+W^- production threshold is named LEP 2.

Today, the LEP collider at CERN is the world's largest particle accelerator. It resides within a 26.667 km circumference tunnel 3.8 m in diameter as much as 150 m underground between the Geneva, Switzerland airport and the Jura mountain range in France (Figure 5.1). Construction of the main LEP tunnel, secondary tunnels, experimental caverns and associated surface buildings required 6 years (1983-1988) at a cost of 5 billion French francs.

LEP is not perfectly circular. Instead, it consists of 8 arcs, each 2840 m in length, interconnected by 8 straight sections, each 500 m long. The arcs contain the beam optics which steer the beams through these bending sections. Conventional (non-superconducting)

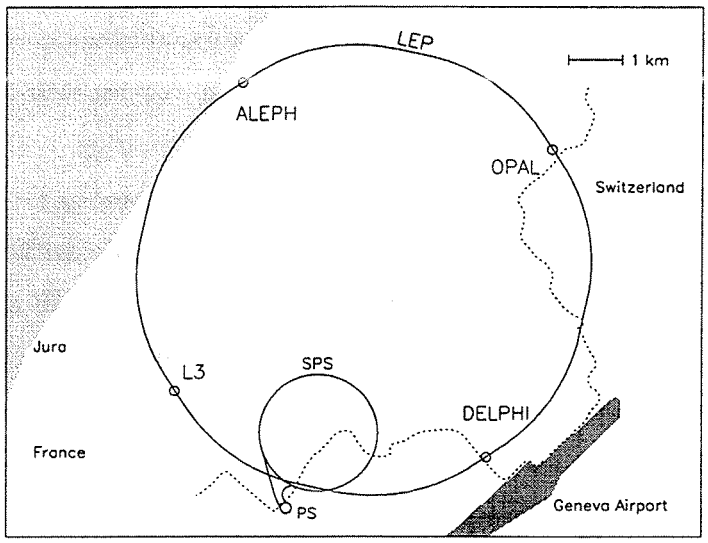

Figure 5.1: Location of the LEP e^+e^- collider at CERN.

dipole magnets composed of concrete and steel layers provide the bending field. Quadrupole magnets of alternating polarity (the strong focusing scheme) focus the beams to maintain tolerable transverse beam size. Sextupole magnets compensate for *chromaticity*, which is the dependence of focusing strength on energy. In total, the 8 LEP bending arcs contain 3368 dipoles, 816 quadrupoles, 504 sextupoles, and 700 horizontal and vertical orbit correctors.

The four experiments (L3, ALEPH, OPAL and DELPHI) are housed in the centers of four straight sections. Superconducting quadrupole magnets located on both sides of each experiment squeeze the beams to small transverse dimensions in order to increase luminosity at the intersection points (IPs). At the IPs, the beams have dimensions ≈ 10 μm in the vertical plane and typically 150 μm in the horizontal plane. Special quadrupole magnets rotated 45° around the central axis compensate for the horizontal-vertical beam oscillation coupling introduced by the experiments' solenoid magnets.

The LEP tunnel houses a single beampipe within which the e^+ and e^- beams circulate in opposite directions. Most of the beampipe is made from aluminum surrounded by several millimeters of lead. The lead reduces the amount of synchrotron radiation escaping the beampipe, because the radiation could damage nearby equipment. At each of the IPs, the beampipe is made from beryllium to minimize scattering of outgoing particles.

Beam particles scattering off air molecules in the beampipe can greatly reduce the useful beam lifetime. Hence, the beampipe is part of an elaborate vacuum system which

creates and maintains low gas pressure within the beampipe. The LEP pumping system reduces the pressure to 8×10^{-12} Torr. Synchrotron radiation from circulating beams causes the pressure to rise to $\approx 10^{-9}$ Torr by provoking gas molecules to desorb from the inner wall of the beampipe.

The 352 MHz radiofrequency (RF) accelerating system for LEP 1 consists of 128 copper cavities powered by sixteen 1 MW klystrons. These RF cavities are located in the straight sections surrounding the L3 and OPAL detectors. The RF system provides the energy needed to accelerate the e^+ and e^- beams from injection energy to physics energy, as well as resupplying the energy lost from the beams by synchrotron radiation. During the 1995 run, several new superconducting RF cavities were installed in preparation for the LEP 2 high energy running.

LEP is actually the last in a chain of five accelerators. The other four machines comprise the LEP injector system. Figure 5.2 illustrates the scheme used to accumulate, accelerate and inject electron and positron bunches into LEP. The LEP Injector Linacs (LIL) and the Electron-Positron Accumulator (EPA) were new machines constructed solely for LEP operation. In order to reduce cost and save time, CERN wisely and efficiently incorporated two existing accelerators, the Proton Synchrotron (PS) and Super Proton Synchrotron (SPS), into the LEP injection system. The filling of the LEP ring does not interfere with the usual operations of the PS and SPS as proton synchrotrons.

The electrons and positrons used in LEP are produced cyclically in the LIL. To create positrons, electrons from a electron gun are accelerated to 200 MeV in the first linac. These electrons bombard a tungsten target, producing hard photons which then convert into electron-positron pairs. A nearby magnet bends the positrons into the second linac, which accelerates them to 600 MeV. Electrons destined for LEP are fired from a separate electron gun directly into the 600 MeV linac.

Following the LIL, the 600 MeV e^+ and e^- are transferred to the EPA. The EPA temporarily stores the electrons and positrons produced in the LIL until a satisfactorily large current is accumulated. Typically, 2.5×10^{10} e^+ and 1.3×10^{10} e^- are accumulated before injection into the PS. More positrons are needed because the positron injection efficiency is lower.

After leaving the EPA, the electron and positron bunches enter the PS where they are accelerated to 3.5 GeV before injection into the SPS. In the SPS, the bunches are accelerated to the LEP injection energy. Through 1994, the LEP injection energy was 20

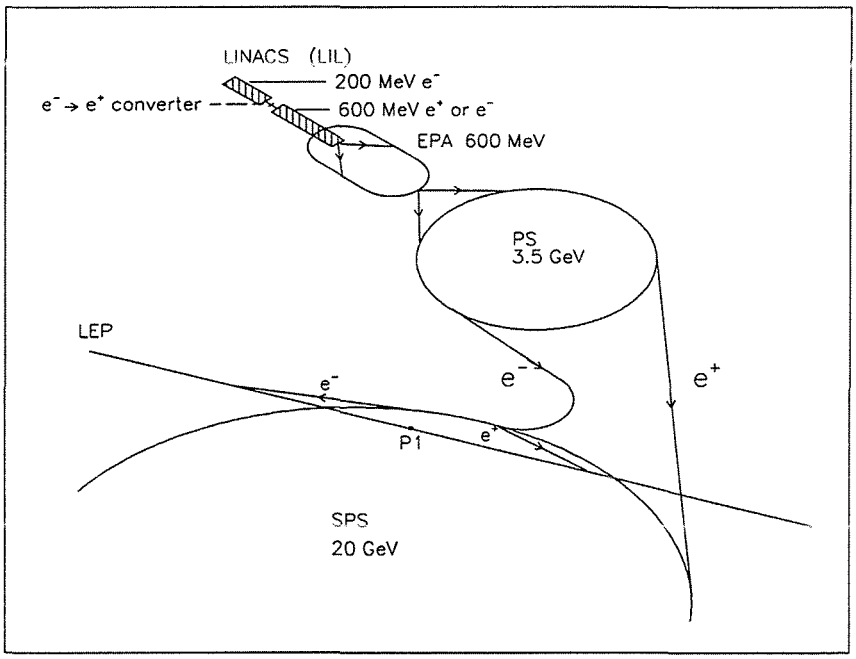

Figure 5.2: Accelerators in the LEP injector system.

GeV. In 1995, this energy was raised to 22 GeV to improve injection efficiency.

Throughout the years, there have been several bunching schemes in LEP. Until 1994, the e^+ and e^- beams consisted of 4 bunches equally spaced in time by ≈ 22 μs. In 1994, each beam contained 8 equally spaced bunches. In 1995, the "bunch train" mode was initiated in preparation for LEP 2 operation. In this mode, the e^+ and e^- beams consisted of 4 equally spaced "trains" containing up to 4 closely spaced "bunchlets".

Once LEP has been filled, the beams are accelerated to physics energy. Then, the superconducting quadrupoles around each experiment squeeze the beam to increase luminosity. After the beams are brought into collision, the machine operators adjust the beam orbits to attain maximum luminosity while minimizing beam-related backgrounds in the detectors. The average LEP luminosity has improved each year, such that in 1994, the typical LEP luminosity in each detector at the start of a fill was $\mathcal{L} \approx 1.5 \times 10^{31}$ cm^{-2} s^{-1}. This luminosity corresponds to approximately one $Z \rightarrow q\bar{q}$ decay produced every 2 s at $\sqrt{s} = M_Z$. Figure 5.3 illustrates the amount of data collected by L3 during each year of LEP 1. The relative steepness of the curves gives an indication of how the machine performance improved over time. A typical LEP fill would last approximately 10 hours, resulting in an average integrated luminosity of 300-500 nb^{-1} per fill, corresponding to

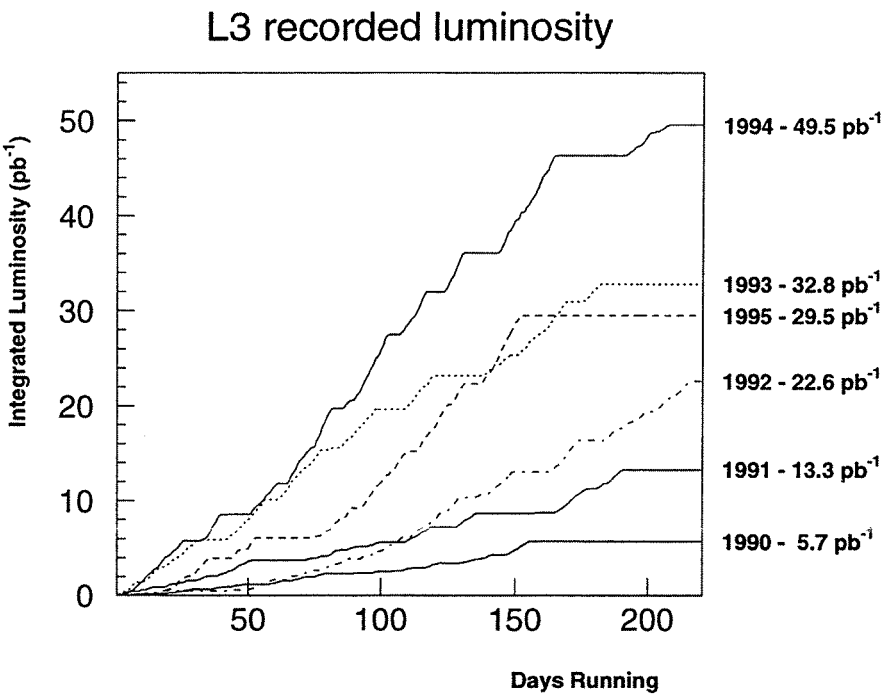

Figure 5.3: Integrated luminosity recorded by L3 versus time during the LEP 1 running periods.

9000-15000 $Z \rightarrow q\bar{q}$ events.

The LEP 1 program was successfully completed in 1995. Each of the four LEP experiments recorded roughly 4 million Z decays. These samples constitute the bulk of the world's Z boson data collected up to the present.

CHAPTER 6

THE L3 DETECTOR

The L3 experiment, depicted in Figure 6.1, is a general purpose detector for studying e^+e^- collisions at center-of-mass energies up to 200 GeV. The design underscores the goal to make high resolution energy measurements of electrons, muons, photons, and hadronic jets. Briefly, from the outermost part of the detector inwards, the L3 detector consists of: a 12 m diameter solenoid magnet providing a 0.5 T field parallel to the beam axis; a large volume muon spectrometer consisting of three precise drift chamber layers ; a uranium-proportional chamber sampling hadron calorimeter; an electromagnetic calorimeter composed of BGO crystals; a charged particle tracking chamber; a silicon microstrip detector.

In this chapter, descriptions of various detector components are presented. Detailed reports on the detector construction and subdetector design are available in References [38], [39] and [40].

In the L3 coordinate system, the $x-y$ $(r-\varphi)$ plane is perpendicular to the beam direction. The positive x-axis points to the center of the LEP ring, the positive y-axis points vertically upward, and the positive z-axis points along the e^- beam direction.

6.1 Magnet

The most prominent feature of the L3 detector is the large octagonal solenoid magnet surrounding the subdetectors. A 12 m long aluminum coil carries 30 kA of current to provide a 0.5 T magnetic field parallel to the beam axis in the central volume. Hence, the magnetic field bends a charged particle's trajectory in the $x-y$ plane. An iron yoke surrounding the coil acts as a magnetic flux return. Table 6.1 lists the main parameters of the solenoid.

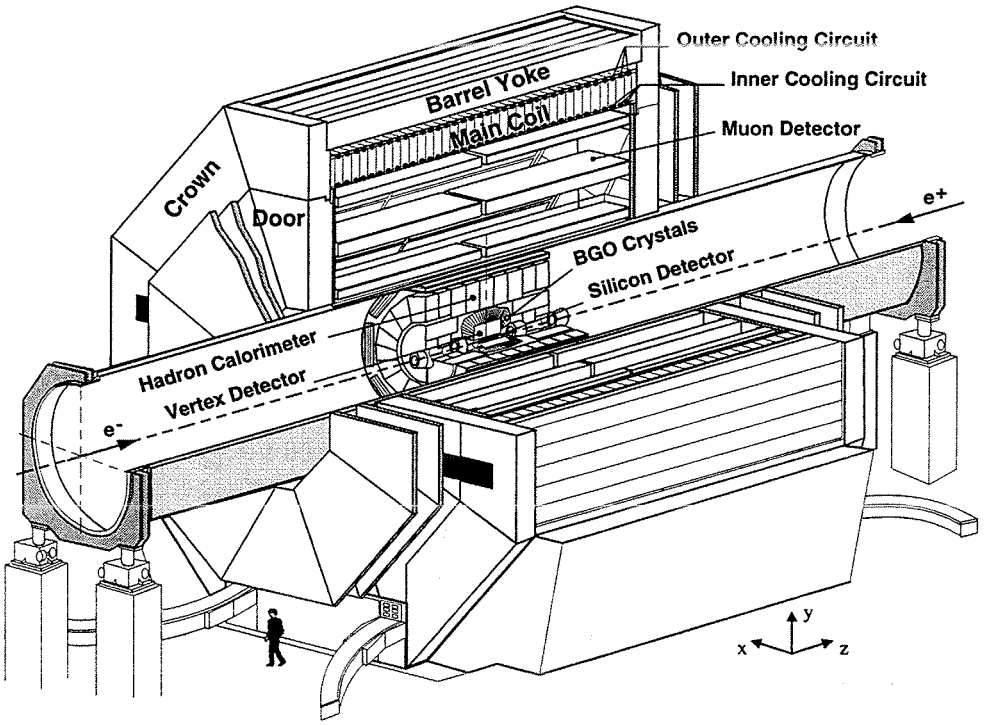

Figure 6.1: Perspective view of the L3 detector.

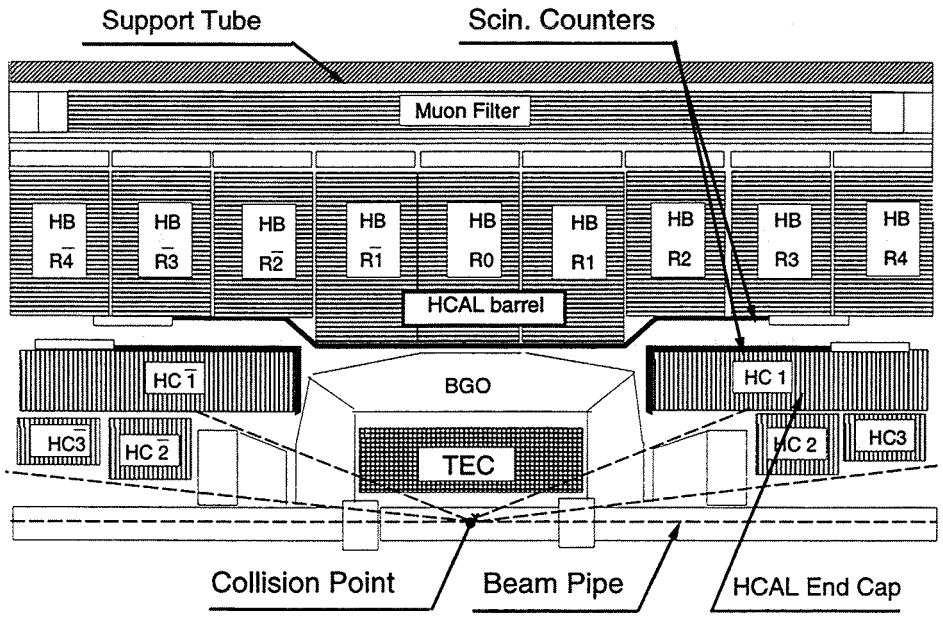

Figure 6.2: View of the inner L3 subdetectors in the upper $r - z$ plane.

Inside radius of coil	5930 mm
Width of Al conductor	890 mm
Outside radius of yoke	7900 mm
Total length of coil	11900 mm
Rated current	30 kA
Current density in conductor	55 A/cm^2
Electrical power at taps	4.2 MW
Central field	0.5 T
Stored magnetic energy	150 MJ
Coil weight	1100 t
Shielding weight	6700 t
Cooling water flow	150 m^3/h

Table 6.1: Main parameters of the L3 solenoid.

The solenoid coil is 168 turns long and consists of aluminum plates which were welded together at CERN. Each plate is 1/8 of a turn. During construction, four plates were welded to form a half-turn. Then, twelve half-turns were welded to create a 6-turn package weighing 38 t. Each package is also bolted together with insulated bolts to maintain structural rigidity. Twenty-eight 6-turn packages form the complete coil.

The coil is cooled by water which flows through two independent circuits welded to the inner and outer edges of the coil. In order to allow thermal expansion of the coil, each package rests on bronze skates which can move on two rails attached to the lower part of the yoke. One coil end is secured to a pole, while the other end is attached to its pole via air core springs. To minimize heat transfer to the inner subdetectors, the interturn gaps are filled with rubber and a thermal screen is situated along the inside of the coil.

The barrel yoke and two poles surrounding the coil provide a return for the magnetic flux lines. The magnetic structure consists of 5600 t of soft iron supported by and contained within the two poles. Each 1100 t pole is a self-supporting steel structure consisting of the crown and two hinged doors allowing access to the muon chambers. The crown forms a complete octagonal ring, while the two doors are half-octagons. Each 340 t door rests on grease skates and rotates about large hinges mounted in the crown.

Obtaining an accurate field map in such a large volume is not an easy task. The

field within the support tube was mapped with a series of Hall probes. Approximately 1000 magnetoresistors attached to the muon chambers map the field in the space between the support tube and the coil. Five NMR probes continuously monitor the absolute value of the field.

6.2 Support Tube

Although the L3 support tube (ST) is not an active detector element, it is an important component of the experiment. The ST bears the heavy load of all the subdetector systems. The support mechanisms for the muon chambers are attached to the outside of the ST, while the remaining subdetectors are mounted within the ST. Furthermore, the LEP optics surrounding the L3 IP are mechanically coupled to the ST.

The ST is a 32 m long, 50 mm thick steel tube with an outer diameter of 4.45 m. The central portion of the ST located within the solenoid magnet volume is constructed from nonmagnetic stainless steel, while the rest is carbon steel. Active servo jacks supporting the ends of the ST keep it and the attached components aligned to the nominal LEP beam line position. With all detector elements installed, the ST sags approximately 10 mm.

6.3 Muon Spectrometer

The purpose of the muon spectrometer system is to measure the momenta of muons. Most muons penetrate the calorimeters with minimal energy loss and traverse the spectrometer drift chamber layers. Coordinates from the drift chamber hits are used to reconstruct the muon's trajectory and measure the momentum via the deflection caused by the magnetic field.

The L3 muon spectrometer is divided into two subsystems covering different polar angle regions. The barrel chambers span the central region $36° < \theta < 144°$. The two sections of the forward/backward (FB) chambers extend over regions closer to the beam axis: $24° < \theta < 44°$ (forward) and $136° < \theta < 156°$ (backward). The complete system has a geometrical acceptance of 92% of 4π.

The barrel muon chamber system is a modular structure occupying the large 1000 m^3 volume between the support tube and the magnet coil. Figure 6.3 provides a perspective

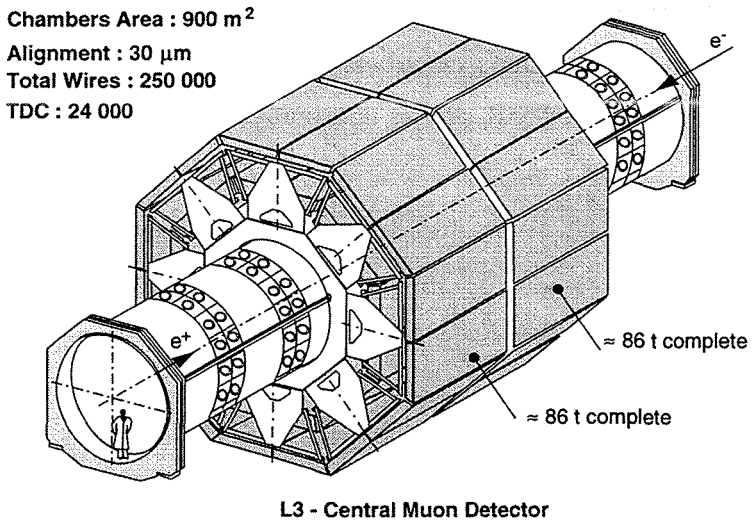

Figure 6.3: Perspective view of the L3 barrel muon chamber system.

view of the barrel spectrometer. In the $x-y$ plane, the barrel spectrometer has an octagonal shape matching the geometry of the magnet coil. Each octant is an independent mechanical unit supporting three drift chamber layers 5.6 m in length (z direction). Octants are mounted onto a cylindrical shell, called a torque tube, to form a so-called ferris wheel. The torque tube rolls on rails attached to the support tube. Two ferris wheels, one each for the $+z$ and $-z$ sides, form the barrel spectrometer structure.

Figure 6.4 is a schematic of an octant in the $x-y$ plane. All three layers, denoted MI, MM and MO, have so-called "P" chambers which provide precise track coordinates in the $r-\varphi$ (bending) plane. The "Z" chambers, which form the top and bottom covers of the MI and MO P chambers, measure the z coordinate. A single P chamber comprises the MI layer, but two P chambers span the MM and MO layers. Hence, there are five P chambers and six Z chambers per octant.

The P chamber $r-\varphi$ measurements are used to determine the sagitta, s, as illustrated in Figure 6.5. When the muon radius of curvature is large compared to the lever arm, L, the transverse momentum with respect to the magnetic field is inversely proportional to the sagitta: $p_T \propto BL^2/s$. With a 0.5 T magnetic field and a 2.9 m lever arm, a $p_T = 45$ GeV/c muon has a sagitta of 3.6 mm. The momentum resolution $\sigma_p/p \propto \sigma_s\, p/BL^2$ improves linearly with the sagitta accuracy and quadratically as the lever arm increases. This quadratic dependence motivates the spectrometer's large lever arm. To achieve a momentum resolution of $\sigma_p/p = 2.5\%$ at 45 GeV/c requires a sagitta resolution of ≈ 85 μm.

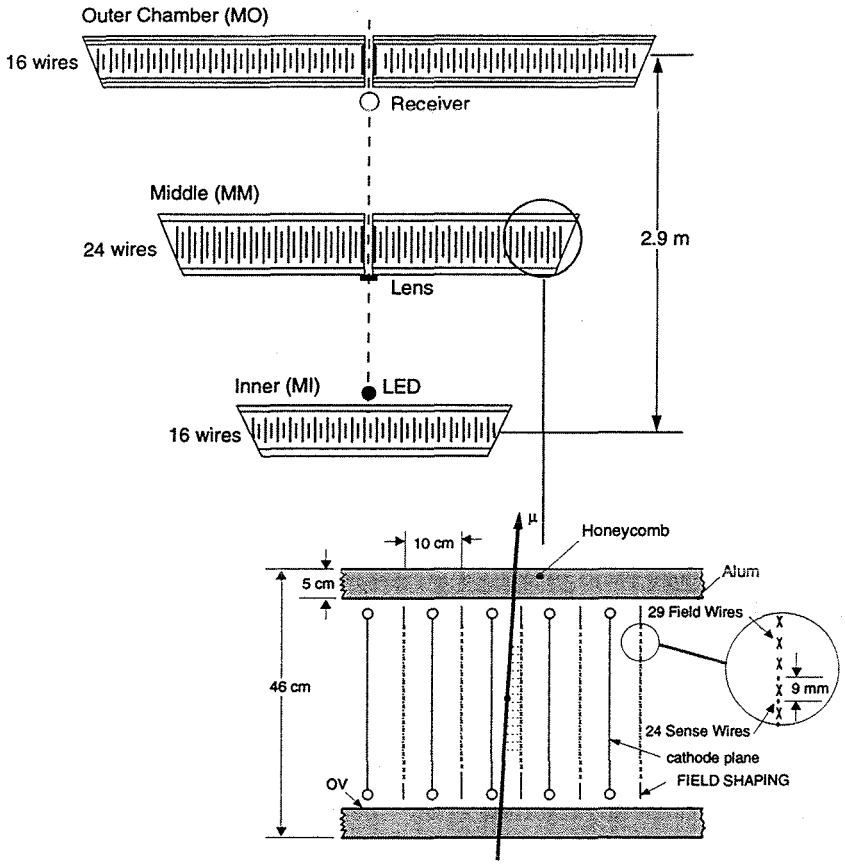

Figure 6.4: Schematic of barrel muon spectrometer octant in the $x-y$ plane. The inset illustrates the wire plane structure of an MM chamber.

Figures 6.4 and 6.6 illustrate the P chamber wire plane geometry. As a passing muon ionizes drift gas molecules, the liberated electrons drift toward the anode plane, while the cathode plane attracts the ions. The cathode and anode planes are spaced 50.75 mm apart. The 30 μm diameter gold-plated tungsten cathode wires are spaced 2.25 mm apart. In the anode plane, the 30 μm diameter signal wires are separated by 9 mm and interspersed with the field-shaping wires held at a slightly lower potential. The MI and MO anode planes contain 16 signal wires, whereas the MM P chambers have 24 signal wires per anode plane. The guard wires, located on both ends of the anode plane, equalize the drift time behavior of the sense wires.

The desired sagitta resolution places strict tolerances on wire placement and chamber alignment. The signal and field shaping wires are positioned to 40(10) μm accuracy in the bending (non-bending) plane by using precision glass/carbon fiber bridges. An internal LED-based alignment system helps position the bridges to within 10 μm. The chambers

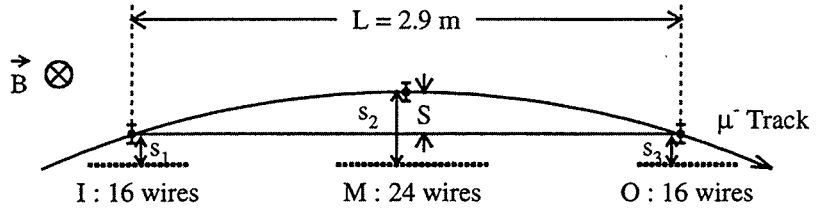

Figure 6.5: The track curvature is determined by the sagitta S. Hits in the P-chamber layers provide the distances $s1$, $s2$, and $s3$.

within an octant must also be aligned to one another since muons with $p_T > 3$ GeV/c are confined to a single octant. The octant stands themselves are designed to maintain chamber alignment to better than 30 μm. LED-based and laser-based alignment systems monitor the straightness and twisting of the octant ends. Any misalignment is taken into account during track reconstruction.

The P chambers are filled with 61.5% argon / 38.5% ethane mixture at 740 mm Hg. At nominal voltage settings, the gas amplification is 5×10^4. In the drift region, the electric field of 1140 V/cm and the 0.5 T magnetic field causes an 18.8° Lorentz drift angle. The single wire resolution has been measured to be $\approx$ 220 μm averaged over the drift cells. The corresponding sagitta resolution is 60 μm.

The 96 Z chambers cover the top and bottom faces of the P chambers in the MI and MO layers. Each chamber consists of two layers of drift cells between parallel rows of aluminum I-beams. The drift cell layers are offset by one half cell to resolve left-right ambiguities. A 50 μm diameter gold-plated molybdenum anode wire held at +2.15 kV spans the length of each cell. The I-beams, connected to −2.4 kV, serve as the cathodes. The cell layers are closed by an aluminum sheet held at ground and electrically isolated from the I-beams by fiberglass strips. The average drift velocity of the 91.5% argon / 8.5% methane gas mixture is about 30 μm/ns. The average single wire resolution is measured to be 500 μm.

Reconstructing muon tracks requires a measurement of the drift time from hit wires. Signals from the P and Z chamber wires are amplified and then passed through a discriminator. The discriminator outputs are connected to Time-to-Digital Converters (TDCs) which record the arrival time of the signals over threshold. A timing calibration system

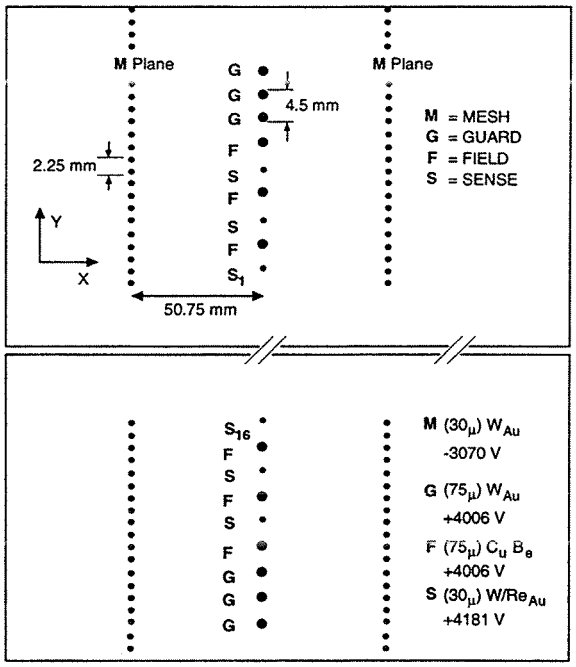

Figure 6.6: Wire plane geometry of a P chamber drift cell in the $x-y$ plane. The mesh (M) plane is the cathode, while the guard, field, and sense wires comprise the anode plane.

monitors the stability of each channel by injecting a pulse at the amplifier and recording the propagation time through the readout electronics.

Construction of the FB muon system was motivated by the physics opportunities in the LEP 2 program. One half of the system was installed in 1994 and the other in 1995. The barrel muon chambers alone provide momentum measurements in 81% of the 4π solid angle; the FB chambers, spanning the regions $24° < \theta < 44°$ from the beam axis, increase the solid angle acceptance of the muon spectrometer to 92%. In the polar angle regions covered by only two barrel chamber layers, the inner FB chamber layer improves momentum resolution by providing a third coordinate measurement.

Three planes of FB chambers are mounted on the four solenoid magnet doors. Coils wrapped around the doors provide an average 1.2 T toroidal magnetic field within the doors. One plane of chambers is attached inside of the doors, and the other two chamber planes are located on the outer sides. The chambers are shaped such that pairs of chambers match the octant structure of the magnet doors. Each chamber plane contains three layers and measures two coordinate projections independently. One layer provides a θ (radius)

measurement, while the other two layers, offset from one another by one half cell, provide azimuth coordinates with resolved ambiguities. The chamber design is based on an I-beam drift cell structure similar to the barrel Z-chambers. However, the FB chambers have 4 anode wires per cell, as well as field shaping strips. Four anode wires can provide a track segment with a measured slope. All drift cells are 105 mm wide and each chamber plane package is only 18 cm thick.

The FB muon chamber readout differs slightly from the barrel system. After amplification and discrimination, the signals are multiplexed to reduce the number of necessary TDC channels by a factor of 8. A timing calibration system monitors the signal propagation time stability for each wire in the FB chambers. This propagation delay is subtracted from the TDC measurement to determine the drift time.

The single wire resolutions averaged over the drift cell are measured to be $\approx 270\ \mu$m ($350\ \mu$m) for the azimuth (radius) measuring layers. The momentum resolution at 45 GeV/c varies from 5% to 20% in the region $0.81 > |\cos\theta| > 0.72$. In the region $25° < \theta < 30°$, the momentum resolution is limited to no better than 30% due to multiple scattering in the 0.9 m thick steel door.

6.4 Hadron Calorimeter

The hadron calorimeter (HCAL), together with the BGO calorimeter in front of it, measures the energy of single hadrons and jets emerging from e^+e^- collisions. The HCAL also acts as a filter by allowing only non-showering particles to reach the muon chambers. Muons can be identified in the HCAL by their characteristic minimum-ionizing particle (MIP) energy deposition.

The HCAL is a sampling calorimeter consisting of multiple layers of depleted uranium absorber plates and proportional wire chambers. Uranium was chosen as the absorber material because its short absorption length allowed the most compact calorimeter design. Uranium's natural radioactivity presents technical challenges for construction and operation, but the radioactivity also provides a convenient *in situ* calibration of the wire chambers. Gas wire proportional chambers were chosen as the detecting medium as a result of their stability, long-term reliability, ability to operate in a magnetic field, and ease of mass production. The HCAL system constitutes the bulk of the absorbing material in L3. Including the BGO and support tube, the detector is at least 5.9 nuclear absorption lengths

thick down to $\theta = 12°$ from the beam line.

The HCAL is divided into a barrel and two endcap parts, as illustrated in Figures 6.1 and 6.2. The cylindrical barrel spans the polar angle range $25° < \theta < 155°$ over the full azimuthal range. The two endcaps cover the polar angle ranges $5.5° < \theta < 35°$ and $145° < \theta < 174.5°$.

The 261 ton HCAL barrel has a modular structure consisting of 9 rings of 16 tower-like modules. Each ring covers the complete azimuthal range $0 < \varphi < 2\pi$. The three central rings are composed of "long modules" which contain 60 planes of wire chambers and 58 layers of uranium plates. The "short modules" of the 6 outer rings hold 53 wire chamber planes and 51 uranium plates. Figure 6.7 illustrates the wire chamber layers for a long module. The HCAL barrel is 472.5 cm long and has an outer radius of 179.5 cm. The inner radius of the long and short modules are 88.5 cm and 97.9 cm, respectively.

The uranium plates and wire chamber layers are stacked within a stainless steel support structure. The 5 mm thick uranium absorber plates are plated with 20 μm of Cu-Ni alloy for safety reasons. Each wire chamber layer is a plane of 0.3 mm brass rectangular tubes with inner dimensions of 5 mm $\times$ 10 mm. For structural rigidity, 0.7 mm thick brass plates are attached to both sides of the chamber plane by self-adhesive Mylar sheets. The brass plates also shield the chambers from uranium radioactivity, and the Mylar sheets electrically insulate the tubes. Each tube contains a gold-plated tungsten anode wire 50 μm in diameter held at ground potential. The tube itself acts as the cathode at a potential of -1600 V. The chambers are filled with a 80% Ar/20% CO_2 gas mixture at atmospheric pressure to provide a nominal gain of 10^4.

The wires in alternating chamber layers are oriented at right angles to each other. The anode wires in the φ layers are parallel to the beam direction, whereas the z layer anode wires are perpendicular to the beam. The wires from each projection are grouped into "readout towers". The anode wires in each tower are connected in parallel and are input to an ADC. The long (short) modules are segmented into 10 (8) radial layers each with 9 φ and 9 z towers of uniform size, as shown in Figure 6.7. Each tower nominally covers an angular region $\Delta\varphi = 2°, \Delta\theta = 2°$. The radial thickness of the towers is smaller toward the front (inner radius) of the module because shower densities are higher there. The HCAL barrel has over 23,000 readout channels.

The energy resolution for single pions, as in $\tau^- \to \pi^-\nu_\tau$ and $\tau^- \to \rho^-\nu_\tau$ decays, was measured in a test beam experiment. This resolution can be represented as

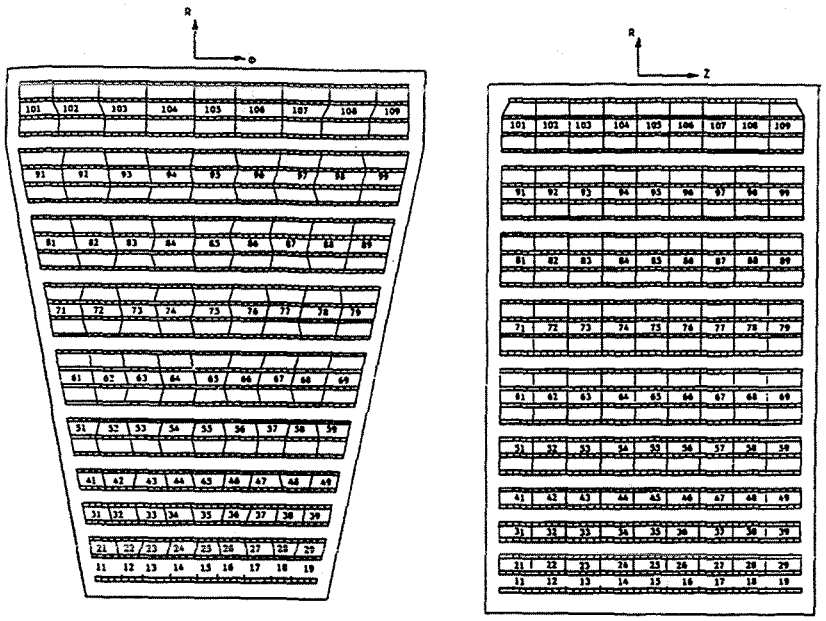

Figure 6.7: Wire chamber layers in a long HCAL barrel module. The φ and z layers are shown separately. The radial lines and numbers indicate the readout tower groups.

$\sigma(E)/E = 5\% + 55\%/\sqrt{E}$, where energy is given in GeV. The total energy resolution from hadronic Z decays is measured to be $\approx$ 10%, and the jet angular resolution is 35 mrad.

The two halves of the HCAL endcap system consist of three separate rings, labeled HC1, HC2 and HC3 in Figure 6.2. These rings are divided vertically into half-rings to give 12 distinct modules in the HCAL endcap. The modular structure of the endcaps facilitates access to the central L3 subdetectors. As in the HCAL barrel, each endcap module consists of alternating layers of uranium absorber plates and proportional wire tubes stacked in stainless steel containers. The face of the plates and chambers are perpendicular to the beam direction.

For mechanical rigidity, the endcap containers are segmented longitudinally into compartments separated by 16 mm stainless steel plates. The HC1 containers have 4 compartments, while HC2 and HC3 have 2 compartments each. The HC1 compartment closest to the interaction point contains 26 chamber layers and 5 mm thick uranium plates. The remaining three HC1 compartments house 17 chamber planes interleaved with 10 mm of uranium. Each HC1 half-ring holds 77 chamber layers in total. The 27 and 23 chamber layers in the HC2 and HC3 containers, respectively, are also separated by 10 mm of uranium. In order to limit radioactivity background in the BGO and TEC, steel plates replace the

first 15 mm of uranium absorber in the HC1 and HC2 containers.

The wire chamber layers in each half-ring are arranged in two alternating configurations. The "U" layers consist of four individual chambers each spanning $\Delta\varphi = 45°$. The wires are stretched azimuthally across each chamber to provide a θ measurement of the shower. The "V" layers have three full size ($\Delta\varphi = 45°$) and two half ($\Delta\varphi = 22.5°$) chambers such that the V-layer wires are rotated 22.5° with respect to the U-layer wires. This stereo angle between allows a φ measurement to be made.

To form the 3960 HCAL endcap readout towers, the detector is logically divided into 31 "roads" $\Delta\theta \approx 1°$ wide pointing toward the interaction point. Separate towers are formed for the U and V layers, so the resulting azimuthal segmentation is $\Delta\varphi = 22.5°$. Each half-ring is segmented longitudinally and the wires within each road are grouped together. HC1 has seven longitudinal segments, while HC2 and HC3 have three and two z segments respectively.

Between the HCAL barrel and support tube is another subdetector called the muon filter. The muon filter provides an additional 1.03 absorption lengths to the HCAL barrel and helps resolve ambiguities between the HCAL and the muon chambers. The eight octants of the muon filter consist of six 1 cm thick brass plates interleaved with 5 layers of proportional chambers followed by five 1.5 cm thick absorber plates approximately matching the circular shape of the surrounding support tube.

6.5 Scintillation Counters

The scintillation counters provide time-of-flight information for incident charged particles. This timing information helps discriminate cosmic ray muons passing through the detector from genuine $Z \rightarrow \mu^+\mu^-$ events. The scintillators are also used in a trigger for events with multiple charged particles, such as hadronic Z decays.

Like other L3 subdetectors, the scintillator system is divided into barrel and endcap parts. The scintillator panels are located between the electromagnetic and hadronic calorimeters, as depicted in Figure 6.2. The scintillator counters are constructed from 1 cm thick plastic scintillator optically coupled to a Plexiglas light guide. Photomultiplier tubes at the ends of the light guides collect the photons to create an analog pulse.

The 30 barrel counters are bent to follow the inner radius of the HCAL barrel modules (Figure 6.2). They are 167 mm wide along the three middle HCAL modules and

182 mm wide along the outer modules. The projected length of a barrel counter is 2.9 m. Pairs of counters are grouped together to cover each of 16 HCAL φ sectors, except for the two sectors near the electromagnetic calorimeter support rails. These 2 sectors are each spanned by a single, wider scintillation counter. Both ends of the barrel scintillator counters have 32 cm long light guides attached to phototubes. The barrel scintillator system covers 93% of the solid angle within the region $34° < \theta < 146°$.

The 32 endcap scintillators are mounted in front of the HC1 endcap HCAL modules. Each scintillator covers one of the 16 Φ sectors of HC1. The active scintillator panel (270 mm long, 180 mm (275 mm) wide on the inner (outer) radius edge) is oriented perpendicular to the beam direction just over 1 m from the interaction point. The light guide carries the light around a 90° bend to a phototube at the far end of the HCAL. The endcap scintillators extend coverage down to θ angles of 25° and 155°.

Photomultiplier tubes attached to the ends of the light guides convert the scintillator light into an electrical signal. These phototubes can operate in the magnetic field with good quantum efficiency (14% at $\lambda = 430$ nm) with a gain of 4×10^5. A TDC using the 92 phototube outputs as START signals provides the timing information. The TDC has 15 bit dynamic range and a resolution of 50 ps. An ADC integrates the phototube output pulse so that time slewing corrections can be applied.

For genuine $Z \rightarrow \mu^+\mu^-$ events originating at the interaction point, the muons pass through opposite scintillators with a time-of-flight difference of zero. However, when a cosmic ray muon fakes a $Z \rightarrow \mu^+\mu^-$ event, the time-of-flight difference is at least 5.8 ns. Figure 6.8 shows the time-of-flight difference for tracks in a sample of $Z \rightarrow \mu^+\mu^-$ events. The good resolution of < 0.5 ns allows an easy discrimination of background from cosmic ray muons.

6.6 Electromagnetic Calorimeter

The primary purpose of the electromagnetic calorimeter is to measure the energy and position of electrons and photons. These particles interact predominantly with atomic electrons in matter. Energy is measured destructively, as the incident particle interacts to create a cascade of photons and electron-positron pairs. The shower energy is an indirect measure of the incident particle's energy.

The L3 electromagnetic calorimeter consists of nearly 11000 bismuth germanate

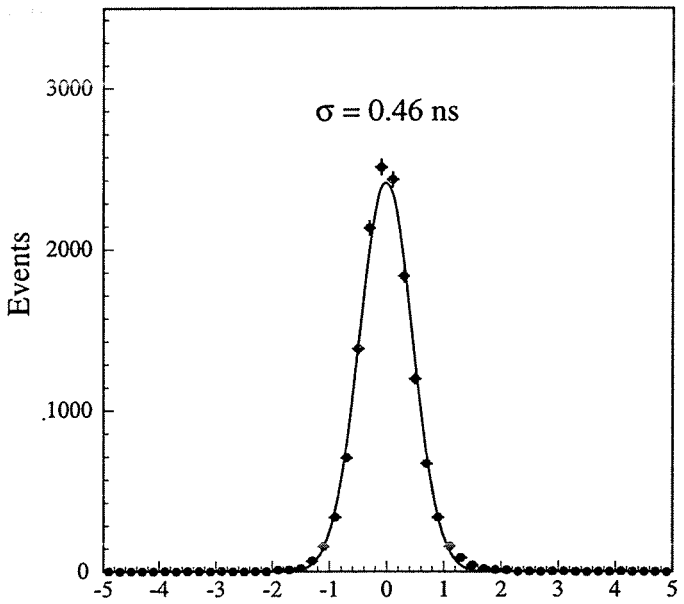

Figure 6.8: Corrected scintillator time-of-flight information for the two tracks in $Z \rightarrow \mu^+\mu^-$ events. A Gaussian fit indicates a resolution of 0.46 ns.

(BGO, $Bi_4Ge_3O_{12}$) crystals located between the tracking chambers and the hadron calorimeter modules. Table 6.2 lists several relevant properties of BGO. The short radiation length and long interaction length are particularly well-suited for this purpose. BGO serves as both the showering and detecting medium for electromagnetic showers. The shower cascade causes the BGO to scintillate, and photodiodes gather the scintillation photons which propagate through the crystal.

Density	7.13 g/cm^3
Radiation length	1.12 cm
Nuclear interaction length	22 cm
dE/dx	9 MeV/cm
Wavelength of maximum emission	480 nm
Refractive index	2.1
Temperature coefficient of light yield	-1.55 %/°C

Table 6.2: Physical properties of BGO.

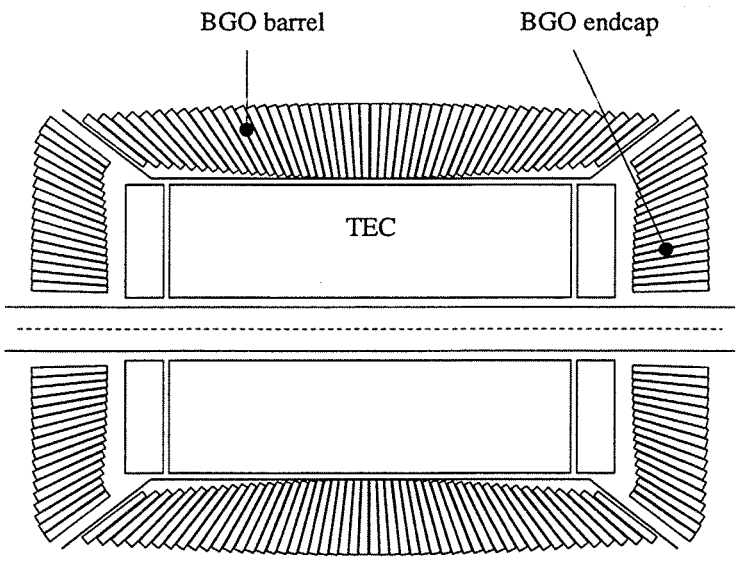

Figure 6.9: Side view of the BGO calorimeter.

The BGO calorimeter (Figure 6.9) consists of two half-barrels and two endcaps. The barrel contains 7680 crystals which span the polar angle region $11.6° < \theta < 38°$. The barrel has a cylindrical shape 100 cm long and an inner radius 52 cm from the beam axis. There are 48 crystals along the θ direction and 160 crystals around in φ. Each endcap unit has 1527 crystals and covers the regions $42° < \theta < 138°$ and $142° < \theta < 168.4°$. The front faces of the endcaps are situated at $z = \pm 75.6$ cm.

Each BGO crystal has the shape of a truncated pyramid, as illustrated in Figure 6.10. The crystals are 24 cm long with a square cross section. This length corresponds to 21.4 radiation lengths and 1.1 nuclear interaction lengths. The front and back face areas are 2×2 cm^2 and approximately 3×3 cm^2, respectively. The actual area of the back faces varies slightly depending upon the θ position of the crystal. The crystals point toward the interaction point and are tilted 10 mrad in φ to suppress leakage of scintillation photons. Each crystal is polished and painted with a high reflectivity paint to achieve a nearly uniform light collection efficiency.

The BGO calorimeter mechanical structures must support more than 10 tons of crystals, readout electronics, and associated monitoring systems. Moreover, the amount of dead space between crystals should be minimized, and the crystals themselves should not bear any weight in order to prevent cracking. The solution is a carbon fiber composite structure in which each crystal occupies a cell separated from its neighbors by 200 μm thick

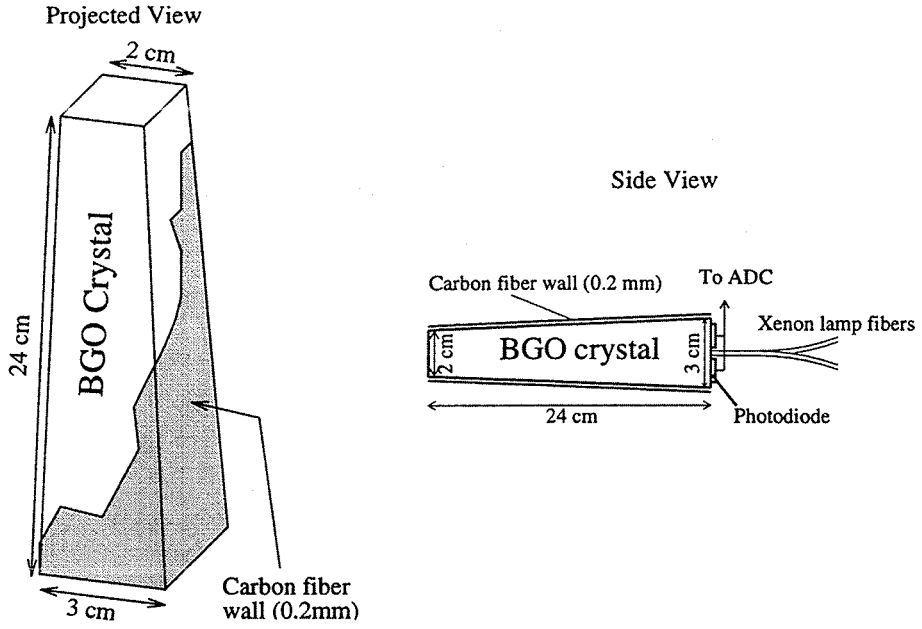

Figure 6.10: Schematics of a BGO crystal.

walls. A spring-loaded device holds each crystal in place. The cell walls and gaps form dead space accounting for 1.75% of the solid angle in the barrel region.

Two photodiodes mounted on the back of each crystal detect the BGO scintillation photons. These photodiodes have a quantum efficiency of nearly 70% and provide a signal of ≈ 0.2 fC (1200 electrons) per MeV of energy deposited in the BGO. The photodiode output is amplified and passed along to ADCs located 3 m away, outside of the hadron calorimeter. These ADCs provide at least 10 bit (0.1%) resolution for signals over an energy range from 100 MeV to 100 GeV. The linearity of the ADC response is better than 1% over the dynamic range. Typical electronic noise corresponds to approximately 1 MeV.

The relatively strong dependence of BGO light output on temperature necessitates keeping the crystal temperature constant to within a few tenths of a degree. Furthermore, since light output decreases as the temperature rises, the ambient temperature should be as low as possible, but above the dew point. Thin metal screens connected to a cooling fluid circuit remove heat from the amplifiers on the crystal backs to maintain the temperature to within $\pm 0.5°$C.

The energy resolution of the BGO calorimeter was tested at several energies before installation. This test beam study also provided initial calibration constants for the crystals. The measured energy resolution is $\approx 5\%$ at 100 MeV and better than 2% for energies above

2 GeV.

Calibration of the BGO *in situ* is performed by several methods. Light pulses from xenon flash lamps are used to monitor the BGO response. Optical fibers mounted on the crystals carry the light from the lamps to individual crystals. Electrons from $Z \rightarrow e^+e^-$ decays are used to monitor the BGO stability at high energies. The minimum ionizing signature from cosmic ray muons allow monitoring of stability at low energies.

6.7 Central Tracking Chambers

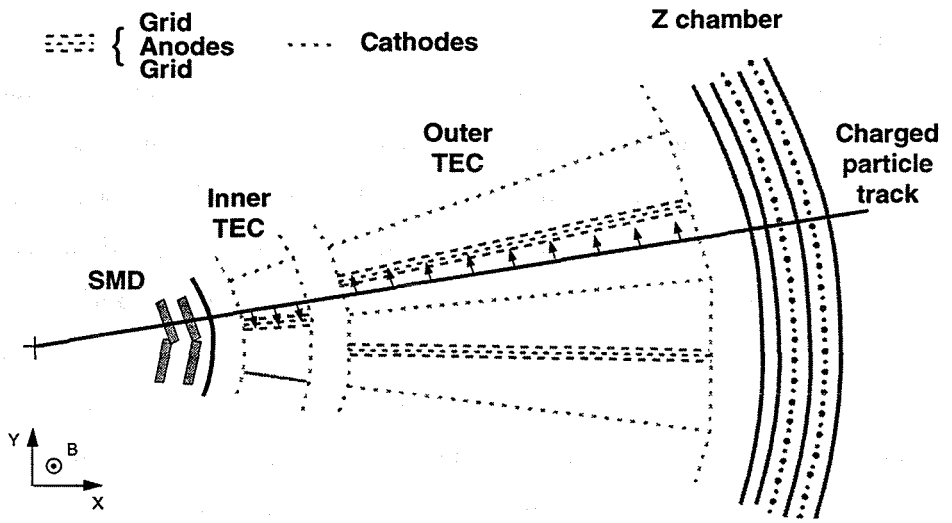

Figure 6.11: A partial schematic of the central tracking system in the $r-\varphi$ plane. The TEC and Z-chamber wires are strung perpendicular to the page.

The central tracking chambers provide position measurements of charged particles passing through the detector. From these coordinates, we can reconstruct the particles' trajectories and measure their momenta (transverse to the magnetic field) from the track curvature. Reconstructed tracks are also used to determine the impact points of charged particles on the electromagnetic calorimeter.

The central tracking chambers include two concentric, cylindrical drift chambers (the Time Expansion Chamber, TEC) surrounded by two proportional chambers (the Z-chambers). They occupy most of the volume between the beampipe and the BGO calorime-

ter. The TEC provides up to 62 $r - \varphi$ coordinates along a track, while the Z-chamber can provide 4 precise z coordinates per track. The available lever arm for measurements is 31.7 cm in the radial direction.

6.7.1 Time Expansion Chamber

The TEC consists of two concentric cylinders 982 mm long capped by aluminum plates at the two ends. The inner cylinder, 170 mm in diameter, is made from 1.5 mm thick beryllium. The outer cylinder has a diameter of 937 mm and is composed of 4 mm thick aluminum. The 45 mm thick aluminum end plates have been precisely drilled and machined to support the approximately 30,000 wires in the TEC. The gas inlets and outlets are also attached to the end plates.

The TEC is divided into 12 inner and 24 outer sectors. Cathode wire planes outline each sector, while the grid-anode plane-grid structures are situated radially along the sector centers. Figure 6.11 depicts one inner and two outer TEC sectors. The anode planes contain two types of sense wires. The *standard* wires, read out only at one end, provide precise $r - \varphi$ coordinates. The *charge division* (CD) wires are read out at both ends and can determine the z position of the track to within a few cm. For some standard wires in the outer sectors, five wires (called *pick-up* wires) from both neighboring grids are also read out. By comparing the charges induced on the pick-up wires, the left-right ambiguity for those standard anodes (LR wires) can be resolved. The inner sectors contain 6 standard and 2 CD anodes, while the outer anode planes include 31 standard, 14 LR and 9 CD wires.

After amplification and pulse shaping, each signal wire output is digitized by a Flash ADC. The nearly 2000 TEC readout channels produce 2 Mb of data per event. Special processors attached to pairs of Flash ADCs reduce this large body of data by 95% before transferring it to the L3 data acquisition (DAQ) system.

The TEC gas mixture and voltage settings are chosen to maximize the single wire resolution. Operating with an 80% CO_2/20% isobutane gas mixture at a pressure of 1.2 bar, the drift velocity in the low field region is 6 μm/ns. Using Flash ADCs to digitize the signal pulses allows a center-of-gravity method to be exploited for precisely measuring the drift time. The average wire resolution is 50 μm (60 μm) for the outer (inner) anode wires. The average transverse momentum resolution obtained with the TEC can be expressed as $\sigma(P_T) = 0.018(\mathrm{GeV}/c)^{-1} \times P_T^2$.

6.7.2 Z-chambers

Although the TEC charge division anodes provide track z coordinates, the resolution is limited to a only few cm. The Z-chambers offer z coordinate measurements with a much better resolution of 500 μm. The Z-chambers are two thin multiwire proportional chambers surrounding the TEC. Each chamber has one anode wire plane between two layers of cathode strips which are read out to make the position measurements. The Z-chambers cover the angular range $42° < \theta < 138°$.

As a charged particle passes through the Z-chambers, the electrons from the ionized gas drift toward the anode wires. The charge avalanche in the high field region near the anodes induces a nearly Gaussian charge distribution on the cathode strips. These copper strips are 3.8 mm wide separated by 0.65 mm. The four cathode layers, denoted u, v, w and z, are located at radii $r_u = 471$ mm, $r_v = 478$ mm, $r_w = 480$ mm, and $r_z = 487$ mm. The v and z layer strips are oriented perpendicular to the z axis, whereas the u and w strips form helices around the z axis with stereo angles of $\alpha_u = 68.85°$ and $\alpha_w = -69.26°$. Hence, the v and z layers directly measure z, and the u and w layers measure a combined $(z - \varphi)$ coordinate. The stereo layers u and w help match hits from the v and z layers with the TEC hits.

The Z-chambers operate with a gas mixture of 80% argon/20% CO_2. With an anode voltage of 1600 V, the nominal gas amplification is 5×10^4. Signals from the 960 cathode strips are read out through preamplifiers, line drivers and charge-to-digital converters. The digital part of the Z-chamber readout is integrated into the TEC readout system.

6.8 Silicon Microstrip Detector

In 1993, a silicon microstrip detector (SMD) was installed between the beampipe and TEC in order to improve track reconstruction. In particular, the SMD provides precise $r - \varphi$ and z track coordinates close to the beampipe to help reconstruct secondary vertices from particles which decay within the beampipe, *e.g.* b-hadrons and τ leptons. The intrinsic SMD resolution is 7 μm for $r - \varphi$ and 15 μm for z. The SMD was fully incorporated into physics analyses in 1994.

The SMD, illustrated in Figure 6.12, consists of two layers of double-sided silicon

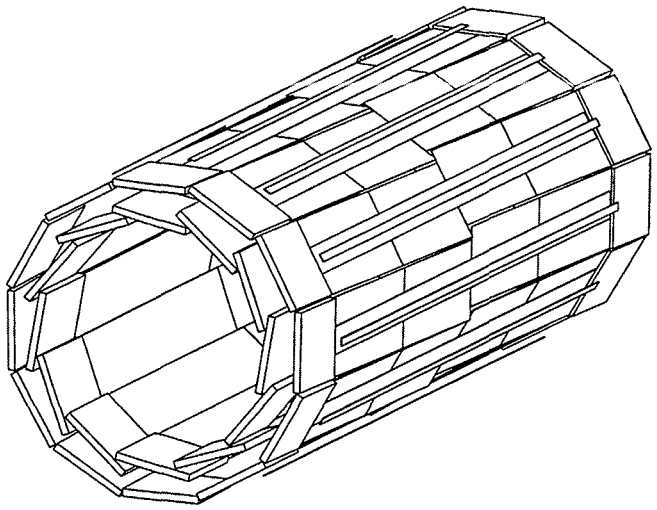

Figure 6.12: Perspective drawing of the SMD.

sensors forming two concentric cylinders surrounding the beampipe. The inner and outer sides of the sensors provide independent z and $r-\varphi$ measurements, respectively. The layers have average radii of 6.2 cm and 7.8 cm from the beam axis. Each layer has 12 "ladders" containing four silicon wafers to cover full azimuth in the polar angle region $|\cos\theta| < 0.93$.

Each of the 96 SMD wafers are 300 μm thick n-type silicon 70 mm long and 40 mm wide. The $r-\varphi$ measuring (junction) side has longitudinal strips every 25 μm and a readout pitch of 50 μm. The z measuring strips on the other (ohmic) side has strips placed every 50 μm, with the readout pitch varying from 200 μm in the region $0.53 < |\cos\theta| < 0.93$ to 150 μm in $|\cos\theta| < 0.53$. The SMD has 72576 readout channels.

Pairs of SMD wafers are read out by custom chips (SVX) mounted on the SMD ladders. These chips contain 128 channels which incorporate preamplifier, sample-and-hold, comparator, and latch circuitry. The chips also control the required multiplexing for the serial readout of all the strips. To electrically isolate the SMD readout components from the DAQ system electronics, the SVX communicates with the DAQ via an optical transceiver and fiber optic cables. Due to the large number of channels, Data Reduction Processors (DRPs) filter the incoming SMD data and transfer to the DAQ only data from strips with good hits.

6.9 Luminosity Monitor

The luminosity monitor identifies Bhabha scattering events at low polar angles to provide a measure of the LEP machine luminosity and, hence, the e^+e^- interaction rate. The luminosity monitor consists of two cylindrical BGO crystal arrays located at $z = \pm 2.7$ m from the interaction point. Each array contains 304 BGO crystals which span polar angle regions $25 < \theta < 70$ mrad ($1.4° < \theta < 4.0°$) from the beam axis. To prevent unnecessary radiation damage, the arrays are split into halves which can be moved radially in and out by a hydraulic device with a 10 μm positioning accuracy. During LEP filling and acceleration, the luminosity monitors are moved away from the beampipe. The BGO arrays are returned to normal position after the LEP operators have attained stable beam orbits. In the small polar angle region spanned by the luminosity monitor, the Bhabha scattering cross section is relatively large ($\sim$ 100 nb) and is dominated by t-channel photon exchange.

6.10 Data Acquisition and Trigger

At a beam crossing rate of 45 kHz (higher in 1994 and 1995), it is impossible to record data for every e^+e^- crossing. Moreover, not every event is interesting from a physics standpoint. Beam-related background and cosmic rays are other sources of potentially uninteresting events. After each beam crossing, the DAQ and trigger system decides if an interesting event has occurred. If so, the digitized detector data is buffered and passed along for further processing and possible recording. This event triggering has three logical levels to reduce the multi-kHz beam crossing rate to a practical tape writing rate of a few Hz.

The DAQ system is based on the FASTBUS standard. The front-end electronics produce two types of data: an approximate, coarse data available within a few μs for use in the trigger, and the fine-grained, full accuracy data to be used in higher level processing and offline analysis. The digitized data from each subdetector is stored in memory units before being merged and transferred to a workstation processing unit. The DAQ system allows the incoming data from each subdetector to be monitored online to check data quality and spot possible problems. The operating status of each subdetector is constantly monitored and recorded to a database for use in offline analyses.

To ensure high efficiency for accepting the desired physics events, the trigger system must be fast with a minimum of dead time. Redundancy is another key characteristic of an efficient trigger. The L3 trigger consists of three levels which are described in the following subsections. The given rates and thresholds are typical.

6.10.1 Level-1 Trigger

The level-1 trigger is the logical OR of five subtriggers from the calorimeters, luminosity monitor, scintillation counters, TEC, and muon chambers, each of which is gated by the beam crossing signal. A positive result from any of the 5 subtriggers initiates the full digitization and buffering of the detector data. A negative result causes the front-end electronics to be cleared and readied for the next beam crossing. The level-1 accept rate is approximately 8 Hz, with a 5% dead time arising from the digitization and buffering process.

Calorimeter trigger

The level-1 calorimeter trigger selects events that deposit sizeable amounts of energy in BGO or hadronic calorimeters. This general characteristic covers many of the interesting physics channels including e^+e^-, $\tau^+\tau^-$, hadronic and $\nu\bar{\nu}\gamma$ final states.

This trigger examines the energy deposits in various blocks of BGO crystals and hadron calorimeter towers. The BGO crystals are grouped into 512 blocks, 32 around the φ direction by 16 in θ. The HCAL modules are divided into front and back layers at a depth corresponding to approximately 1 interaction length. There are $16 \times 11 = 176$ ($16 \times 13 = 208$) trigger blocks in the front (back) HCAL layers. Dedicated arithmetic and logic hardware calculate several energy sums and compare them with preset thresholds. These sums include the total (HCAL+BGO) energy, the BGO energy alone, and the total and BGO energy within the barrel region. The usual thresholds for these four energy sums are 25, 25, 15 and 8 GeV, respectively.

In addition to the above energy sums, the level-1 calorimetric trigger also looks for spatially coincident clusters in the BGO and HCAL. The θ and φ blocks are searched independently. The energy threshold for clusters is 6 GeV, but is lowered to 2.5 GeV if a TEC track coincides with an energy cluster. Single electromagnetic clusters are accepted at a threshold of 1 GeV.

The level-1 calorimeter trigger provides a positive result if any of the thresholds are exceeded. Typical trigger rates are 1-2 Hz. Electronic noise is the primary background source.

Scintillator trigger

The level-1 scintillator trigger is used primarily to identify high multiplicity events. This trigger is also used to reduce the muon trigger rate caused by cosmic rays. Hits from any of the scintillator panels within 30 ns of a beam crossing are used in this trigger. Radioactivity from the HCAL uranium causes scintillator hits coincident with beam crossings at a rate of 3 kHz. High multiplicity events are selected by requiring at least 5 scintillator hits spread over an angular region larger than 90°.

TEC trigger

The level-1 TEC trigger selects events containing charged particles. Nearly all the desired physics events fulfill this requirement. The trigger logic searches for tracks in the $r-\varphi$ plane, *i.e.*, no Z-chamber data are used.

The TEC trigger uses information from 14 anode wires in each of the 24 outer TEC sectors. The total drift time is equally divided into 2 parts, and left-right ambiguities are resolved by signals induced on the wire grids on both sides of the anode plane. Hence, the available information is a 96×14 bit matrix corresponding to 96 φ bins in 14 radial layers.

The track-finding modules search for tracks originating from the interaction point with transverse momenta of at least 150 MeV/c. A track with this momentum can cross 3 adjacent φ bins. The logic allows for missing or multiple hits along the track segment.

The trigger decision is based on the number of tracks and the acoplanarity angle between pairs of tracks. The particular values are programmable. A typical maximum acoplanarity angle is 60°. The level-1 TEC trigger rate depends on the chosen values and especially on beam-related background. Typical rates vary between 1 and 4 Hz.

Muon trigger

The level-1 muon trigger selects events with at least one track in the muon spectrometer drift chambers. Relevant physics channels include the $\mu^+\mu^-$, $\tau^+\tau^-$ and multihadron final states.

Hits from the P and Z chambers are fed into hardware logic which searches for tracks with transverse momentum > 1 GeV/c originating from the interaction point. Muon chamber tracks passing the level-1 trigger requirements must have matched hits in 2 of 3 P chamber layers and 3 of 4 Z chamber layers.

The level-1 muon trigger alone has a rate of 10 Hz dominated by impinging cosmic rays coincident with the beam gate. The trigger rate is reduced to 1 Hz by demanding a muon trigger with an in-time scintillator hit.

Luminosity trigger

The luminosity trigger selects low angle Bhabha scattering events by requiring significant energy deposits in the luminosity monitor. The monitor crystals on each side are grouped into 16 φ sectors. A positive trigger decision results if any of the following three conditions are fulfilled: back-to-back (within $\pm$ 1 sector) clusters in the two monitors each $\geq$ 15 GeV; total energy in one monitor $\geq$ 25 GeV and $\geq$ 5 GeV in the other; total energy in either monitor $\geq$ 30 GeV. The typical trigger rate of 1.5 Hz depends on the LEP luminosity and can increase dramatically from beam-related background.

6.10.2 Level-2 Trigger

The purpose of the level-2 trigger is to reject background events which passed the level-1 trigger. Such events include spurious calorimetric triggers caused by electronic noise, as well as TEC triggers from beam-gas and beam-wall interactions. The input data for the level-2 trigger include the same coarse trigger data used in level-1, the level-1 trigger results, and more detector data which was unavailable for level-1 decision (*e.g.*, signals from the TEC charge division wires). Luminosity triggers and events satisfying more than one level-1 subtrigger pass the level-2 trigger automatically. The level-2 trigger can spend more time processing an event than the level-1 trigger without the penalty of additional detector deadtime. After a positive result, the level-2 trigger passes its input and output to the level-3 trigger. The complete digitized detector data is combined and also passed on to level-3. The level-2 trigger rejects 20-30% of the events passed by level-1. The level-2 trigger acceptance rate is < 6 Hz.

6.10.3 Level-3 Trigger

Like the level-2 trigger, the level-3 trigger rejects unwanted background events. Three 3081/E computers (IBM 370 emulators) equipped with FASTBUS interfaces serve as the heart of the level-3 trigger. These computers run FORTRAN-based algorithms which use the fully digitized detector data to apply more stringent background rejection criteria. Luminosity triggers and events passing more than one level-1 subtrigger automatically pass the level-3 trigger. Muon triggers must have an associated scintillator hit within $\pm$ 10 ns of a beam crossing. In TEC trigger events, the quality of the tracks is checked and a vertex is reconstructed. The level-3 trigger also attempts to match TEC tracks with calorimeter clusters. The level-3 trigger reduces the event rate by another 40-60% for an output rate of 2-3 Hz. After a positive level-3 decision, the trigger information and event data are transferred to the main online workstation which spools the data to tape. Other online computers monitor the data quality and subdetector performance.

6.11 Detector Simulation

Understanding systematic effects is an important aspect of any precision measurement. Like most other high energy physics experiments, the L3 detector is a complex apparatus whose performance can be more complicated to describe than is possible by analytic formulæ alone. Computer-based simulations allow a more thorough modeling and understanding of the detector response to physics events.

Event simulation takes place in three steps. First, a Monte-Carlo event generator program creates a sample of the desired physics events with their final state particles and four-momenta. Next, a detector simulation program reads the generated events and simulates the detector response. Finally, the simulated event is reconstructed using the same software that is used to reconstruct data events.

The L3 detector simulation program (SIL3) is based on the GEANT (version 3.14) software package [41] for describing the physical properties of detector media and simulating particle interactions. The GHEISHA program [42] is used to simulate hadronic interactions. SIL3 includes detailed geometries of each subdetector down to scales of 10-100 μm. The simulation tracks particles through the detector while taking into account processes such

as secondary decays, energy loss, multiple scattering, nuclear interactions, bremsstrahlung, pair production and photofission. To describe showers in the calorimeters, the simulation tracks particles with energy down to $\approx$ 10 keV in the BGO and $\approx$ 1 MeV in the HCAL. Results from test beam projects were used to fine-tune simulation parameters.

Time-dependent detector inefficiencies and imperfections, *e.g.* noisy BGO crystals and disconnected chamber wires, are also simulated using the the subdetector status and calibrations stored in the L3 database. During reconstruction, simulated events are assigned a time and date from the relevant data-taking period with the correct luminosity weighting. The database information corresponding to that time and date are applied to the event, so that dead or noisy channels are discarded and the appropriate calibrations are applied.

Before performing any physics analyses, the simulation quality is checked by comparing various distributions from simulation and actual data. Discrepancies may indicate the need to correct the detector modeling. Large samples of Monte-Carlo events, preferably 5-10 times larger than the relevant data sample, allow an adequate study of systematic detector effects while limiting the effects of statistical fluctuations in the simulation sample itself.

CHAPTER 7

EVENT SELECTION

This chapter describes the selection of $Z \rightarrow \tau^+\tau^-$ events used in this analysis. This description includes event preselection, neutral cluster reconstruction, charged pion energy measurement, particle identification, and background rejection. The estimations of selection efficiencies and background fractions are also presented.

7.1 Data Sample

The data sample used for this analysis consists of e^+e^- interactions recorded by the L3 detector during the 1991-1995 LEP collider running periods. The center-of-mass energies are concentrated at several points around the Z resonance peak. Approximately 75% of the recorded luminosity occurred at $\sqrt{s} = M_Z$, while much of the remainder was divided roughly equally among the points $\sqrt{s} \approx M_Z \pm 1.8$ GeV. Figure 5.3 shows the recorded luminosity per year. The whole data sample contains 148 pb^{-1}.

7.2 Event Selection

An ideal event selection would select all of the desired events while rejecting all possible backgrounds. However, this goal is virtually impossible to attain. One hopes to accept a large fraction of the desired events while minimizing the background contamination. In this analysis, we want to select a sample of $Z \rightarrow \tau^+\tau^-$ decays and then correctly identify the various τ decay modes. Because the energies of the τ decay products depend on the polarization, the selection should not depend strongly on energy in order to minimize any

potential measurement bias. It is straightforward to obtain a clean sample of $Z \rightarrow \tau^+\tau^-$ decays, and most of the background in the final event sample arises from the misidentification of τ decays.

Three steps comprise the selection of the event sample. First, we obtain a clean sample of $Z \rightarrow \ell^+\ell^-$ decays. These leptonic Z decays are distinguished from hadronic Z decays according to particle multiplicity; hadronic Z decays typically contain many more particles than $Z \rightarrow \ell^+\ell^-$. The preselection also diminishes backgrounds from cosmic rays and two-photon interactions by simple requirements.

The second selection step is particle identification. Each event is divided into two hemispheres which are analyzed independently. An attempt is made to identify the particles as electrons, muons, pions or rho mesons based on tracks reconstructed in the central tracker, calorimeter energy deposits and tracks in the muon chambers.

The final step involves event classification and rejection of the remaining background from non-τ sources. Events containing at least one π or ρ are retained. These events are then classified into one of the five event categories ρX, πX, $\rho\rho$, $\pi\pi$ or $\rho\pi$. Additional cuts are applied to further reduce the background from non-τ sources.

The three steps of the selection process are described more fully in the following subsections.

7.2.1 Event Preselection

The goal of preselection is to obtain a clean sample of leptonic Z decays $Z \rightarrow \ell^+\ell^-$ where ℓ can be an electron, muon, or tau. These events tend to have a single track or low-multiplicity jet in each hemisphere roughly back-to-back with each other. Figures 7.1 and 7.2 are displays of $Z \rightarrow \tau^+\tau^-$ events in the $r-\varphi$ and $r-z$ planes, respectively. (The charged tracks are depicted by solid lines connecting open circles, BGO clusters are represented by "towers" whose lengths are proportional to the energies in the crystals, and HCAL clusters are portrayed by squares whose areas are proportional to the tower energies.) The preselection separates $Z \rightarrow \ell^+\ell^-$ decays from the more numerous hadronic decays $Z \rightarrow q\bar{q}$. Preselection also reduces the background from two-photon interactions and cosmic rays passing through the detector.

Hadronic Z decays are rejected using the following cuts:

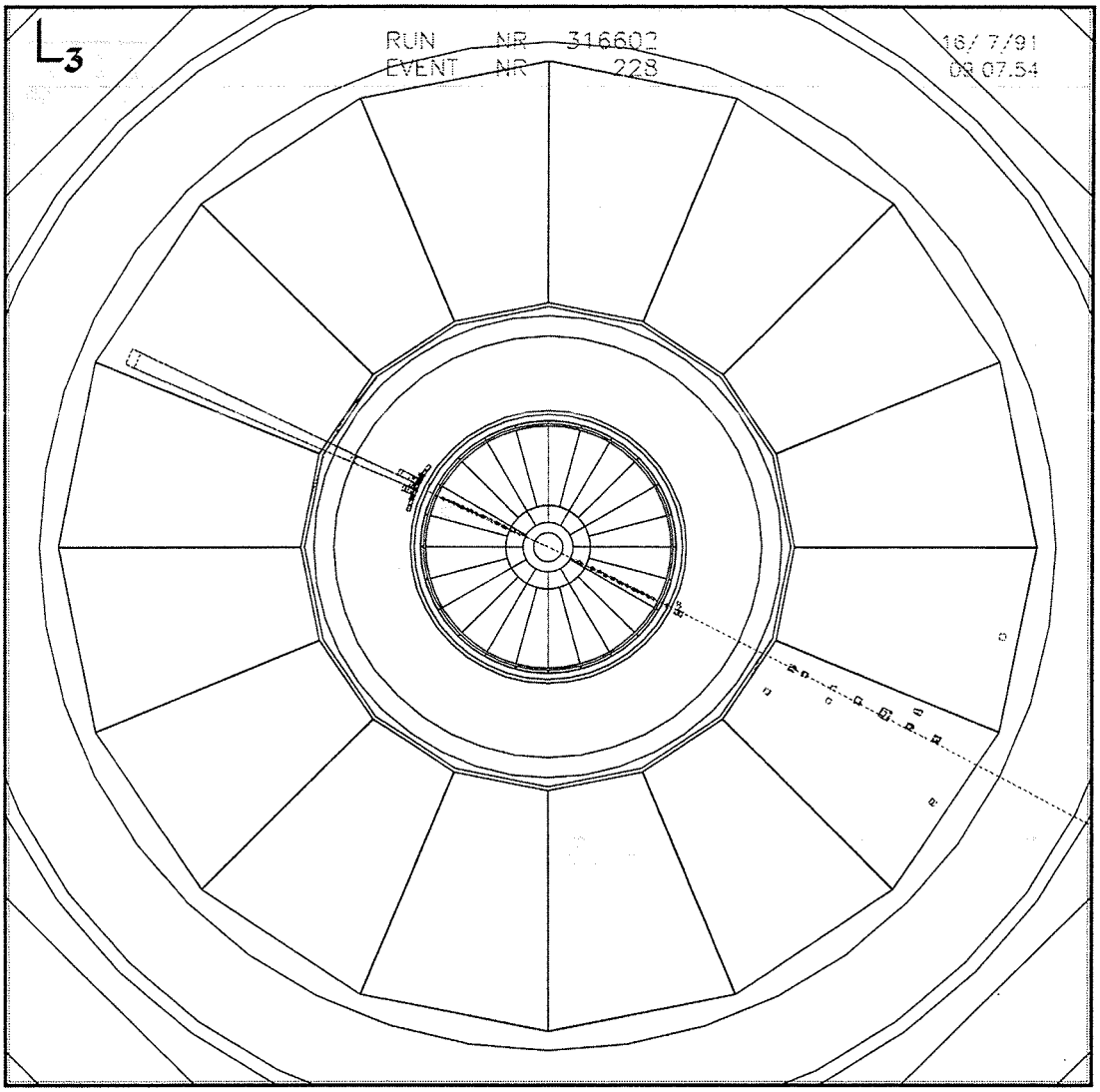

Figure 7.1: A view of a $Z \rightarrow \tau^+\tau^-$ event in the $r-\varphi$ plane. The particle on the left side is an electron from $\tau^- \rightarrow e^-\bar{\nu}_e\nu_\tau$, and the particle on the right side is a muon from $\tau^+ \rightarrow \mu^+\nu_\mu\bar{\nu}_\tau$. Only the barrel subdetectors within the support tube are shown.

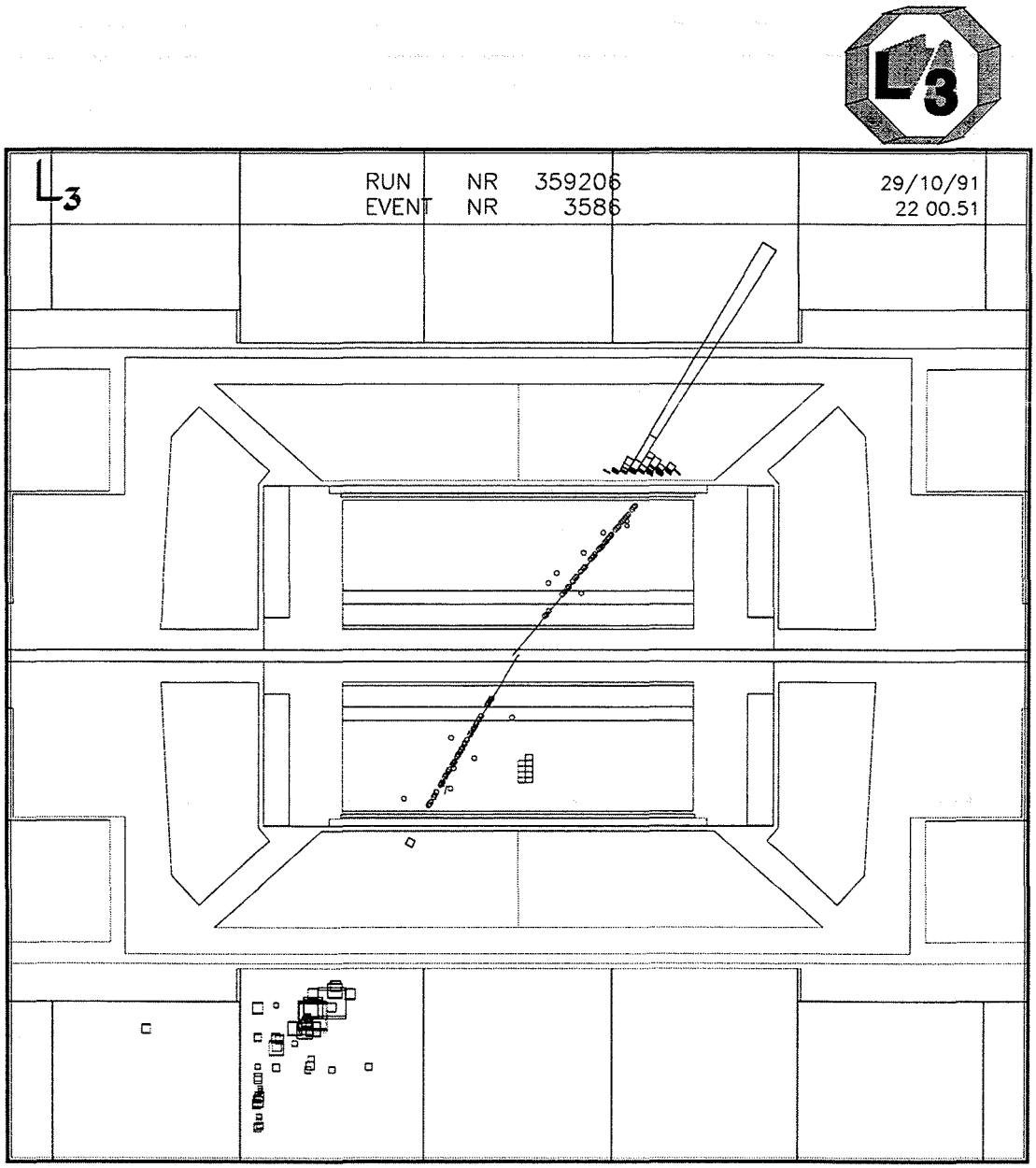

Figure 7.2: A view of a $Z \rightarrow \tau^+\tau^-$ event in the $r-z$ plane. A π^- and a π^o from $\tau^- \rightarrow \rho^-\nu_\tau$ are in the top half, and in the bottom is a π^+ from $\tau^+ \rightarrow \pi^+\bar{\nu}_\tau$.

1. the event has at most 8 TEC tracks;

2. both hemispheres have 5 or fewer TEC tracks;

3. one hemisphere has at most 3 TEC tracks;

4. the event has at most 25 clusters in the BGO calorimeter;

5. the φ separation between each track and the thrust axis is less than 30°.

The first four cuts exploit the high particle multiplicity in typical hadronic Z decays. Figure 7.3 shows a reconstruction of a $Z \rightarrow q\bar{q}$ event; note the large number of tracks and calorimeter clusters relative to $Z \rightarrow \tau^+\tau^-$. The jet of decay products in multihadronic τ decays is highly collimated due to the high Lorentz boost and relatively low τ mass. However, the jets in $Z \rightarrow$ hadrons can be broader as a result of gluon emission and fragmentation during the hadronization process. Cut number 5 diminishes this type of background. These cuts 99.9% reject of the $Z \rightarrow$ hadrons events and reject less than 2% of the $Z \rightarrow \ell^+\ell^-$ events [43].

Two-photon interactions $e^+e^- \rightarrow e^+e^- f\bar{f}$ are another source of background for $Z \rightarrow \ell^+\ell^-$ events. (These events are called two-photon events because the e^+ and e^- interact via two virtual photons.) In these events, the e^- and e^+ often scatter at low angles and escape detection by remaining within the beampipe. Only the fermion-antifermion pair $f\bar{f}$ is observed in the detector. The $f\bar{f}$ system characteristically has low energy and is boosted along the beam axis. Consequently, the two tracks are not back-to-back and each has a small transverse momentum. Two-photon background is suppressed by requiring:

1. at least 1 TEC track with transverse momentum > 0.5 GeV/c with respect to the beam axis;

2. at least 2 GeV of energy in the event.

Cosmic ray muons penetrate the experimental cavern constantly and interact with the detector. Most of these muons arrive outside the beam-crossing intervals and leave tracks or calorimeter deposits which appear to originate far from the interaction point. At the preselection stage, cosmic rays are rejected by demanding:

1. at least 1 TEC track passing within 15 mm of the interaction point in the plane normal to the beam axis;

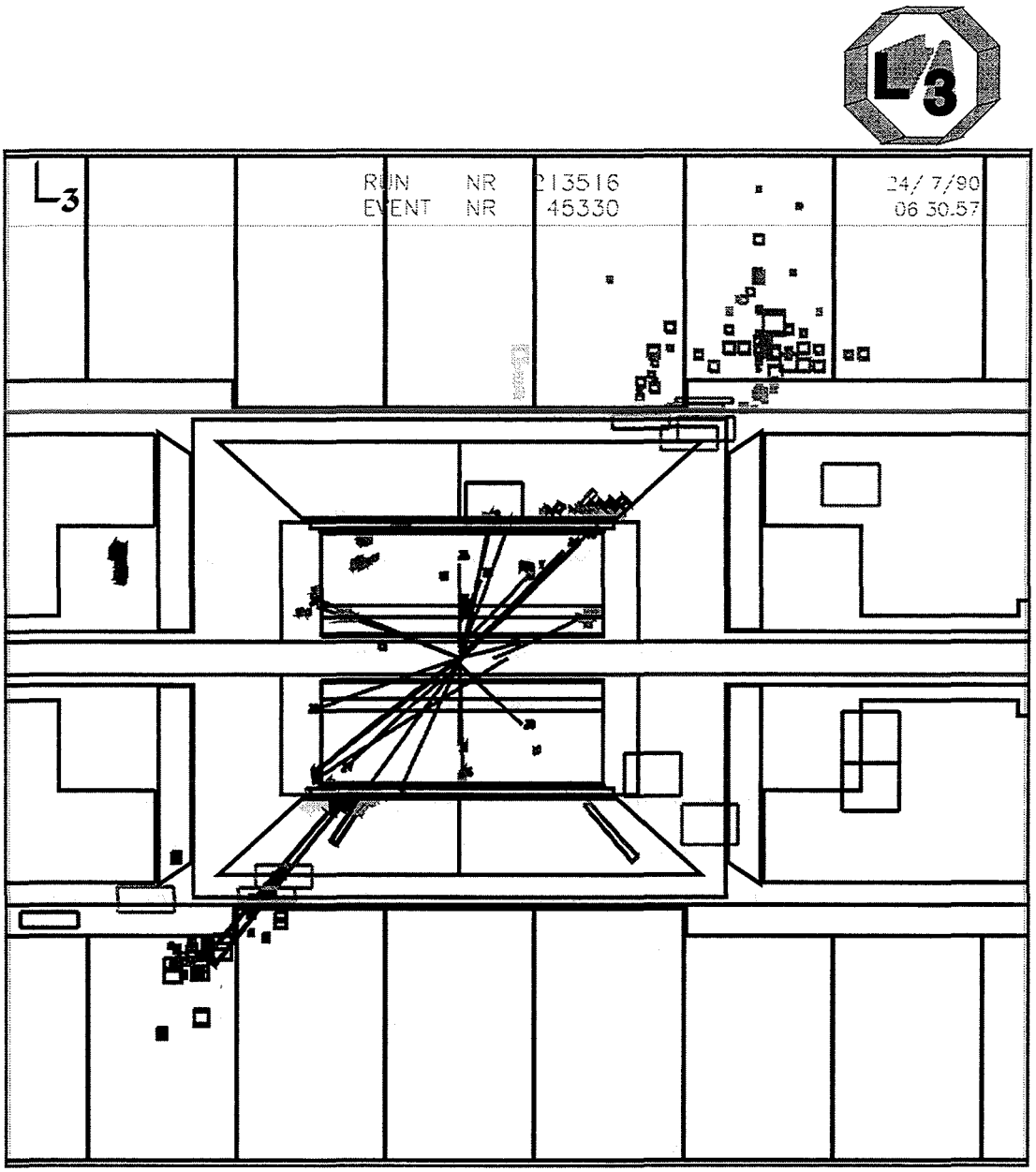

Figure 7.3: A view of a typical $Z \rightarrow q\bar{q}$ decay in the $r - z$ plane as reconstructed with the L3 detector.

2. at least one scintillator hit within ±10 ns of the beam crossing.

After imposing the preselection cuts, the remaining data sample contains 98% of the original leptonic Z decays within the fiducial volume $|\cos\theta| < 0.8$. The 5% background consists mainly of two-photon events and cosmics [43]. Additional cuts applied in the final selection will further diminish background from cosmics and two-photon events.

7.2.2 Particle Identification

Particle identification is the second step of the event selection procedure. Events in the preselected sample are divided into two hemispheres by the plane that is perpendicular to the event's thrust axis and contains the nominal interaction vertex. The thrust axis is defined by the unit vector $\vec{n}$ maximizing the quantity (called *thrust*):

$$T = \max\left[\sum_i |\vec{p}_i \cdot \vec{n}| \,/\, \sum_i |\vec{p}_i|\right], \tag{7.1}$$

where $\vec{p}_i$ denotes the momentum of the i^{th} particle, and the summations are over all particles in the event. We then attempt to identify the particles in each hemisphere independently.

The particles we attempt to identify include charged and neutral pions, electrons, and muons. Tau leptons also have decays involving kaons, but we do not distinguish between charged pions and kaons. No attempt is made to identify neutral kaons. Rho mesons are identified via their $\rho^- \to \pi^-\pi^o$ decay.

We distinguish the various particles by their characteristic charged track and calorimeter shower topology. The pertinent τ decay modes involve single charged tracks. In order to precisely determine where the charged particle impacts the BGO calorimeter, the tracks must have an associated Z-chamber hit. This requirement confines the identification to tracks with polar angle $42° < \theta < 138°$. The event thrust axis must lie within the region $|\cos\theta| < 0.7$.

Neutral Cluster Separation and π^o Identification

An important step in identifying $\tau^- \to h^-\nu_\tau$ decays is a search for neutral clusters in the BGO which overlap the shower of the charged hadron. The neutral clusters are the decay photons of the π^o's ($\pi^o \to \gamma\gamma$) present in $\tau^- \to \rho^-\nu_\tau$ and $\tau^- \to a_1^-\nu_\tau$ decays. The large Lorentz boost of the τ, $E_\tau/m_\tau \approx 25$, causes the charged hadron decay products to lie

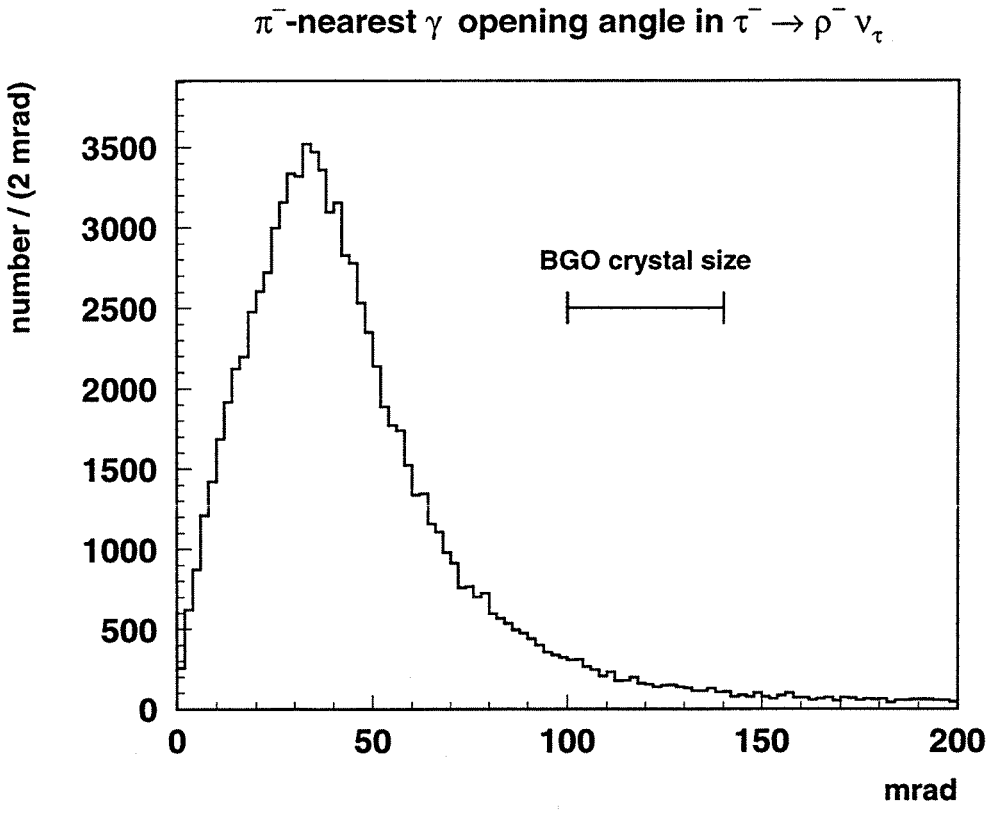

Figure 7.4: The opening angle distribution between the π^- and the nearest photon in $\tau^- \rightarrow \rho^- \nu_\tau$ decays from a $e^+e^- \rightarrow Z \rightarrow \tau^+\tau^-$ Monte-Carlo sample.

within a narrow cone in the lab frame. For example, Figure 7.4 illustrates the opening angle distribution between the π^- and the nearest γ in $\tau^- \rightarrow \rho^- \nu_\tau$ decays from a Monte-Carlo generated sample of $Z \rightarrow \tau^+\tau^-$ decays. The peak of the distribution occurs near 40 mrad which corresponds to the angular size of the BGO crystals as seen from the interaction point. Given that the lateral shape of BGO showers typically spans a 3×3 matrix of crystals surrounding the impact point, and at least one of the π^o decay photons usually lies within 2 crystal widths of the π^- in $\tau^- \rightarrow \rho^- \nu_\tau$, the BGO showers of the ρ^- decay products often overlap. Overlapping charged and neutral showers is also a concern for $\tau^- \rightarrow a_1^- \nu_\tau$ in which the a_1^- decays to $\pi^-\pi^o\pi^o$. Losing one or more photons in the charged hadron shower or incorrectly measuring the neutral cluster energies can cause misidentification of the τ decay.

An algorithm was developed to determine the energies and positions of photon

candidates whose BGO showers overlap with the energy deposit of a charged hadron [43]. The algorithm uses the charged hadron's extrapolated impact point on the BGO along with the average lateral shapes of electromagnetic and hadronic showers in the BGO. The lateral profiles for electromagnetic showers were obtained from $Z \rightarrow e^+e^-$ data, while the hadronic shower energy profiles were obtained in a pion test-beam study [44]. Figure 7.5 illustrates the steps of the algorithm presented here:

1. Using the TEC and Z-chamber hits, the path of the charged track is extrapolated to the BGO to determine the impact point on the so-called *central crystal* (Figure 7.5a).

2. The lateral energy profile of the charged particle shower is estimated by an average hadronic shower profile normalized to the energy of the central crystal. This energy profile is subtracted from the raw energy of every crystal within a 30° half-angle cone around the central crystal (Figure 7.5b).

3. Any remaining local maxima in BGO energy (neutral clusters) are photon candidates (Figure 7.5c). The energy profiles of these candidates are fit with electromagnetic shower shapes to obtain obtain energy and position measurements.

4. The energies of the reconstructed neutral shower profiles are subtracted from the original raw BGO crystal energies to provide a better estimate of the charged hadron energy deposited in the central crystal (Figure 7.5d).

Steps 2-4 are repeated until the reconstructed energies are stable to 1% which usually requires only three or four iterations.

After reconstructing neutral clusters using the algorithm just described, neutral pions are identified in the BGO via their decay $\pi^o \rightarrow \gamma\gamma$. In $e^+e^- \rightarrow Z \rightarrow \tau^+\tau^-$ at $\sqrt{s} \approx M_Z$, neutral pions arising from $\tau^- \rightarrow \rho^-\nu_\tau$ decays typically have lab frame energies above 1 GeV. The Lorentz boost causes the π^o decay photons to be highly collimated. Consequently, it is not always possible to resolve two distinct photons, so π^o candidates can consist of one or two neutral clusters in the BGO.

Two distinct electromagnetic neutral clusters form a π^o candidate if both cluster energies are greater than 500 MeV and their invariant mass is within 30 to 60 MeV, depending on the cluster energies, of the π^o mass (135 MeV). A single neutral cluster is considered a π^o candidate if it has an electromagnetic shower shape and energy greater than 1 GeV. For a cluster whose lateral shape agrees better with two nearly merged showers, the invariant

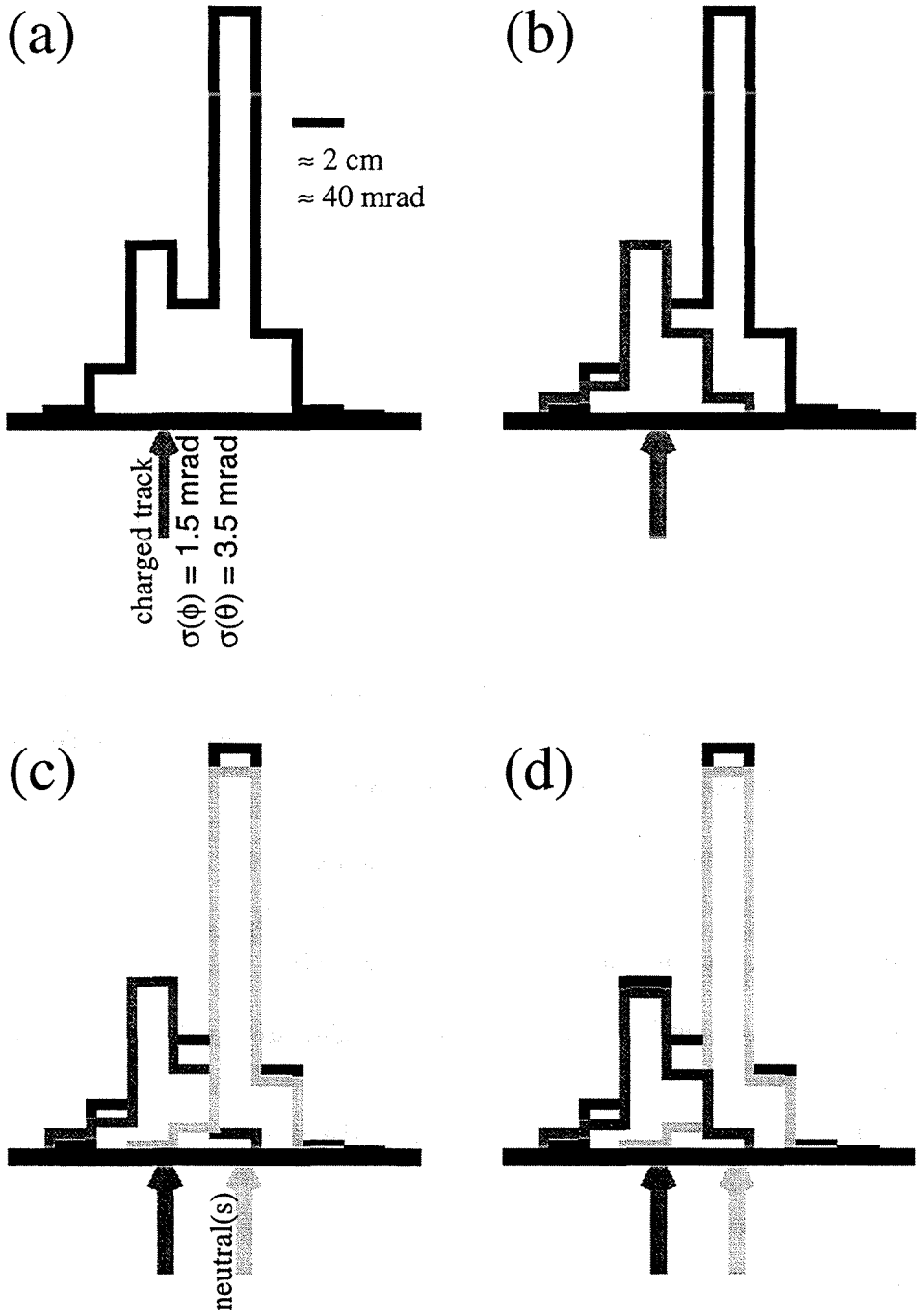

Figure 7.5: Illustration of the algorithm used to reconstruct neutral clusters overlapping a charged hadron shower in the BGO. Each panel represents the energy deposition of several neighboring crystals. The horizontal axis corresponds to individual crystals, and the vertical axis represents the energy deposited in the crystals.

mass must be within approximately 50 MeV of the π^o mass. The reconstructed mass of the π^o candidates in hemispheres identified as $\tau^- \to \rho^- \nu_\tau$ is shown in Figure 7.6 for both data and Monte-Carlo.

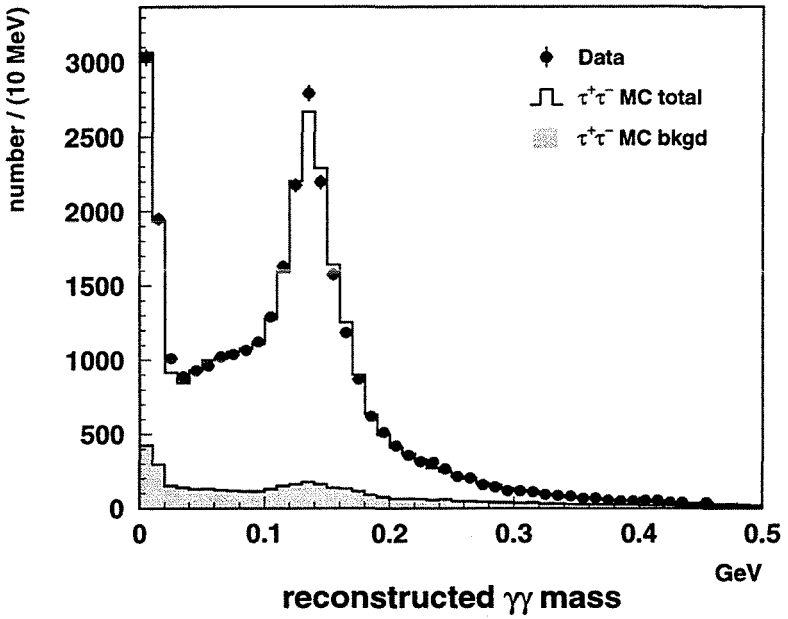

Figure 7.6: The reconstructed mass of the π^o candidates in the hemispheres identified as $\tau^- \to \rho^- \nu_\tau$.

π^- Energy Measurement

To determine the energy of the charged hadron in $\tau^- \to h^- \nu_\tau$, the energies of reconstructed photons and neutral pions are subtracted from the BGO energy in that hemisphere. An estimate of the charged hadron energy is based on the remaining BGO energy, E_B, and the HCAL energy deposition, E_H, according to the sum:

$$E_{CAL} \;=\; f_B(E) \cdot E_B \;+\; f_H(E) \cdot g_H(\theta, \varphi) \cdot E_H \;. \tag{7.2}$$

The coefficients f_B and f_H are energy-scale corrections obtained from test-beam calibrations and data. The factor g_H accounts for the nonuniform HCAL response due to its modular structure.

The π^- calorimetric energy measurement is combined with the independent transverse momentum p_T measurement from the tracking chambers in order to improve the π^- energy resolution. The charged hadron energy is taken to be the energy which maximizes the probability that the measured calorimetric energy and transverse momentum result from a pion with energy E_π, given energy and track curvature resolutions σ_{CAL} and σ_{1/p_T}:

$$P_{\text{combined}}(E_\pi) = \frac{1}{\sqrt{2\pi\sigma^2_{CAL}(E_\pi)}} \exp\left[-\frac{(E_{CAL}-E_\pi)^2}{2\sigma^2_{CAL}(E_\pi)}\right] \times \frac{1}{\sqrt{2\pi\sigma^2_{1/p_T}}} \exp\left[-\frac{(1/p_T - 1/(E_\pi \sin\theta))^2}{2\sigma^2_{1/p_T}}\right]. \tag{7.3}$$

The actual maximum probability obtained with this method is defined to be the compatibility of the energy and momentum measurements.

The average charged pion energy resolutions from tracking alone, calorimetry alone, and the combined measurement are illustrated in Figure 7.7. The average tracking resolution, given by $\sigma_{1/p_T} = 0.011 p_T$ (GeV/c)$^{-1}$ if the reconstructed track contains SMD hits, and $\sigma_{1/p_T} = 0.018 p_T$ (GeV/c)$^{-1}$ without SMD hits, is much better than the calorimeter energy resolution $\sigma_{CAL} = 8\% + 55\%/\sqrt{E_\pi}$ at low energies, while the HCAL is more precise at high

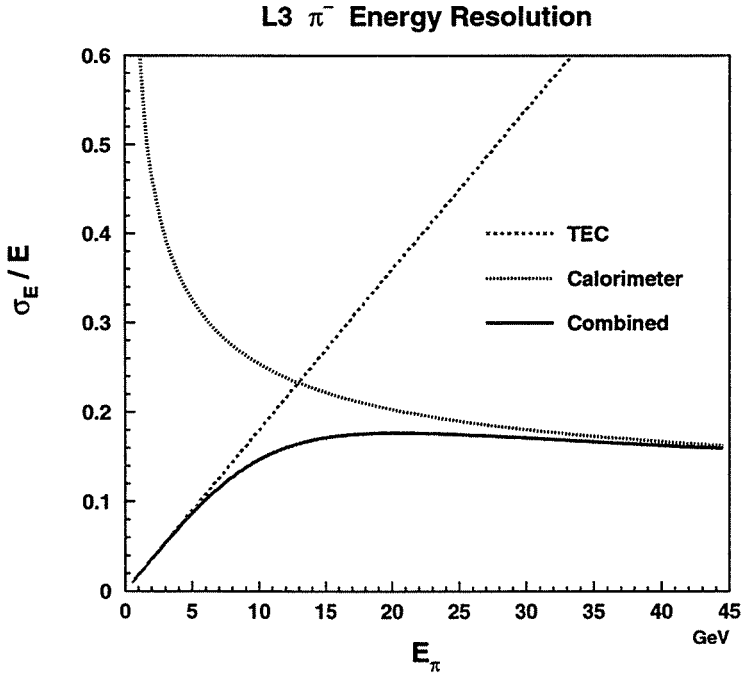

Figure 7.7: The average π^- energy resolutions versus π^- energy for momentum measurement alone, calorimetric energy measurement alone, and the combined measurement.

energies. The combined measurement provides the greatest resolution improvement for π^- energies in the 10-25 GeV range.

Identification of $\pi^{\pm}$

To be considered as a $\tau^- \to \pi^- \nu_\tau$ decay, a hemisphere must contain a single TEC track and have at least 200 MeV in the BGO or 600 MeV in the HCAL within the 30° half-angle cone around the track. Electrons are rejected by cutting on the BGO lateral shower shape. Muons are rejected if the calorimeter deposits are consistent with that of a MIP, or if a track in the muon chambers extrapolates back to the interaction point.

If the hemisphere passes the cuts outlined above, it must also satisfy the following requirements to be identified as a $\tau^- \to \pi^- \nu_\tau$:

1. no identified π^o or extra neutral clusters with energy greater than 500 MeV;
2. the energy-momentum compatibility is greater then 0.003 (Figure 7.8);
3. no track in the muon chambers with measured momentum greater than 30 GeV;
4. the total BGO energy within the 30° half-angle cone around the track is less than 35 GeV.

The first cut reduces background from $\tau^- \to \rho^- \nu_\tau$ and one-prong $\tau^- \to a_1^- \nu_\tau$ decays. The second cut eliminates tracks with inconsistent energy and transverse momentum, perhaps caused by poor measurements or by a neutral particle shower completely overlapping the charged particle shower. Cut three rejects muons from $\tau^- \to \mu^- \bar{\nu}_\mu \nu_\tau$ and $Z \to \mu^+ \mu^-$ while cut four rejects electrons from $\tau^- \to e^- \bar{\nu}_e \nu_\tau$ and $Z \to e^+ e^-$.

Identification of $\rho^{\pm}$

A hemisphere is selected as a $\tau^- \to \rho^- \nu_\tau$ decay if the following identification criteria are satisfied:

1. the hemisphere contains one TEC track and one identified π^o;
2. any extra neutral clusters have energy less than 500 MeV;
3. the energy-momentum compatibility is greater then 0.001;
4. no track in the muon chambers with measured momentum greater than 30 GeV;

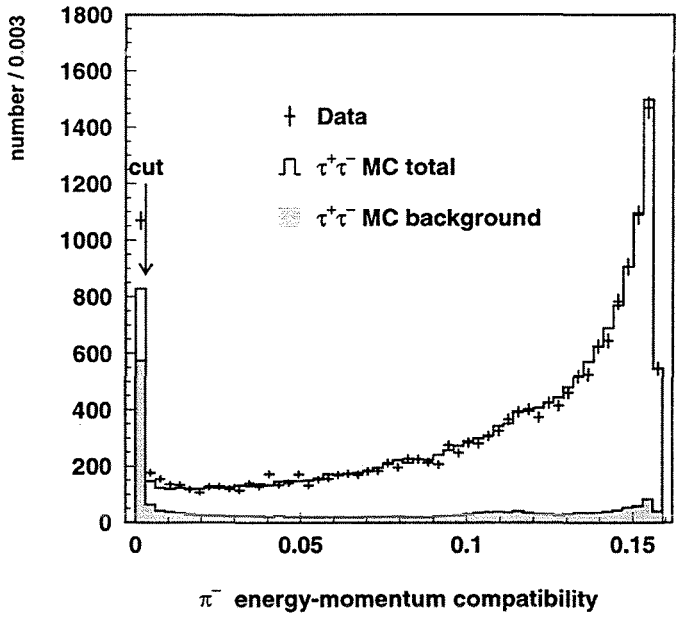

Figure 7.8: The π^- energy-momentum compatibility distribution for hemispheres identified as $\tau^- \to \pi^-\nu_\tau$ without applying the cut on the compatibility. The arrow indicates the cut value. All other cuts have been applied.

5. the total BGO energy in the 30° half-angle cone around the the track is less than 44 GeV;

6. the ρ^- energy, equal to the sum of the π^- and π^o energies, must be greater than 5 GeV;

7. the $\pi^-\pi^o$ invariant mass $m_{\pi^-\pi^o}$ is in the range $0.45 < m_{\pi^-\pi^o} < 1.2$ GeV.

The first requirement is obvious, and cuts 2-5 serve the same purpose as in the $\tau^- \to \pi^-\nu_\tau$ identification. Cut 3 is looser than the analogous cut for $\tau^- \to \pi^-\nu_\tau$ because of the possible BGO energy misassignment between the π^- and the π^o. Cut 6 is motivated by kinematics; the minimum lab frame ρ^- energy in $\tau^- \to \rho^-\nu_\tau$ with $E_\tau = 45.6$ GeV is approximately 5 GeV. Cut 7 requires the $\pi^-\pi^o$ invariant mass to be consistent with the nominal ρ^- mass. Figure 7.9 shows the $\pi^-\pi^o$ invariant mass distribution for selected $\tau^- \to \rho^-\nu_\tau$ hemispheres before applying cut 7.

In the data, only 17.4% of the π^o's have fully resolved decay photons, as compared to 18.7% in the Monte-Carlo. Since the $\tau^- \to \rho^-\nu_\tau$ selection efficiency and ω spectrum

differ slightly for resolved and unresolved π^o, the Monte-Carlo distributions are reweighted to match the resolved π^o fraction observed in the data.

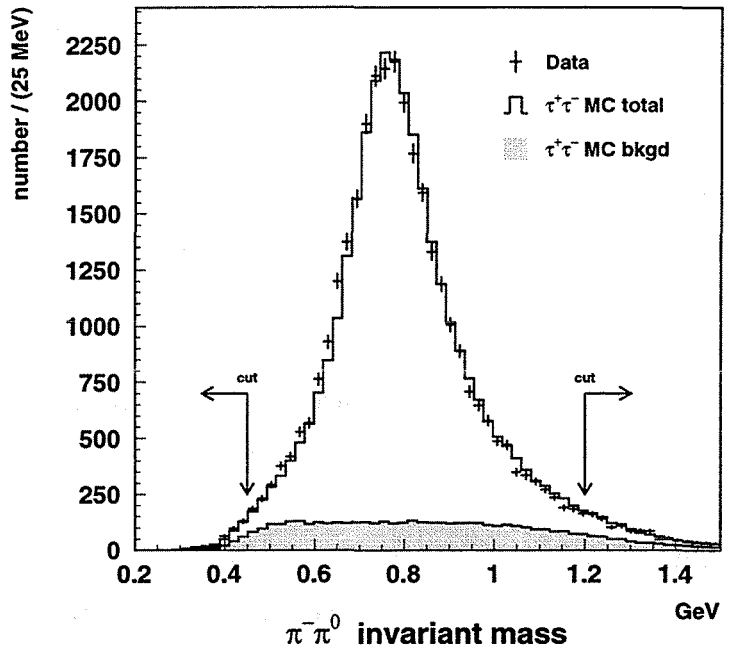

Figure 7.9: The $\pi^-\pi^o$ invariant mass distribution for hemispheres with an identified $\tau^- \to \rho^-\nu_\tau$. The arrows indicate the cut regions. All other cuts have been applied.

7.2.3 Event Classification and Non-τ Background Rejection

Assigning events into one of the five classes and further reducing background from non-τ sources is the final step of the event selection procedure. Only events with at least one hemisphere identified as $\tau^- \to \pi^-\nu_\tau$ or $\tau^- \to \rho^-\nu_\tau$ are retained. These events are then grouped into one of the five event classes ρX, πX, $\rho\rho$, $\pi\pi$, and $\rho\pi$, according to the identified τ decay in each hemisphere. The X, or *opposite*, hemisphere in ρX and πX is not identified as $\tau^- \to \pi^-\nu_\tau$ or $\tau^- \to \rho^-\nu_\tau$.

The remaining non-τ background in each event class is reduced by applying *correlated* cuts. These correlated cuts involve characteristics of the opposite hemisphere (ρX and πX) or the event as a whole, in contrast to the particle identification which considered each

hemisphere independently.

Bhabha ($Z \rightarrow e^+e^-$) and dimuon ($Z \rightarrow \mu^+\mu^-$) events cause background when at least one of the electrons or muons fakes a ρ or π signature. Such misidentification can arise as a result of a particle passing through a subdetector gap, or a large fluctuation of its shower profile in the calorimeters. The probability of both leptons in a Bhabha or dimuon event faking a pion or rho is quite low. The total BGO energy is required to be less than $0.9\sqrt{s}$ for ρX and $\rho\rho$ events, and less than $0.68\sqrt{s}$ for events in the πX, $\pi\pi$ and $\rho\pi$ classes. The calorimeter deposits in both hemispheres must be inconsistent with MIP signatures if there is no associated track in the muon chambers. The $Z \rightarrow e^+e^-$ and $Z \rightarrow \mu^+\mu^-$ backgrounds in ρX and πX can be easily identified by the peaks near 45 GeV in the electron and muon energy distributions from the opposite ("X") hemisphere, as shown in the top plots of Figures 7.10 and 7.11. Much of the Bhabha and dimuon background in ρX and πX is eliminated by rejecting events with an opposite hemisphere electron or muon with an energy greater than 40 GeV.

Two other quantities examined for rejecting non-τ backgrounds are the track acollinearity and distance-of-closest-approach (DCA). The acollinearity of two tracks is defined as the angle between the tracks subtracted from π radians, as illustrated in Figure 7.12. Two tracks exactly back-to-back have zero acollinearity. A track's DCA, shown in Figure 7.13, is the minimum distance (in the $x - y$ projection) between the track's trajectory and the interaction vertex. Primary tracks originating from the Z decay vertex have very small DCA, whereas tracks from cosmic ray muons and beam-related backgrounds can have large DCA.

Backgrounds from two-photon events are reduced by cutting on acollinearity. The acollinearity in ρX and $\rho\rho$ events is required to be less than 640 mrad (about 11°), while the πX, $\pi\pi$ and $\rho\pi$ events have a tighter cut of 340 mrad (about 6°). The acollinearity cut is looser for the former events because the minimum energy of the ρ candidate considerably reduces $\gamma\gamma$ background by itself. The charged tracks in events with an identified π must also have a transverse momentum difference greater than 1 GeV when both hemispheres have BGO energy deposits less than 2 GeV and less than 5 GeV in the HCAL. This cut exploits the balanced transverse momentum in two-photon events. The bottom left plots in Figures 7.10 and 7.11 depict the acollinearity distributions of tracks in the ρX and πX classes.

In addition to the preselection timing requirements, imposing restrictions on track

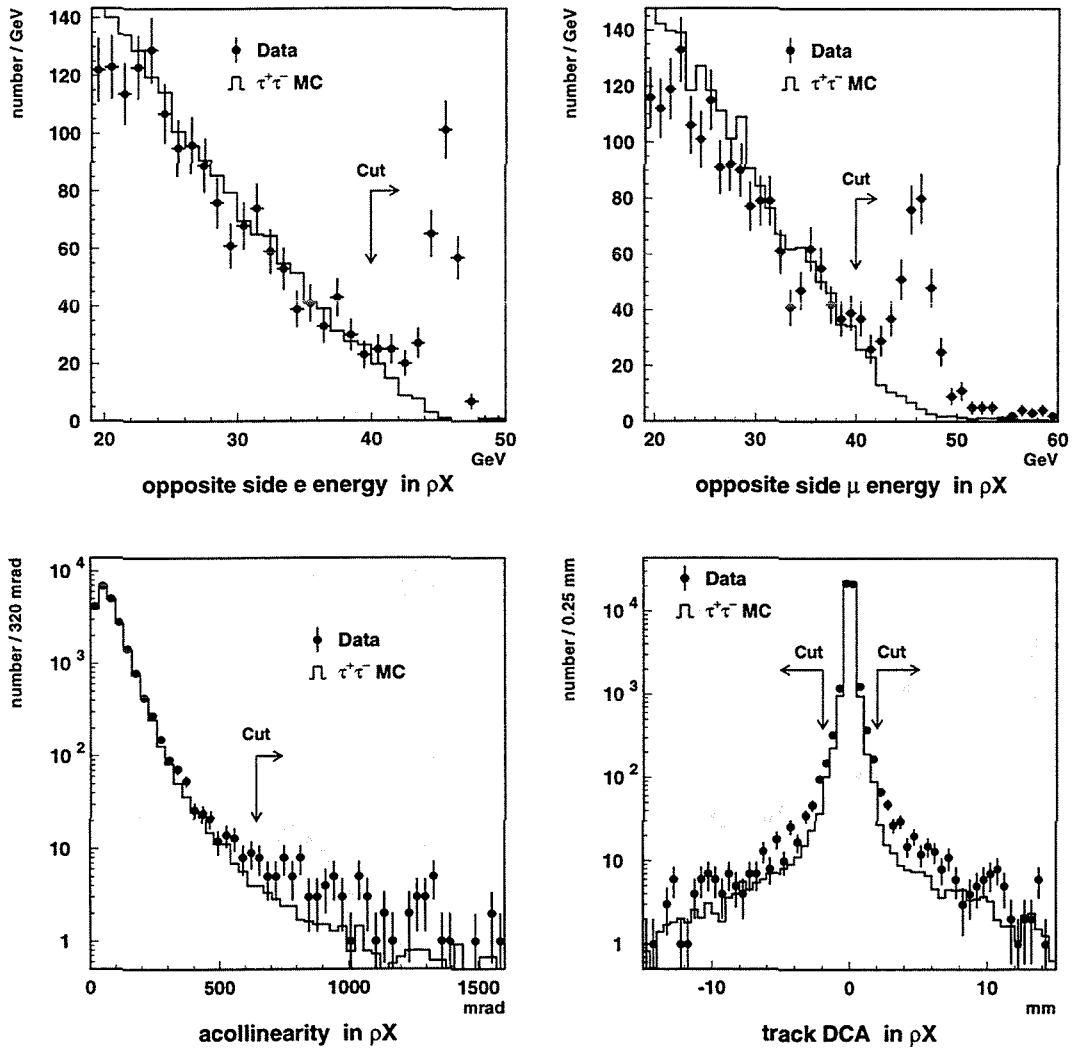

Figure 7.10: Quantities used to reject non-τ background in the selected ρX sample. For each plot, all other cuts have been applied.

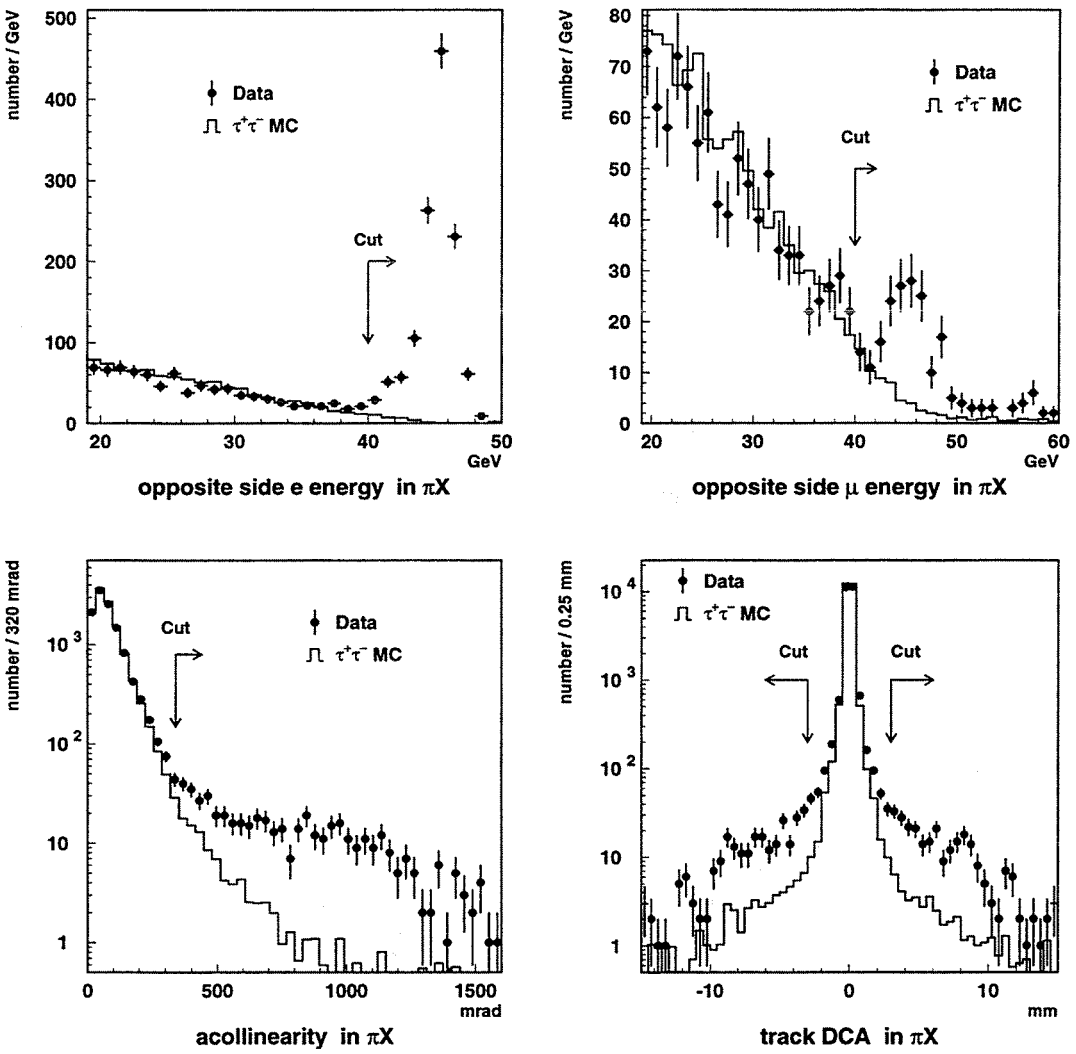

Figure 7.11: Quantities used to reject non-τ background in the selected πX sample. For each plot, all other cuts have been applied.

DCA rejects cosmic ray backgrounds. The reconstructed tracks in cosmic ray muon events typically have large DCAs. Hence, the tracks in both hemispheres are required to have DCA magnitudes less than 2 mm. This cut also removes events in which a poorly reconstructed track resulted in a large DCA. The bottom right plots in Figures 7.10 and 7.11 illustrate the DCA distributions of tracks in the ρX and πX classes.

Table 7.1 gives the year-by-year tally of selected events from data for each event class.

7.3 Estimation of Selection Efficiencies and Backgrounds

The selection efficiencies and backgrounds from misidentified τ decays were estimated by applying the selection criteria to the $\tau^+\tau^-$ Monte-Carlo event sample. To estimate the Bhabha, dimuon and two-photon event backgrounds in ρX and πX events, the opposite hemisphere electron and muon energy distributions and the acollinearity distributions were fit to the sum of distributions obtained from the $\tau^+\tau^-$ and the appropriate background process Monte-Carlo event sample. In effect, the shape of the relevant distributions were taken from Monte-Carlo, but normalized according to the data. For the $\rho\rho$, $\pi\pi$ and $\rho\pi$ events, the background contaminations were estimated directly from the background process Monte-Carlo sample. The amount of cosmic ray background was estimated from the data itself by extrapolating the tails of DCA distributions, assuming a uniform population of cosmic rays, into the signal region.

Table 7.2 summarizes the average selection efficiency $\bar{\epsilon}$ (over the 4π solid angle) and the estimated fraction of τ and non-τ background for each of the event classes. Misidentified

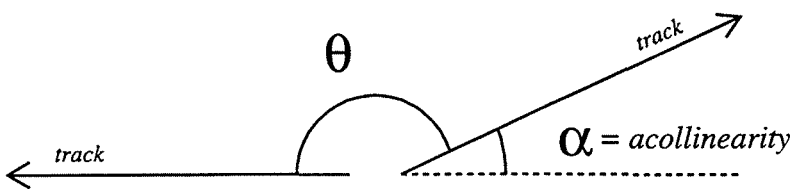

Figure 7.12: Definition of the acollinearity between two tracks. Acollinearity α is related to the opening angle θ by $\alpha = \pi - \theta$.

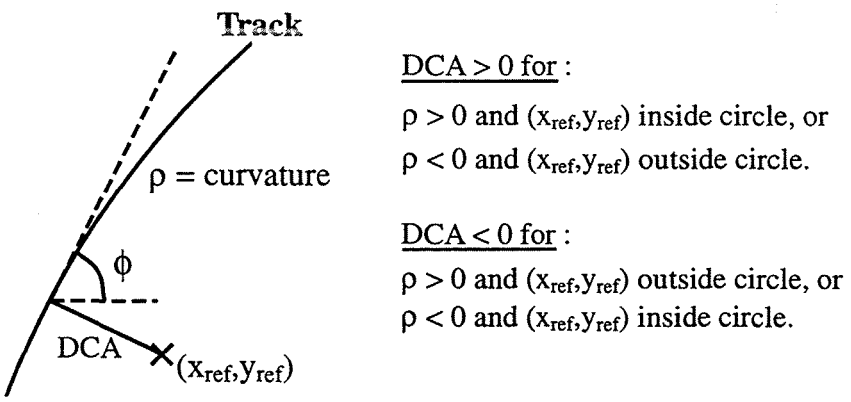

Figure 7.13: Definition of track DCA. The DCA is the minimum distance between the track trajectory and the reference point (x_{ref}, y_{ref}) in the $x - y$ plane. The nominal interaction vertex is the usual reference point. The sign of DCA depends on whether the reference point is inside or outside of the track trajectory.

τ decays are the dominant backgrounds; the bulk of the misidentifications comes from other hadronic τ decays. Figures 7.14 and 7.15 illustrate, respectively, the average selection efficiencies of $\tau^- \to \rho^- \nu_\tau$ and $\tau^- \to \pi^- \nu_\tau$ in the fiducial volume $|\cos\theta| < 0.7$ as functions of the true ω and x_π for those decays. The effects of uncertainties in the efficiencies and backgrounds are discussed in Chapter 8.

Year	ρX	πX	$\rho\rho$	$\pi\pi$	$\rho\pi$	Total
91	2129	1116	326	67	257	3895
92	4502	2337	563	167	562	8131
93	4496	2421	530	182	582	8211
94	8155	3985	899	242	980	14261
95	3832	2195	476	130	477	7110
Total	23114	12054	2794	788	2858	41608

Table 7.1: The numbers of selected events in each class by year.

	$\bar{\epsilon}$	% Bkgd	
Class	(in 4π)	τ	non-τ
ρX	32.9	12.7	0.5
πX	36.8	9.0	2.9
$\rho\rho$	21.6	23.8	< 0.1
$\pi\pi$	28.2	17.3	1.0
$\rho\pi$	24.7	20.5	< 0.1

Table 7.2: The average selection efficiencies (over 4π solid angle) and background fractions from misidentified τ decays and non-τ backgrounds for the five event classes.

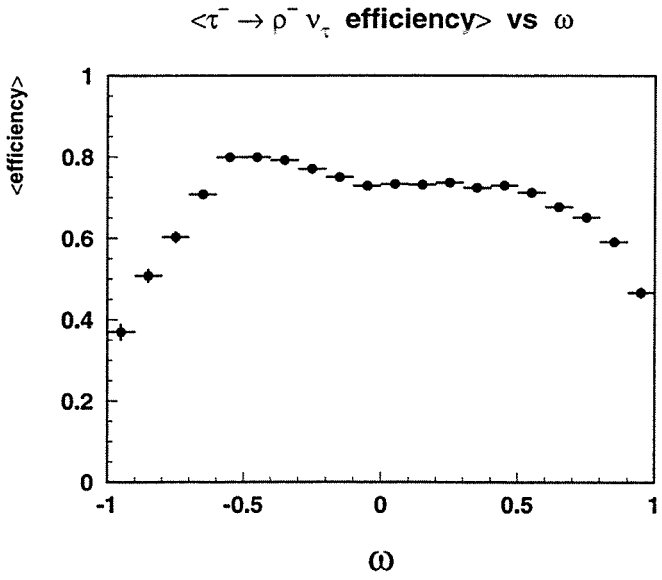

Figure 7.14: The average $\tau^- \to \rho^- \nu_\tau$ selection efficiency within the fiducial volume $|\cos\theta| < 0.7$ as a function of generated ω.

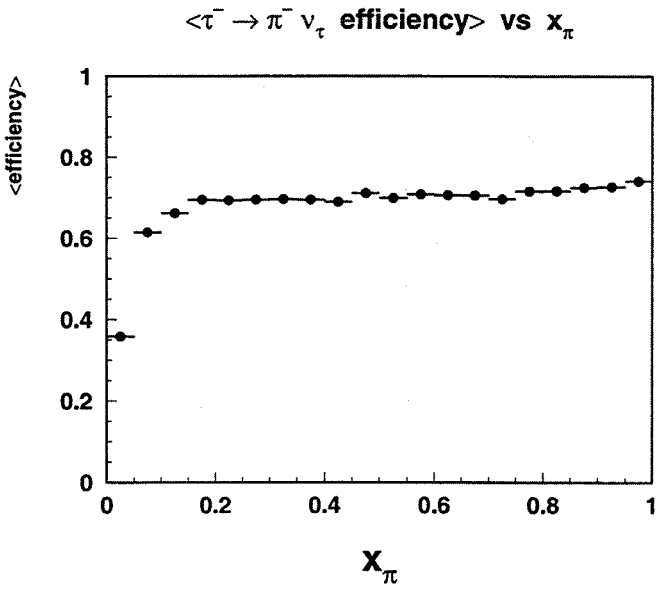

Figure 7.15: The average $\tau^- \to \pi^- \nu_\tau$ selection efficiency within the fiducial volume $|\cos\theta| < 0.7$ as a function of generated x_π.

CHAPTER 8

MEASUREMENT

8.1 Fit Results

Following the method outlined in Chapter 4, the single τ decay spectra (ρX and πX) and the correlated distributions ($\rho\rho$, $\pi\pi$ and $\rho\pi$) from the selected data events are simultaneously fit to distributions using the kinematic functions f and g constructed from the selected $\tau^+\tau^-$ Monte-Carlo events. The fit employs a binned maximum-likelihood method in which the chirality parameters and the average τ polarization are the parameters that are varied. The $\rho\rho$, $\pi\pi$ and $\rho\pi$ distributions have non-uniform bin sizes in order to combine bins having low statistics. The numbers of bins in each distribution are as follows: 20 (ρX), 15 (πX), 36 ($\rho\rho$), 15 ($\pi\pi$), and 40 ($\rho\pi$).

The fit results assuming universality between $\tau^- \to \pi^-\nu_\tau$ and $\tau^- \to \rho^-\nu_\tau$ decays, *i.e.*, $\xi_\pi = \xi_\rho \equiv \xi_h$, are:

$$\xi_h = -1.022 \pm 0.031 \qquad \text{and} \qquad \mathcal{P}_\tau = -0.146 \pm 0.011 \tag{8.1}$$

with a correlation coefficient $\rho(\xi_h, \mathcal{P}_\tau) = -0.372$. Without the universality assumption, the fit results are:

$$\xi_\rho = -1.007 \pm 0.049\,, \qquad \xi_\pi = -1.040 \pm 0.055 \qquad \text{and} \qquad \mathcal{P}_\tau = -0.147 \pm 0.011\,. \tag{8.2}$$

The correlation coefficients for this fit are:

$$\rho(\xi_\rho, \mathcal{P}_\tau) = -0.275 \qquad \rho(\xi_\pi, \mathcal{P}_\tau) = -0.161 \qquad \rho(\xi_\rho, \xi_\pi) = -0.299 \tag{8.3}$$

The uncertainties in the fitted values correspond to one standard deviation statistical errors, where the logarithm of the likelihood function decreases by 0.5 from its maximum value. The chirality parameter biases described in Chapter 4 have not been incorporated into these results.

The resultant goodness-of-fit evaluation corresponds to a confidence level of approximately 10^{-6}. The low confidence level suggests that systematic effects, not just statistical fluctuations, contribute to the poor fit. Figures 8.1 through 8.5 illustrate the data and best-fit decay distributions for the five event classes. Some discrepancies between the data and fit results are apparent.

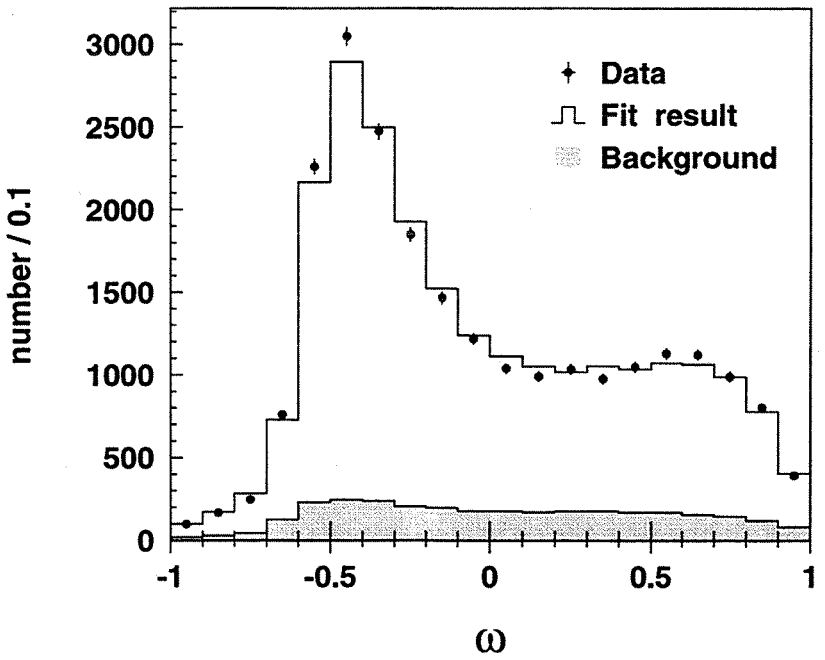

Figure 8.1: The observed and best-fit ω spectra for ρX events.

8.2 Systematic Uncertainties

The following sources of systematic uncertainties were investigated: the detector calibrations, the finite size of the Monte-Carlo event sample, uncertainties in the background

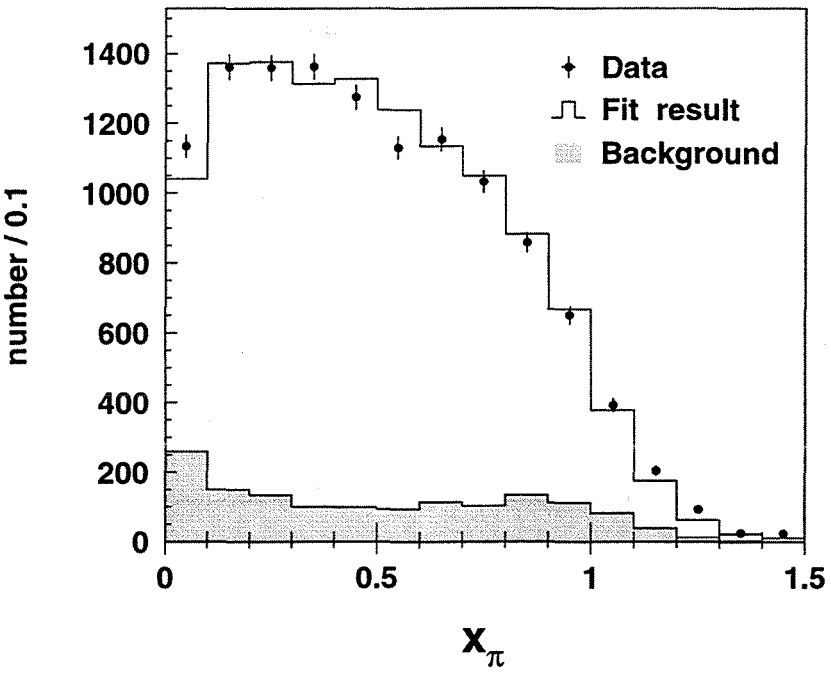

Figure 8.2: The observed and best-fit x_π spectra for πX events.

estimations, and the event selection. The uncertainties due to these sources were estimated by the changes in fit results for $\mathcal{P}_\tau$ and the chirality parameters after varying the subdetector calibration factors, the amounts of each background, and the pertinent selection cuts. These sources are considered to be independent, so the resulting uncertainties are combined quadratically. Table 8.1 summarizes the estimated systematic uncertainties of the chirality parameters and $\mathcal{P}_\tau$.

The energy scales of the BGO, HCAL and the central tracker were varied independently to investigate the effect of their calibration uncertainties. The BGO electromagnetic energy scale is known to 1% accuracy at low energies ($\sim$ 1 GeV) from the π^o peak position in the $\gamma\gamma$ invariant mass distribution. Bhabha events provide the energy scale to 0.1% accuracy at 45 GeV. The BGO scale factors in data were varied according to a linear interpolation between $\pm 1\%$ at 1 GeV and $\mp 0.1\%$ at 45 GeV.

The HCAL and the BGO responses to charged hadrons were initially investigated by a test-beam experiment [44]. The calibrations are verified and/or corrected *in situ* by using the momentum measurement from the tracker for low π energies as well as the ρ peak

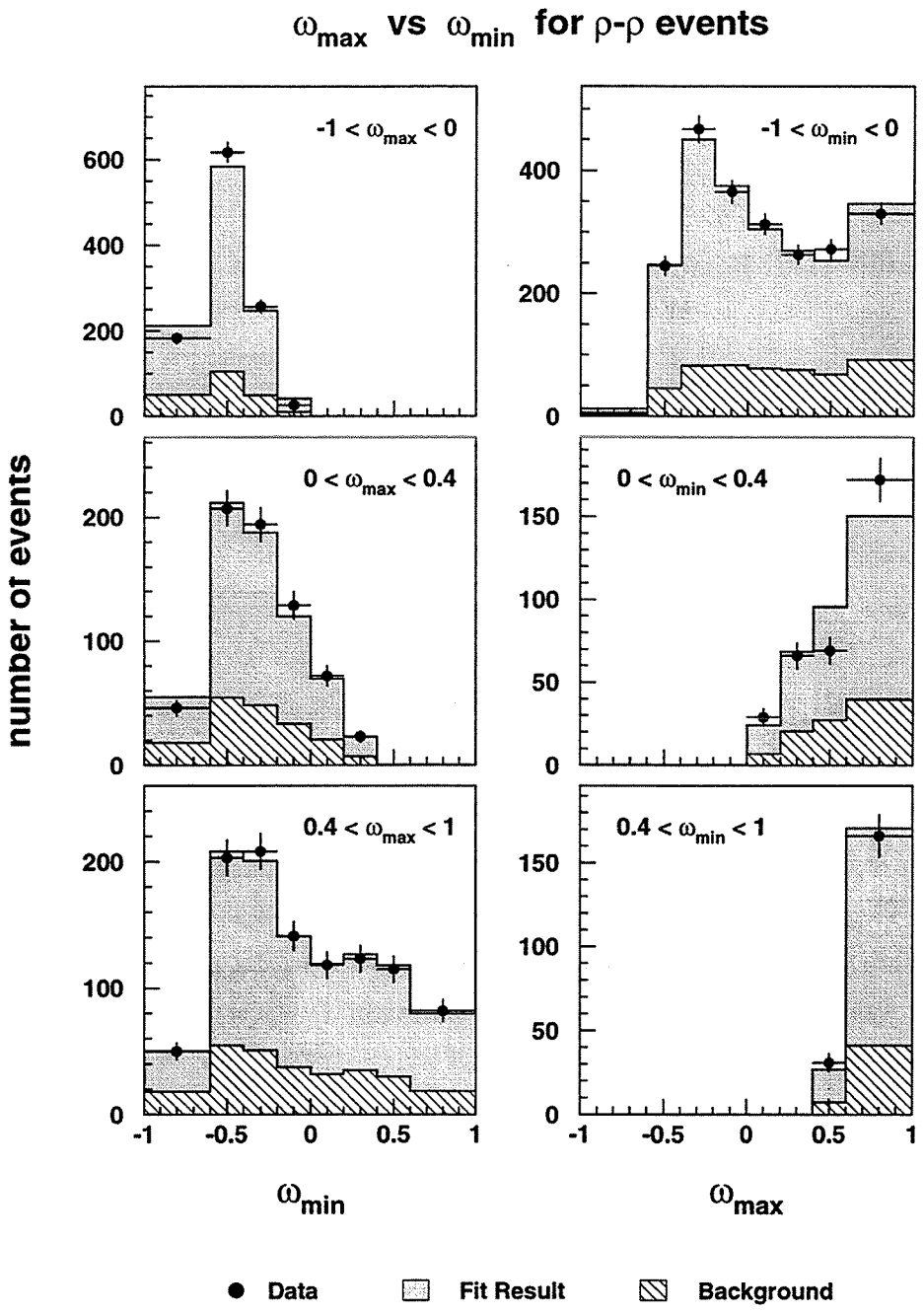

Figure 8.3: Projection slices of the observed and best-fit $(\omega_{min}, \omega_{max})$ correlated decay distributions for $\rho\rho$ events.

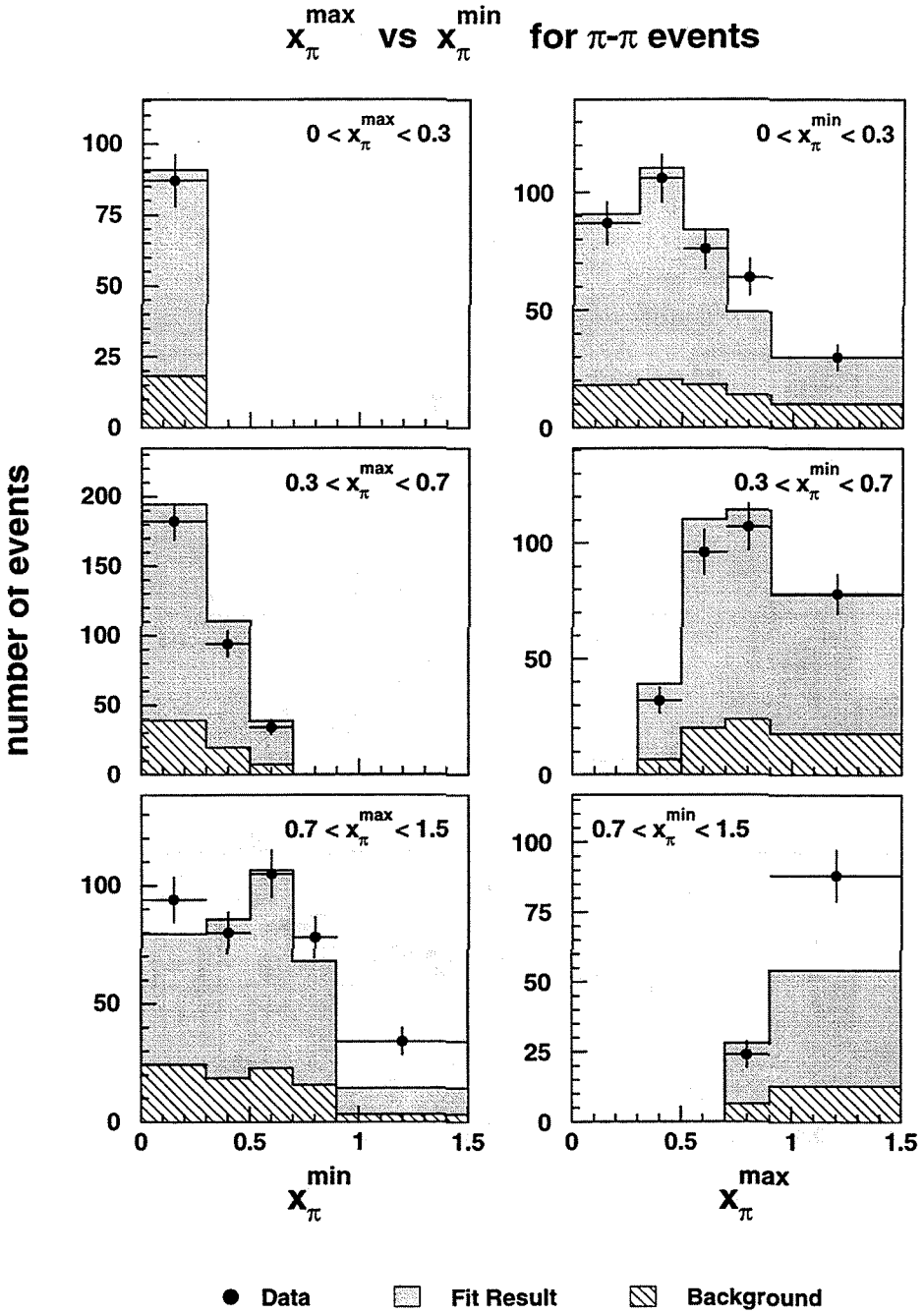

Figure 8.4: Projection slices of the observed and best-fit $(x_\pi^{min}, x_\pi^{max})$ correlated decay distributions for $\pi\pi$ events.

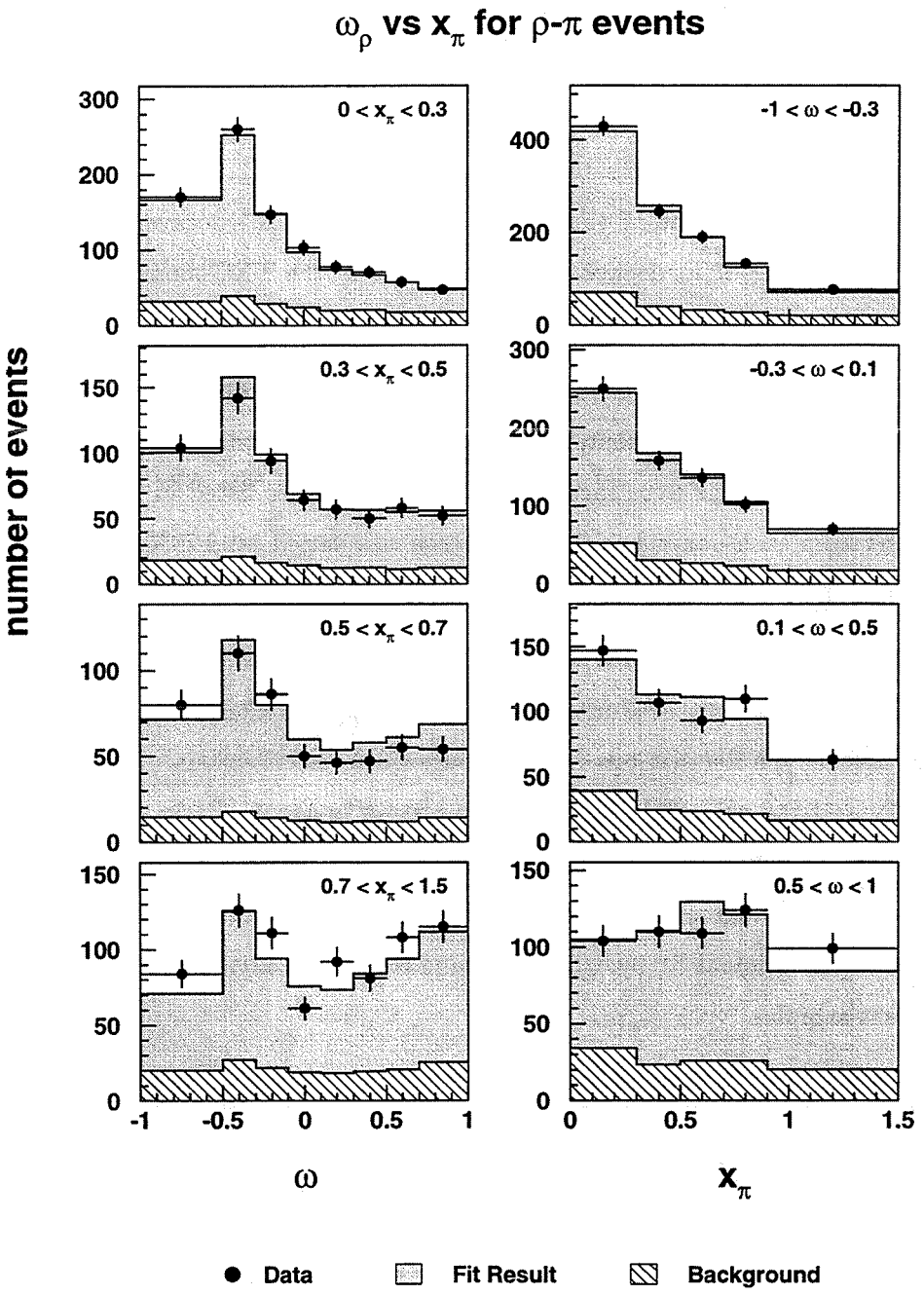

Figure 8.5: Projection slices of the observed and best-fit (x_π, ω) correlated decay distributions for $\rho\pi$ events.

position in the $\pi^-\pi^\circ$ invariant mass distribution. By comparing the ρ peak positions from data and simulation, the absolute energy scales of the BGO and HCAL for charged hadrons are known to approximately 1.5%. The effect of this uncertainty was studied by varying the relevant scales by $\pm 1.5\%$ overall and by factors changing linearly from $\pm 1.5\%$ at low energy to $\mp 1.5\%$ at high energy.

The central tracker was calibrated by using the precise (2.5% resolution) muon chamber momentum measurement of 45 GeV muons in $Z \rightarrow \mu^+\mu^-$ decays. Intermediate energy muons from $\tau^- \rightarrow \mu^-\bar{\nu}_\mu\nu_\tau$ decays were used to verify the TEC momentum scale to 1%.

Backgrounds alter the shapes of the ideal τ decay spectra in different ways. To study the effect of uncertainties in the misidentified τ decay background composition, the major τ decay mode branching fractions were varied by their uncertainties listed in Table 3.1. The estimated amount from each non-τ background source was varied by $\pm 20\%$.

A Monte-Carlo event sample of finite size harbors statistical fluctuations just like Mother Nature can produce in real data observations. To investigate statistical fluctuations in the Monte-Carlo, the fitting procedures were performed with a likelihood function which accounted for Poisson-type fluctuations in the Monte-Carlo distributions. The systematic uncertainty in $\mathcal{P}_\tau$ and the chirality parameters due to finite Monte-Carlo statistics is the quadratic difference of the statistical errors from fits using the two different likelihood functions. These numbers agree well with the naive expectations obtained by scaling the statistical errors of the original fit by $\sqrt{8}$ to account for the relative size of the data and Monte-Carlo event samples.

Source	ξ_h	$\mathcal{P}_\tau$	ξ_ρ	ξ_π	$\mathcal{P}_\tau$
Calibrations	0.006	0.013	0.022	0.026	0.013
MC Statistics	0.011	0.004	0.017	0.020	0.004
Backgrounds	0.002	0.004	0.006	0.007	0.003
Selection	0.006	0.004	0.009	0.010	0.003
Total	0.014	0.015	0.030	0.035	0.014

Table 8.1: The individual and combined systematic errors for the chirality parameters and $\mathcal{P}_\tau$.

Several facets of the Monte-Carlo simulation were compared to data in an attempt to locate discrepancies which could explain the poor goodness-of-fit result. In particular, the $\tau^- \to \rho^- \nu_\tau$ reconstruction was studied to account for systematic differences appearing each year in the shape of the ω spectrum. It was thought that perhaps the Monte-Carlo incorrectly modeled the overlapping showers in the BGO. However, the Monte-Carlo does reproduce the π^--π^o opening angle and the π^--π^o energy difference distributions observed in the data without any significant deviations. The excesses and deficits occur such that their effect of the fitted parameter values tends to cancel.

The pion energy spectra also contain unexpectedly large deviations. The effect due to the HCAL energy scale uncertainty has already been considered. The excesses in data for large pion energies ($x_\pi > 1.1$) in Figures 8.2 and 8.4 are consistent with the HCAL resolution being slightly worse than expected from the Monte-Carlo. It is difficult to independently measure the HCAL resolution for large pion energies due to the lack of statistics and pions of known energy. The deviations in the πX spectrum in the range $0.4 < x_\pi < 0.6$ correspond to the intermediate energies where the HCAL scale is calibrated least reliably. The low energy background from $\gamma\gamma$ and cosmic-ray backgrounds in πX events almost exclusively populates the first x_π bin. Underestimating these backgrounds could account for the observed excess; the consequences of such uncertainties have already been estimated. The disparities at low and high pion energies tend to cancel, so the effect on the measured values of $\mathcal{P}_\tau$ and the chirality parameter should be minor.

CHAPTER 9

CONCLUSION

9.1 Results

A 148 pb^{-1} sample of e^+e^- annihilations with center-of-mass energies $\sqrt{s} \approx M_Z$ was recorded by the L3 experiment during 1991-1995 at the LEP e^+e^- collider. From this data, 41608 $Z \to \tau^+\tau^-$ events were selected such that at least one of the τ lepton decays was identified as $\tau^- \to \pi^-\nu_\tau$ or $\tau^- \to \rho^-\nu_\tau$. These events were used to examine the Lorentz structure of the τ lepton's charged-current coupling by measuring the chirality parameter $\xi_h = \frac{2\ \mathrm{Re}(v_\tau a_\tau^*)}{(|v_\tau|^2+|a_\tau|^2)}$ which indicates the mixture of $V-A$ and $V+A$ currents and, correspondingly, the average ν_τ helicity. The average τ polarization in $Z \to \tau^+\tau^-$, $\mathcal{P}_\tau$, was measured simultaneously with the chirality parameter.

After correcting the fit results for the biases described in Chapter 4, the measurement results are, assuming universality in τ decays,

$$\begin{aligned} \xi_h &= -1.031 \pm 0.031 \pm 0.014 \\ \mathcal{P}_\tau &= -0.149 \pm 0.011 \pm 0.015\,, \end{aligned}$$

and, relaxing the universality condition,

$$\begin{aligned} \xi_\rho &= -1.025 \pm 0.048 \pm 0.030 \\ \xi_\pi &= -1.036 \pm 0.055 \pm 0.035 \\ \mathcal{P}_\tau &= -0.149 \pm 0.011 \pm 0.014 \end{aligned}$$

where the first uncertainties are statistical and the second are systematic.

The measured values of the chirality parameters are all consistent with the Standard Model prediction of -1. Moreover, the ξ_ρ and ξ_π measurements are compatible with one another, as expected for τ decay universality. This $\mathcal{P}_\tau$ measurement agrees with the previous L3 τ polarization result [45]. Within the experimental errors, the charged-current coupling of the τ lepton has a pure $V-A$ Lorentz structure in conformity with the Standard Model. Since the chirality parameter can be interpreted as the average ν_τ helicity, this measurement suggests that the ν_τ has only a left-handed helicity state.

9.2 Recent and Future Measurements

This chirality parameter measurement is consistent with recent measurements by other experiments which are listed in Table 9.1. The CLEO experiment should have the most precise chirality parameter measurement for quite some time as more data will be added to the already large $e^+e^- \to \tau^+\tau^-$ sample at $\sqrt{s} \approx 10$ GeV. The four LEP experiments have completed their $\tau^+\tau^-$ data sets as LEP now runs at energies well above the Z resonance peak. It should not be forgotten that, in addition to the chirality parameter, the Michel parameters measured in leptonic τ decays also probe the Lorentz structure of the τ lepton's charged-current coupling. Eventually, the next generation of B meson factories at the SLAC and KEK laboratories will provide $e^+e^- \to \tau^+\tau^-$ data samples many times larger than the CLEO sample, and these measurements can be repeated to perform even more stringent tests of the Standard Model's $V-A$ charged-current structure.

Experiment	Measured ξ_h
CLEO [46]	$-0.995 \pm 0.010 \pm 0.003$
SLD [26]	$-0.93 \pm 0.10 \pm 0.04$
ALEPH [47]	$-1.006 \pm 0.032 \pm 0.019$
ARGUS [48]	-1.017 ± 0.039
OPAL [28]	$\lvert 1.29 \rvert \pm 0.26 \pm 0.11$

Table 9.1: Other recent measurements of the chirality parameter.

APPENDICES

APPENDIX A

The ω Variable in $\tau^- \to \rho^- \nu_\tau$

The ω variable originated in an attempt to simplify τ polarization measurements in multipion τ decays [22]. For $\tau^- \to \rho^- \nu_\tau$, the two-dimensional decay distribution depending on the two decay angles θ^* and ψ^*

$$\frac{1}{\Gamma}\frac{d\Gamma}{d\cos\theta^* \, d\cos\psi^*} = f(\cos\theta^*, \cos\psi^*) \pm \mathcal{P}_\tau \, g(\cos\theta^*, \cos\psi^*) \tag{A.1}$$

can be rewritten in terms of $\omega \equiv g(\cos\theta^*, \cos\psi^*)/f(\cos\theta^*, \cos\psi^*)$ to obtain the familiar form

$$\frac{1}{\Gamma}\frac{d\Gamma}{d\omega} = \hat{f}(\omega)[1 \pm \mathcal{P}_\tau \, \omega] = \hat{f}(\omega) \pm \mathcal{P}_\tau \, \hat{g}(\omega) \tag{A.2}$$

Explicitly, ω can be expressed [49]:

$$\omega = \frac{b_0(\theta^*)h_0(\psi^*) + b_1(\theta^*)h_1(\psi^*)}{a_0(\theta^*)h_0(\psi^*) + a_1(\theta^*)h_1(\psi^*)} , \tag{A.3}$$

where the various components are defined

$$\begin{aligned}
h_0(\psi^*) &= 2\cos^2\psi^* \\
h_1(\psi^*) &= \sin^2\psi^* \\
a_0(\theta^*) &= m^2(F-G) + m_\tau^2 G \\
a_1(\theta^*) &= m^2(F+G) + m_\tau^2(F-G) \\
b_0(\theta^*) &= (m_\tau^2 - m^2)(F-G) + m_\tau^2 F\cos\theta^* \\
b_1(\theta^*) &= -(m_\tau^2 - m^2)(F-G) - 2m^2 F\cos\theta^* \\
F(\theta^*) &= [m_\tau^2 + m^2 + (m_\tau^2 - m^2)\cos\theta^*]^2 \\
G(\theta^*) &= [m_\tau^2 - m^2 + (m_\tau^2 + m^2)\cos\theta^*]^2 .
\end{aligned}$$

APPENDIX B

Glossary of Acronyms

ADC - Analog to Digital Converter

BGO - Bismuth Germanium Oxide

CERN - Conseil Européen pour la Recherche Nucléaire

DAQ - Data AcQuisition

DCA - Distance of Closest Approach

DRP - Data Reduction Processor

EPA - Electron-Positron Accumulator

FB - Forward/Backward (Muon Chambers)

HCAL - Hadronic CALorimeter

IP - Interaction Point

ISR - Initial State Radiation

KEK - Kou-Enerugii Kasokuki Kenkyuu Kikou
(Japanese High-Energy Accelerator Research Organization)

LEP - Large Electron Positron Collider

LIL - LEP Injector Linacs

MIP - Minimum Ionizing Particle

NMR - Nuclear Magnetic Resonance

PS - Proton Synchrotron

QCD - Quantum ChromoDynamics

QED - Quantum ElectroDynamics

RF - Radio Frequency

SLAC - Stanford Linear Accelerator Center

SM - Standard Model

SMD - Silicon Microstrip Detector

SPS - **S**uper **P**roton **S**ynchrotron

ST - **S**upport **T**ube

TDC - **T**ime to **D**igital **C**onverter

TEC - **T**ime **E**xpansion **C**hamber

BIBLIOGRAPHY

BIBLIOGRAPHY

[1] S. Weinberg, *Phys. Rev. Lett.* **19** (1967) 1264.

[2] A. Salam, in Proceedings of the 8th Nobel Symposium, ed. N. Svartholm, Stockholm, 1968.

[3] S. Glashow, *Nucl. Phys.* **22** (1961) 579.

[4] W. Fetscher, H.-J. Gerber, and K.F. Johnson, *Phys. Lett.* **B 173** (1986) 102.

[5] G. Kane, *Modern Elementary Particle Physics*, (Addison-Wesley Publishing Co., 1993).

[6] I.J.R. Aitchison and A.J.G. Hey, *Gauge Theories in Particle Physics*, (IOP Publishing Ltd., second edition, 1989).

[7] P.A.M. Dirac, *Proc. R. Soc.* **A 117** (1928) 610.

[8] N. Cabibbo, *Phys. Rev. Lett.* **10** (1963) 531.

[9] M. Kobayashi and T. Maskawa, *Prog. Theor. Phys.* **49** (1973) 652.

[10] F. Englert and R. Brout, *Phys. Rev. Lett.* **13** (1964) 321.

[11] P.W. Higgs, *Phys. Lett.* **12** (1964) 132.

[12] Particle Data Group, R.M. Barnett *et al.*, *Phys. Rev.* **D 54** (1996) 1.

[13] The LEP Collaborations ALEPH, DELPHI, L3 and OPAL, the LEP Electroweak Working Group, and the SLD Heavy Flavor Group, *A Combination of Preliminary Electroweak Measurements and Constraints on the Standard Model*, Internal Report LEPEWWG/97-02, CERN, 1997.

[14] M.L. Perl *et al.*, *Phys. Rev. Lett.* **35** (1975) 297.

[15] P. Weber, in Proceedings of the Fourth Workshop on Tau Lepton Physics (TAU96), ed. J.G. Smith and W. Toki, (Elsevier Science B.V., 1997), p. 107.

[16] ALEPH Collab., D. Buskulic *et al.*, *Phys. Lett.* **B 349** (1995) 103.

[17] M. Consoli *et al.*, *Electroweak Radiative Corrections for Z Physics*, in Z Physics at LEP 1, ed. R. Kleiss G. Altarelli and C. Verzegnassi, volume 1, 1989.

[18] F.A. Berends *et al.*, *Z Line Shape*, in Z Physics at LEP 1, ed. R. Kleiss G. Altarelli and C. Verzegnassi, volume 1, 1989.

[19] G. Burgers *et al.*, *Δr, or The Relation Between the Electroweak Couplings and the Weak Boson Masses*, in Z Physics at LEP 1, ed. R. Kleiss G. Altarelli and C. Verzegnassi, volume 1, 1989.

[20] M.A.B. Bég *et al.*, *Phys. Rev. Lett.* **38** (1977) 1252.

[21] Y.S. Tsai, *Phys. Rev.* **D 4** (1971) 2821, Erratum, *Phys. Rev.* **D 13** (1976) 771.

[22] M. Davier, L. Duflot, F. Le Diberder and A. Rougé, *Phys. Lett.* **B 306** (1993) 411.

[23] C. Nelson, *Phys. Rev.* **D 40** (1989) 123, Erratum, *Phys. Rev.* **D 41** (1990) 2327.

[24] R. Alemany *et al.*, *Nucl. Phys.* **B 379** (1992) 3.

[25] SLD Collab., K. Abe *et al.*, *Phys. Rev. Lett.* **79** (1997) 804.

[26] SLD Collab., K. Abe *et al.*, *Phys. Rev. Lett.* **78** (1997) 4691.

[27] ARGUS Collab., H. Albrecht *et al.*, *Z. Phys.* **C 58** (1993) 61.

[28] OPAL Collab., K. Ackerstaff *et al.*, *Z. Phys.* **C 75** (1997) 593.

[29] B. Jadach, B.F.L. Ward and Z. Wąs, *Comp. Phys. Comm.* **66** (1991) 276, (KORALZ Version 3.8).

[30] B. Jadach, B.F.L. Ward and Z. Wąs, *Comp. Phys. Comm.* **79** (1994) 503, (KORALZ Version 4.0).

[31] B. Jadach, J.H. Kühn and Z. Wąs, *Comp. Phys. Comm.* **64** (1991) 275, (TAUOLA Version 1.5).

[32] R. Decker, B. Jadach, J.H. Kühn and Z. Wąs, *Comp. Phys. Comm.* **76** (1993) 361, (TAUOLA Version 2.4).

[33] F. James, *MINUIT Version 94.1 Reference Manual*, Internal Report CERN Program Library Long Writeup D506, CERN CN Division, 1994.

[34] S. Baker and R.D. Cousins, *Nucl. Inst. Meth.* **A 221** (1984) 437.

[35] *Design Study of a 15 to 100 GeV* e^+e^- *Colliding Beam Machine (LEP)*, CERN/ISR-LEP 78/17, 1978.

[36] *LEP Design Report (Vol. 1) - The LEP Injector Chain*, CERN/LEP 83-29, 1983.

[37] *LEP Design Report (Vol. 2) - The LEP Main Ring*, CERN/LEP 84-01, 1984.

[38] L3 Collab., B. Adeva *et al.*, *Nucl. Inst. Meth.* **A 289** (1990) 35.

[39] L3 SMD Collab., M. Acciarri *et al.*, *Nucl. Inst. Meth.* **A 360** (1995) 103.

[40] L3 F/B Muon Group, A. Adam *et al.*, *Nucl. Inst. Meth.* **A 383** (1996) 342.

[41] R. Brun *et al.*, *GEANT 3*, Internal Report DD/EE/84-1, CERN, 1984, revised September 1987.

[42] H. Fesefeldt, Internal Report PITHA 85/02, RWTH Aachen, 1985.

[43] L3 Collab., O. Adriani *et al.*, *Phys. Lett.* **B 294** (1992) 466.

[44] I.J. Scott, *A Measurement of the Polarization of Tau Leptons in Z Decays with the L3 Detector at LEP*, Ph.D. thesis, Harvard University, 1993.

[45] L3 Collab., M. Acciarri *et al.*, *Phys. Lett.* **B 341** (1994) 245.

[46] CLEO Collab., J.P. Alexander *et al.*, *Phys. Rev.* **D 56** (1997) 5320.

[47] ALEPH Collab., D. Buskulic *et al.*, *Phys. Lett.* **B 346** (1995), Erratum, *Phys. Lett.* **B 363** (1995) 265.

[48] ARGUS Collab., H. Albrecht *et al.*, *Phys. Lett.* **B 349** (1995) 576.

[49] A. Rougé, *On the estimation methods in the measurement of tau polarization*, Internal Report X-LPNHE 92/20, LPNHE Ecole Polytechnique-IN2P3, 1992.